

# UC Irvine

## UC Irvine Electronic Theses and Dissertations

### Title

Emerging air quality concerns in California: Atmospheric fates of neonicotinoid pesticides and increasing wildfire influence on ozone attainment

### Permalink

<https://escholarship.org/uc/item/86n5356n>

### Author

Anderson, Andrea

### Publication Date

2022

### Copyright Information

This work is made available under the terms of a Creative Commons Attribution-NonCommercial License, available at <https://creativecommons.org/licenses/by-nc/4.0/>

Peer reviewed|Thesis/dissertation

UNIVERSITY OF CALIFORNIA,  
IRVINE

Emerging air quality concerns in California: Atmospheric fates of neonicotinoid pesticides  
and increasing wildfire influence on ozone attainment

DISSERTATION

submitted in partial satisfaction of the requirements  
for the degree of

DOCTOR OF PHILOSOPHY

in Chemistry

by

Andrea Anderson

Dissertation Committee:  
Professor Barbara J. Finlayson-Pitts, Chair  
Professor Sergey Nizkorodov  
Professor Craig C. Martens

2022

Portions of Chapters 2 and 3 © 2019 and 2021 American Chemical Society  
Portion of Chapters 5 © 2022 European Geosciences Union  
All other materials © 2022 Andrea Anderson

## **DEDICATION**

To my parents,

with deepest thankfulness for their unending support,  
for filling my life with fun and adventure,  
and for fostering my curiosity in the natural world.

## TABLE OF CONTENTS

Dedication .....	ii
List of Figures .....	vi
List of Tables .....	xii
Acknowledgements .....	xiii
Vita .....	xv
Abstract of the Dissertation .....	xviii
Chapter 1: Introduction .....	20
1.1 Atmospheric chemistry research in California air quality .....	20
1.2 Challenges of pesticides .....	21
1.3 Neonicotinoid history and concerns .....	22
1.4 Goals of neonicotinoid multi-phase atmospheric chemistry experiments .....	25
1.5 Goals of wildfire effects on ozone attainment research .....	26
Chapter 2: Photochemistry of neonicotinoids .....	28
2.1 Research goals .....	28
2.2 Methods .....	28
2.2.1. Thin film preparation .....	28
2.2.2. Photolysis setup .....	28
2.3 Absorption cross sections .....	29
2.4 Quantum yields and atmospheric lifetimes .....	30
2.5 Gas and solid phase products .....	36
Chapter 3: Matrix effects of commercial formulations on neonicotinoid degradation .....	37
3.1 Research goals .....	37
3.2 Methods .....	38
3.2.1. Commercial formulations .....	38
3.2.2. Preparation and IR analysis of KBr pellets .....	38
3.2.3. DART mass spectrometry .....	43
3.2.4. High resolution mass spectrometry (HRMS) .....	43
3.2.5. Preparation and analysis of thin films .....	45
3.2.6. Calculation of absolute number of molecules .....	45
3.3 Infrared spectra analysis of the pure NNs versus commercial formulation .....	46
3.4 Major NPM photolysis products .....	48

3.5 Major DNF photolysis products: desnitro and urea pathways .....	51
3.6 “Solid phase” products unique to DNF.....	56
3.7 Change in products after photolysis.....	61
3.8 6. N <sub>2</sub> O yields.....	65
3.9 Quantum yield calculations for loss of NN during photolysis .....	66
3.10 Conclusions.....	72
Chapter 4: Hydroxyl radical oxidation reactions with neonicotinoids .....	74
4.1 Research Goals .....	74
4.2 Methods .....	74
4.2.1. OH generation .....	74
4.2.2. OH measurement.....	75
4.2.3. NN thin film preparation.....	76
4.2.4. ATR FTIR cell measurements.....	77
4.2.5. Product Analysis by Mass Spectrometry (HRMS and DART-MS).....	79
4.3 In situ monitoring using ATR FTIR .....	81
4.4 Product Identification .....	86
4.4.1. Imidacloprid .....	86
4.4.2. Dinotefuran .....	96
4.4.3. Clothianidin.....	99
4.4.4. Summary of common products .....	103
4.5 Environmental implications .....	108
4.5.1. Atmospheric Lifetimes.....	108
4.5.2. Mechanism.....	109
4.6 Conclusions .....	111
Chapter 5: Wildfire influence on ozone levels: Insights into California ozone sensitivity using ground and satellite measurements .....	112
5.1 Introduction .....	112
5.2 Research Goals .....	117
5.3 Methods .....	117
5.3.1. Ground-Level Air Quality Monitoring Data.....	117
5.3.2. TROPOMI Satellite Data for O <sub>3</sub> -NO <sub>x</sub> -VOC sensitivity .....	120
5.3.3. Threshold Exceedance Determination (TED).....	121

5.4 Identification of fire-influenced days.....	124
5.5 Seasonal Shifts in TROPOMI HCHO/NO <sub>2</sub> ratios.....	128
5.5.1. HCHO/NO <sub>2</sub> ratios on tier 2 days .....	132
5.6 Effects on O <sub>3</sub> levels .....	134
5.7 Application of TED technique to field chamber studies in Sacramento .....	139
5.8 Conclusions .....	142
References .....	144

## LIST OF FIGURES

- Figure 1.1 1948 photo of the Los Angeles Civic Center at the height of a smog attack, the buildings one block away are barely visible, from the Los Angeles Times Photographic Archive.<sup>1</sup> ..... 20
- Figure 1.2 Neonicotinoid structures grouped by chromophore..... 23
- Figure 2.1 Absorption cross sections of the neonicotinoids in acetonitrile and TMX in methanol, where nitroguanidines are in blues, nitromethylenes are in green, and cyanamidines are in reds. .... 30
- Figure 2.2 FTIR spectra of CLD before photolysis (black) and difference spectra after photolysis (blue), which is  $\log(S_0/S_t)$ , where  $S_0$  is the single beam spectra before photolysis and  $S_t$  is the single beam spectra at a given photolysis time, and positive peaks indicate product formation and negative peaks indicate reactant loss..... 32
- Figure 2.3 First-order degradation plots of CLD and IMD during 254 nm and 313 nm photolysis following loss of the -NO<sub>2</sub> peak..... 33
- Figure 3.1 SEM-EDS image of 5% w/w imidacloprid (IMD)/KBr pellet surface mounted on carbon tape showing distribution of K, Br, O, Cl, C, and N. Colored areas show the presence of individual elements. IMD was used because of the presence of a Cl atom which has a strong SEM-EDS signal and facilitates detection..... 40
- Figure 3.2 (a) Schematic of the reaction cell. Samples were attached to a circular sample holder connected to a retractable rod and placed in a custom-built glass FTIR cell with CaF<sub>2</sub> windows. Light below 290 nm was removed using a glass filter and a water-filled cuvette was used to absorb heat from the lamp. The lamp, water compartment, and light filter were removed to probe the NN/KBr pellet with the IR beam. (b) A photo of a typical NN/KBr sample pellet. (c) The combined gas and solid spectra are measured with the rod in the down position and the gas phase only in the rod up position. Spectra of the solid pellet only were obtained by subtracting the gas phase spectrum from the combined gas and solid spectrum. .... 41
- Figure 3.3 Relative emission spectra of UV lamps used for photolysis. .... 42
- Figure 3.4 FTIR spectra of DNF and NPM in three solid forms. (a) DNF: (blue) pure DNF in a KBr pellet by transmission ( $3.9 \times 10^{14}$  molecules/cm<sup>2</sup> DNF), (green) commercial formulation Safari in a KBr pellet by transmission ( $3.6 \times 10^{14}$  molecules/cm<sup>2</sup> DNF), and (black) pure DNF in a thin film by ATR ( $3.1 \times 10^{14}$  molecules/cm<sup>2</sup> DNF); and (b) NPM: (blue) pure NPM in a KBr pellet by transmission ( $1.8 \times 10^{15}$  molecules/cm<sup>2</sup>



NPM), (green) commercial formulation Capstar™ in a KBr pellet by transmission ( $2.3 \times 10^{15}$ molecules/cm <sup>2</sup> NPM), and (black) pure NPM in a thin film by ATR ( $1.3 \times 10^{15}$ molecules/cm <sup>2</sup> NPM).....	47
Figure 3.5 DART-MS of NPM before (black traces) and after (color traces) photolysis at 350 nm for 3 hours in three solid forms.....	49
Figure 3.6 FTIR spectra for NPM irradiated at 305 nm in three solid forms: ( <b>blues</b> ) pure NPM in a KBr pellet ( $5.1 \times 10^{14}$ molecules/cm <sup>2</sup> NPM at 35% and 50% loss), ( <b>greens</b> ) commercial formulation Capstar™ in a KBr pellet ( $3.2 \times 10^{15}$ molecules/cm <sup>2</sup> NPM, 20% and 48% loss), and ( <b>pinks</b> ) pure NPM in a thin film ( $1.4 \times 10^{15}$ molecules/cm <sup>2</sup> NPM at 16%, 50% and 92% loss). Gray traces show initial absorbance spectra before photolysis. The initial absorbance spectrum of the commercial formulation has been multiplied by a factor of 0.1.....	50
Figure 3.7 DART-MS of DNF before (black traces) and after (color traces) photolysis at 305 nm in three solid forms.....	52
Figure 3.8 Proposed DNF degradation mechanism, based on Wang et al. 2019 <sup>46</sup> and Aregahegn et al. 2016. <sup>47</sup> .....	54
Figure 3.9 Solid-phase difference spectra of DNF irradiated at 305 nm in three matrices: ( <b>blue</b> ) pure DNF in a KBr pellet by transmission ( $3.9 \times 10^{14}$ molecules/cm <sup>2</sup> DNF, 43 % loss), and ( <b>green</b> ) commercial formulation Safari® in a KBr pellet by transmission ( $3.6 \times 10^{14}$ molecules/cm <sup>2</sup> DNF, 31% loss), and ( <b>pink</b> ) pure DNF in a thin film by ATR ( $3.1 \times 10^{14}$ molecules/cm <sup>2</sup> DNF, 36% loss). Gray traces show initial absorbance spectra before photolysis for reference, and these spectra in the 1900-1500 region cm <sup>-1</sup> are not to scale.....	55
Figure 3.10 FTIR spectra comparing solid and gas phase products of 0.5% DNF/KBr photolyzed at 254 nm to 59% loss DNF.....	56
Figure 3.11 Comparison of solid phase product formation in KBr pellets at w/w concentrations of 0.49% DNF/KBr, 1.04% CLD/KBr, 0.94% TMX/KBr, and 0.94% IMD/KBr, and 0.67% NPM/KBr. Nitroguanidines were irradiated at 254 nm for ~30 min, and NPM for 10 hours.....	58
Figure 3.12 Crystal structures of DNF (top) and IMD (bottom) adapted from Le Questel et al. <sup>51</sup> The red circles highlight the differences between DNF and IMD in -NO <sub>2</sub> hydrogen bonding. ....	60
Figure 3.13 Proposed isomerization of -NO <sub>2</sub> to -ONO to produce NO <sup>+</sup> .....	61

- Figure 3.14 0.49% DNF/KBr irradiated at 254 nm to 21% loss DNF (dashed line), and then monitored for 4 days in dark conditions. Frames (a) and (b) are of solid phase only spectra (gas phase has been subtracted) and results in (c) for  $N_2O(g)$  are taken from gas phase only spectra. Y-axis is absorbance peak height for (a) DNF at  $1616\text{ cm}^{-1}$ , (b) product peak heights for  $NO^+$  ( $2136\text{ cm}^{-1}$ ) and  $N_2O(s)$  ( $2222\text{ cm}^{-1}$ ) products, and (c)  $N_2O(g)$  peak measured at  $2235\text{ cm}^{-1}$  from the gas phase spectra..... 63
- Figure 3.15 0.49% DNF/KBr irradiated with a 254 nm lamp for 30 min (pink trace). The photolysis lamp was shut off and the sample was then monitored for 4 days in dark conditions. Spectra are (a) solid phase only and (b) gas phase only..... 64
- Figure 3.16 Photolysis rate constants ( $k_p$ ) at varying initial absorbances (proportional to concentration) recorded for NPM and Capstar (top) and DNF and Safari (bottom). ..... 67
- Figure 3.17 Quantum yields for pure NN in thin films and pure and formulated NN in KBr pellets. Errors are  $\pm 1\sigma$ . The asterisk (\*) indicates that the quantum yield at 350 nm for NPM has not been corrected for a possible change in absorption cross section due to adsorbed water. The value shown is therefore a lower limit.... 69
- Figure 3.18 UV-Vis absorbance spectra (top) of 0.36 mM NPM in acetonitrile, 0.48% NPM/KBr (w/w), and 4.8% Capstar™/KBr and photolysis lamp emission spectra (bottom). Obtaining quantitatively reproducible spectra of solids is difficult due to the inhomogeneity of the pellets and light scattering differences so three runs of each were carried out, green are replicate runs of Capstar™ in KBr and blue are NPM in KBr..... 71
- Figure 4.1: (a) observed total  $^{13}CO_2$  from  $2268\text{ cm}^{-1}$  peak in FTIR, (b) calibration curve for  $^{13}CO_2$  using  $2268\text{ cm}^{-1}$  peak, (c) amount of  $^{13}CO_2$  generated in each photolysis interval, and (d) calculated OH concentration from  $^{13}CO + OH$  reactions and their polynomial fits to determine [OH] at  $t=0$ . Colors represent three different trials. .... 76
- Figure 4.2: Lamp filter cut offs (right axis) overlaid with the IMD absorption cross section (left axis). DNF and CLD have similar absorption cross sections..... 77
- Figure 4.3: Calibration curves of thin films of NN on ZnSe crystals using FTIR. .... 78
- Figure 4.4: FTIR spectra of IMD, CLD, and DNF (grey) and difference spectra after reaction, which show  $\log S_0/S_1$  where  $S_0$  is the single beam of the NN before reaction and  $S_1$  is the single beam at the selected reaction time. The first is reaction with OH (blue), the second is exposure to UV and the 360 nm filter, and the third is

exposure to IPN in the dark (pink). Initial absorbance spectra have been scaled by a factor 0.5. ....	82
Figure 4.5: Observed loss of IMD (1560 cm <sup>-1</sup> ), DNF (1615 cm <sup>-1</sup> ), and CLD (1615 cm <sup>-1</sup> ) thin films during OH reactions, where the slope at t = 0 on the left graphs is the initial number of reactions cm <sup>-2</sup> s <sup>-1</sup> (R <sub>0</sub> ). ....	83
Figure 4.6 Typical HRMS total ion chromatogram (TIC) for (a) IMD, (b) DNF, and (c) CLD after reaction with OH (blue traces), as well as control studies of before reaction (grey traces) and in UV + 360 nm filter conditions (tan traces). Chromatogram peaks are labeled with the major ion observed within that peak. ....	87
Figure 4.7: Extracted ion chromatogram (EIC) of HRMS peaks at m/z 256, 270, 272, 254 (offset for clarity) and 225 for IMD + OH reactions. ....	92
Figure 4.8: Typical DART-MS spectra of IMD samples. The top pane (a) shows IMD on ZnSe before reaction. The second pane (b) shows representative IMD spectra after 15 hours reaction with OH. The bottom pane (c) shows IMD after 20 hours of photolysis with a 360 nm optical filter. Spectra of background room air has been subtracted. ....	94
Figure 4.9: Extracted ion chromatograms (EIC) for species with m/z 203, 217, 219, 201 (offset for clarity) and 172 in DNF + OH reaction. ....	97
Figure 4.10: Typical DART-MS spectra of DNF samples. The top pane (a) shows DNF on ZnSe before reaction. The second pane (b) shows representative DNF spectra after 16 hours reaction with OH. The bottom pane (c) shows DNF after 18 hours of photolysis with a 360 nm optical filter. Spectra of background room air has been subtracted. ....	98
Figure 4.11: Extracted ion chromatograms (EIC) for species with m/z 250, 264, 266 and 219 in CLD + OH reaction. ....	101
Figure 4.12: Typical DART-MS spectra of CLD samples. The top pane (a) shows CLD on ZnSe before reaction. The second pane (b) shows representative CLD spectra after 16 hours treatment with OH. The bottom pane (c) shows CLD after 19 hours of photolysis with a 360 nm optical filter. Background room air has been subtracted. ....	102
Figure 4.13: Summary of common OH reaction products observed using IMD as an example, with only one isomer shown for simplicity. ....	103

Figure 4.14: Extracted ion chromatograms (EIC) for species of interest in IMD + OH reaction. Peaks are labeled by their dominant ion, and are in grey if the ion of interest is not the dominant ion (i.e. it is occurring as a fragment of a larger signal).....106

Figure 4.15: : Extracted ion chromatograms (EIC) for doubly-oxidized species in DNF + OH reaction. Peaks are labeled by their dominant ion, and are in grey if the ion of interest is not the dominant ion (i.e. the ion is a fragment of a larger signal and is not counted as an isomer identification).....107

Figure 4.16: Extracted ion chromatograms (EIC) for doubly-oxidized species in CLD + OH reaction. Signals for a double carbonyl product (m/z 278) and carbonyl + alcohol product (m/z 279) were not observed. Peaks are labeled by their dominant ion.....108

Figure 4.17: Proposed mechanism of IMD reaction with OH.....109

Figure 5.1 Ozone isopleths for urban (left) and rural (right) sites in the South Coast Air Basin, where the x-axis shows anthropogenic VOC emissions, and the y-axis shows anthropogenic NO<sub>x</sub> emissions at ranges of 20-100% of the projected 2030 anthropogenic emissions. The color scheme represents the ozone design values in ppb, where 70 ppb is the NAAQS attainment value. Adapted from Collet et al.<sup>146</sup> .....113

Figure 5.2 Schematic representation of the NO<sub>x</sub> and radical reaction cycles involved in the production and consumption of ozone, adapted from Milford et al.<sup>145</sup> .....114

Figure 5.3 8-hour O<sub>3</sub> design value in California from 1993 to 2020, adapted from the CARB 2022 Draft SIP,<sup>149</sup> where areas in green (< 70 ppb) meet NAAQS.....115

Figure 5.4: Map of ground monitor locations. ....120

Figure 5.5 Ground-level air quality data in Butte County compared to reported wildfires<sup>165</sup> in Butte County. ....122

Figure 5.6: Example of ground monitor data retrieved for each site. Colors show differentiation of days between tiers, where Tier 1 (teal) are control days, Tier 2 (red) are extreme air pollution event days, and Tier 3 (yellow) are NAAQS exceedance days that did not meet criteria for Tier 2. The tiers are determined by the TED method described in the methods section, based on values of PM<sub>10</sub>, PM<sub>2.5</sub>, and CO. O<sub>3</sub> data is also shown in the top pane, but was not used in the binning process. The dashed line in the O<sub>3</sub> pane is the 8-hour O<sub>3</sub> NAAQS of 70 ppb. ....124

Figure 5.7: Histogram of identifications of tier 2 days, normalized to the normal of monitors in each air basin. Reported CAL FIRE<sup>165</sup> begin dates correlating with large identification peaks are also marked ..... 126

Figure 5.8 Tons of PM or VOCs reported in agricultural burn notices in 2018 in San Joaquin Valley.<sup>166</sup> ..... 127

Figure 5.9: Visualization of TROPOMI HCHO/NO<sub>2</sub> values in each air basin aggregated by month from 2018-2020. Median values are bars across box, the top and bottom of boxes indicate the 75<sup>th</sup> and 25<sup>th</sup> percentiles, and whiskers show 90<sup>th</sup> and 10<sup>th</sup> percentiles. Outlier points have been hidden from the box-and-whiskers display, and instead individual data points are shown behind box plots. Statistical significance of tier 2 and tier 3 days compared to tier 1 days are calculated using Wilcoxon tests, where \* represents statistical significance (\* is  $p < 0.05$ , \*\* is  $p < 0.01$ , \*\*\* is  $p < 0.001$ , and \*\*\*\* is  $p < 0.0001$ ) and groups with no \* are not statistically different..... 129

Figure 5.10: Median monthly TROPOMI HCHO and NO<sub>2</sub> values compared to their January values, highlighting an increase in HCHO values in the summer months..... 131

Figure 5.11: Visualization of MDA8 O<sub>3</sub> levels in each air basin aggregated by month from 2018-2020. Median values are bars across box, the top and bottom of boxes indicate the 75<sup>th</sup> and 25<sup>th</sup> percentiles, and whiskers show 90<sup>th</sup> and 10<sup>th</sup> percentiles. Outlier points have been hidden from the box-and-whiskers display, and instead individual data points are shown behind box plots. Statistical significance of tier 2 and tier 3 days compared to tier 1 days are calculated using Wilcoxon tests, where \* represents statistical significance (\* is  $p < 0.05$ , \*\* is  $p < 0.01$ , \*\*\* is  $p < 0.001$ , and \*\*\*\* is  $p < 0.0001$ ) and groups with no \* are not statistically different..... 135

Figure. 5.12: Visualization of observed HCHO/NO<sub>2</sub> ratio and O<sub>3</sub> differences on tier 2 and tier 1 days, colored by month. Wildfire season corresponds to red colors..... 137

Figure 5.13 Identification of extreme air pollution event days in Sacramento using the TED method. .... 140

Figure 5.14 Monthly variation of  $\Delta O_3$  (box) observed in chamber studies due to NO<sub>x</sub> addition ( $\Delta O_3^{+NO_x}$ , a) and VOC addition ( $\Delta O_3^{+VOC}$ , b) including wildfire days (shaded box) and without wildfire days (open box). TROPOMI HCHO/NO<sub>2</sub> values (diamond) are also shown..... 141

## LIST OF TABLES

Table 2.1: Quantum yield calculation for CLD .....	34
Table 2.2: Quantum Yields ( $\phi$ ) for photolysis of neonicotinoids at different wavelengths..	35
Table 3.1 Nitrous oxide yields ( $\Delta[\text{N}_2\text{O}]/\Delta[\text{NN}]$ ) from photolysis of dinotefuran in different matrices .....	65
Table 3.2 Comparison of quantum yields in three matrices .....	68
Table 4.1: Uptake coefficients of heterogeneous NN + OH reactions .....	85
Table 4.2: Products observed in the oxidation of solid NN by gas phase OH radicals .....	88
Table 5.1: Ground-monitor site locations.....	119
Table 5.2: Threshold exceedance value (TED) method summary for wildfire influence summary.....	123

## ACKNOWLEDGEMENTS

I would like to express the deepest appreciation to my committee chair, Professor Barbara Finlayson-Pitts, for her support, guidance, and community. Not only did she develop my scientific skill set, nurture my scientific inquiry, and expand my professional horizons, but she also directly connected me to and supported my unique California Air Resources Board internship. Her leadership maintains the highest quality of scholarship, rigor, and integrity, and this dissertation would not be possible without her devoted leadership.

I am also deeply grateful for my committee members Professor Sergey Nizkorodov and Professor Craig Martens. Prof. Nizkorodov has been an advocate for me since my first visit on campus, written countless letters of support for me, supported me in my TA appointments, and has continued to be a good friend throughout my graduate studies. Prof. Craig Martens mentored me through the ChAMP program math and chemistry courses which were essential for a non-traditional student like myself to be successfully reimmersed in the academic environment and has continued to be a supportive and joyful mentor throughout my academic career.

I would like to also acknowledge to the amazing group of staff scientists, postdocs, and students in the Finlayson-Pitts lab. Dr. Weihong Wang, Dr. Lisa Wingen and Dr. Veronique Perraud especially were indispensable experts in experimental design, instrument operation, data interpretation, and keeping my head above water throughout the graduate research process.

Additionally, I would like to thank the greater community of the Chemistry Department who make this level of research possible by their everyday contributions. This includes facilities staff who continued to work in-person, daily throughout the pandemic, the AirUCI Orbitrap instrument operators, the IMRI staff for assistance with SEM-EDS and AFM analysis, expert glass blowing by Jorg Meyer, and the machine shop staff who assisted with experimental design and fabrication.

Lastly, I would like to acknowledge my gratefulness to my graduate school companions, who weathered the experience with me, shared the good times and bad, and made these five years so enjoyable. In particular, I am thankful to my husband Luke, who gave up so much to move across the country to support my dream, and with whom I hope to accomplish many more.

Permission to use copyrighted material in chapters 2 of this manuscript has been granted by the American Chemical Society and includes work from co-authors Weihong Wang, Kifle Z. Aregahegn, Simone T. Andersen, Anton Z. Ni, Ole John Nielsen and Barbara J. Finlayson-Pitts. Permission to use copyrighted material in chapters 3 of this manuscript has been granted by the American Chemical Society and includes work from co-authors Michael J. Ezell, Véronique Perraud, and Barbara J. Finlayson-Pitts. Permission to use copyrighted material in chapter 5 has been granted by the European Geosciences Union under the Creative

Commons Attribution 4.0 License and includes work from co-authors Shenglun Wu, Hyung Joo Lee, Shang Liu, Toshihiro Kuwayama, John H. Seinfeld, and Michael J. Kleeman. Financial support was provided by the University of California, Irvine, NSF Grant #1404233, the NSF Ridge 2 Reef fellowship (award DGE-1735040), the 2018 American Veterans of Korea scholarship, the 2018 donors to the Michael. E. Gebel award, and the 2020 SCTA scholarship.



## VITA

### Andrea Anderson

- 2011 B.S. in Chemistry, Dominican University, River Forest, IL
- 2011 Study Abroad, University of Havana, Cuba
- 2011-12 Product Development Intern, Clarke Mosquito Control
- 2012-13 Associate Scientist – Analytical Chemistry, Abbott Laboratories
- 2013-16 Senior Environment, Health, and Safety Specialist, AbbVie
- 2016-17 Method Development Chemist, Bureau Veritas
- 2017-22 Graduate Student Researcher, University of California, Irvine
- 2017-19 Teaching Assistant, Chemistry, University of California, Irvine
- 2021 Atmospheric Processes Research Section Intern,  
California Air Resources Board
- 2017-21 Ecosystem Management and Environmental Change Certificate  
“Ridge to Reef” NSF research traineeship, University of California, Irvine
- 2022 Ph.D. Atmospheric Chemistry, University of California, Irvine

## PUBLICATIONS

**Anderson, A.**, Kuwayama, T., Lee, H.J., *Fire Influence on O<sub>3</sub> levels: Insights into California O<sub>3</sub> Sensitivity using Ground and Satellite Measurements*, in preparation, 2022.

**Anderson, A.**, Lakey, P., Shiraiwa, M., Finlayson-Pitts, B.J., *Heterogeneous OH radical reactions with thin films of neonicotinoid pesticides: kinetics, products, mechanism, and environmental implications*, in preparation, 2022.

Wu, S.; Lee, H. J.; **Anderson, A.**; Liu, S.; Kuwayama, T.; Seinfeld, J. H.; Kleeman, M. J., [Direct measurements of ozone response to emissions perturbations in California](#). *Atmos. Chem. Phys.* 2022, 22 (7), 4929-4949.

**Rohrbacher, A.**;<sup>\*</sup> Ezell, M. J.; Perraud, V.; Finlayson-Pitts, B. J., [Probing Matrix Effects on the Heterogeneous Photochemistry of Neonicotinoid Pesticides, Dinotefuran and Nitenpyram](#). *ACS Earth Space Chem* 2021, 5 (5), 1196-1209.

Wang, W.; Aregahegn, K. Z.; Andersen, S. T.; Ni, A. Z.; **Rohrbacher, A. F.**;<sup>\*</sup> Nielsen, O. J.; Finlayson-Pitts, B. J., [\*Quantum yields and N<sub>2</sub>O formation from photolysis of solid films of neonicotinoids\*](#). J Agr Food Chem 2019, 67 (6), 1638-1646.

*\*Note previously published under the name Andrea Rohrbacher*

#### ORAL PRESENTATIONS

“Using Satellite Data to Track How Wildfires are Changing Ozone Pollution Chemistry in California” California Air Resources Board interdivisional forestry management group. 7 May 2021.

“Matrix Effects in the Heterogeneous Photochemistry of Neonicotinoid Pesticides.” ISKPPA. 19 Feb 2021.

“Matrix Effects in the Heterogeneous Photochemistry of Neonicotinoid Pesticides.” American Geophysical Union. 07 Dec 2020.

“Atmospheric Fate of Neonicotinoid Pesticides as Pure Compounds and in Formulations.” American Geophysical Union. 11 Dec 2019.

***\*Outstanding Student Presentation Award (OSPA)***

“Comparison of Degradation of Neonicotinoids in Commercial Formulations and as Pure Reagents.” AirUCI Internal Symposium. 9 May 2019.

#### POSTER PRESENTATIONS

“Heterogeneous OH reactions with thin films of neonicotinoid pesticides” American Chemical Society. 23 Apr 2022.

“Ozone in fire-influenced California air samples using ground and satellite measurements” UCI AGS. 24 Apr 2021. ***\*First place award***

“Atmospheric Fate of Neonicotinoid Insecticides as Pure Compounds and in Formulations.” SESAC, Shanghai. 10 Nov 2019.

“Atmospheric Fate of Neonicotinoid Insecticides as Pure Compounds and in Formulations.” American Chemical Society. 26 Aug 2019 and 28 Aug 2019. ***\*Selected for Sci-Mix***

“Pesticides in the Environment: Comparison of Degradation of Neonicotinoids in Commercial Formulations and as Pure Reagents.” ISKPPA. 10 May 2019.

“Pesticides in the Environment: Comparison of Degradation of Neonicotinoids in Commercial Formulations and as Pure Reagents.” UCI AGS. 26 April 2019. ***\*First place award***

“Bee Declines and Human Health: Are Pesticides More Dangerous After Air Exposure?” UCI Ridge to Reef poster symposium. 6 Dec 2018.

## PATENT

Willis, M.; Saunders, M.; Ramoutar, D.; Szymczyk, J.; Krenick, F.; **Rohrbacher, A.;**\*  
“*Insecticidal Compositions and Methods Using the Same*”, US20130101687 A1, Apr 25, 2013.

## COMMUNITY OUTREACH

Project management practicum 2020  
· Developed interactive museum exhibits for youth age 5-18 at the Discovery Cube Science Center

NSF Discovery Research K-12 Project – Science Expert 2019

- Served as Science Expert in revamping local, predominantly Hispanic high school science curriculum in project called “Expanding Latinxs’ Opportunities to Develop Complex Thinking in Secondary Science Classrooms Through a Research-Practice Partnership”

Local presentations to general public 2018 – 2019

- “Fate of the World’s Most Commonly Used Pesticide.” Brews and Brains Events at Fireside Pub, Costa Mesa, CA. 2019.
- “Chemistry, Climate Change, and Crud: Atmospheric Chemistry.” Assembly for hundreds of University High School students, Irvine, CA. 20 Feb 2019.
- “Chemistry: For a Safer Planet and Healthy World.” Irvine School District Career Fair. 5 Dec 2018.

Irvine Unified School District 2017 – 2018

- Ask a Scientist Night: Resource for local for local 6<sup>th</sup>-8<sup>th</sup> grade science students
- ‘21<sup>st</sup> Century Careers’ presenter: Used demonstrations to present to 30 middle school students about STEM career path and environmental chemistry field

## AWARDS AND DISTINCTIONS

NSF Research Traineeship Fellowship (\$34,000)	2019, 2020
UCI Symposium – Poster Session First Place Winner	2019, 2021
AGU Outstanding Student Presentation Award (top 5%)	2019
4 <sup>th</sup> Sino-European School on Atmospheric Chemistry, Shanghai	2019
Michael E. Gebel Award (for environmental chemistry contributions in community service)	2018
Outstanding Contributions to Education by a Chemistry Department TA – UCI	2018
AbbVie Environment, Health, and Safety Excellence Award	2015

## **ABSTRACT OF THE DISSERTATION**

Emerging air quality concerns in California: Atmospheric fates of neonicotinoid pesticides and increasing wildfire influence on ozone attainment

by

Andrea Anderson

Doctor of Philosophy in Atmospheric Chemistry

University of California, Irvine, 2022

Professor Barbara J. Finlayson-Pitts, Chair

Application of atmospheric chemistry has been the cornerstone of California's landmark air quality improvement over the 20<sup>th</sup> century. Yet challenges with pesticides, poor air quality, and disproportionate pollution burdens in environmental justice communities continue to evolve in the 21<sup>st</sup> century. The majority of this work developed techniques to characterize the atmospheric fates of neonicotinoid pesticides, which are now the world's most commonly used insecticides. Laboratory studies were conducted to evaluate the heterogeneous photochemistry and OH radical oxidative reactions with selected neonicotinoid pesticides, as well as potential matrix effects due to commercial formulations and application type. Estimated atmospheric lifetimes are reported and the reaction products are identified.

A second project, completed in collaboration with the California Air Resources Board and in partial fulfillment of the Ridge to Reef professional development traineeship, evaluated the impact of increasing wildfires on ozone formation and NAAQS attainment across three air basins in California, the San Joaquin Valley, the South Coast Air Basin, and

the Sacramento Valley. Results demonstrated the need for simultaneous NO<sub>x</sub> and VOC reductions across the air basins to meet ozone attainment requirements, with implications for prescribed burning techniques to reduce ozone and PM<sub>2.5</sub> pollution.

## CHAPTER 1: INTRODUCTION



*Figure 1.1 1948 photo of the Los Angeles Civic Center at the height of a smog attack, the buildings one block away are barely visible, from the Los Angeles Times Photographic Archive.<sup>1</sup>*

### **1.1 Atmospheric chemistry research in California air quality**

California faces formidable environmental challenges in the coming decades in simultaneously reducing climate-warming greenhouse gas emissions, meeting National Ambient Air Quality Standards (NAAQS) for criteria pollutants, and addressing local toxic pollutant issues that have historically disproportionately affected environmental justice communities. Atmospheric chemistry has been the cornerstone of California's environmental policy journey, with seminal work focused on photochemistry and gas phase reactions. Examples include Arie Haagen-Smits work on photochemical smog formation from vehicle exhaust and industrial gas emissions research<sup>2-4</sup> and F. Sherwood Rowland and Mario Molina's Nobel-prize winning chlorine catalyzed ozone destruction research.<sup>5</sup>

As the field has matured, atmospheric chemistry has grown to incorporate heterogeneous reactions between gases and solids, such as aerosol particles and environmental surfaces. This field of multi-phase atmospheric chemistry has important implications for the destruction of stratospheric ozone and the growth of health-hazardous particles. Understanding the heterogeneous photochemistry and reactions of atmospheric gases with surfaces is thus a critical field of study for both fundamental understanding of physical and chemical properties, and also in applied sciences for understanding fates of specific emissions.

In this dissertation, multi-phase chemistry laboratory experiments were applied to the environmental fates of neonicotinoid (NN) pesticides in order to calculate the probable lifetimes of these species and to identify their degradation products. An additional project was completed in collaboration with the California Air Resources Board and in partial fulfillment of the Ridge 2 Reef professional development traineeship requirements. This evaluated how the increasing numbers and intensities of wildfires are affecting ozone formation and attainment across California. Both projects highlight the importance of fundamental atmospheric chemistry inquiry and the subsequent translation to effective policy that will be key to meeting California's coming challenges.

## **1.2 Challenges of pesticides**

California, like the rest of the world, has many classes of emerging contaminants that are found in the environment, including pharmaceuticals, personal care products, and pesticides.<sup>6-8</sup> The scope of understanding the fate of these emerging contaminants is daunting: hundreds of new products are produced annually and it is often unclear what their

environmental impact is until decades after their use has been introduced. Exposed to sunlight and oxidants in the environment, these contaminants undergo reactions resulting in countless new degradation products.

One advisory example is the pesticide malathion, which was used extensively to treat the Mediterranean fruit fly through the 1990s. It was later discovered in field studies in Southern California that when exposed to atmospheric oxidants, malathion produced the degradation product malaoxon, which displayed a 64× increase in toxicity from the original pesticide.<sup>9</sup> This research highlighted that it is not just the original contaminant that may be a concern, but also degradation products in air. Thus, a full understanding of the atmospheric reactions is necessary to accurately plan for the environmental fate of emerging contaminants.

### **1.3 Neonicotinoid history and concerns**

Neonicotinoids (NN) are now the world's most commonly used class of insecticides. They are used extensively in California's agricultural areas, particularly in the central San Joaquin Valley Air Basin agricultural hub, but also in household sectors such as lawn care, in-home pest abatement, and veterinary care. Neonicotinoids are neurotoxins that act by binding to specific sub-sites of the nicotinic acetylcholine receptor.<sup>10,11</sup> Although these receptors are present in both insects and mammals, *in vivo* toxicity studies have shown that NNs are much more toxic to insects, likely due to their higher binding affinity to insect receptors.<sup>12,13</sup> As a result, NNs exhibit relatively low toxicity to mammals, making them an attractive alternative to earlier products that have a higher potential to adversely affect human health.<sup>14</sup>



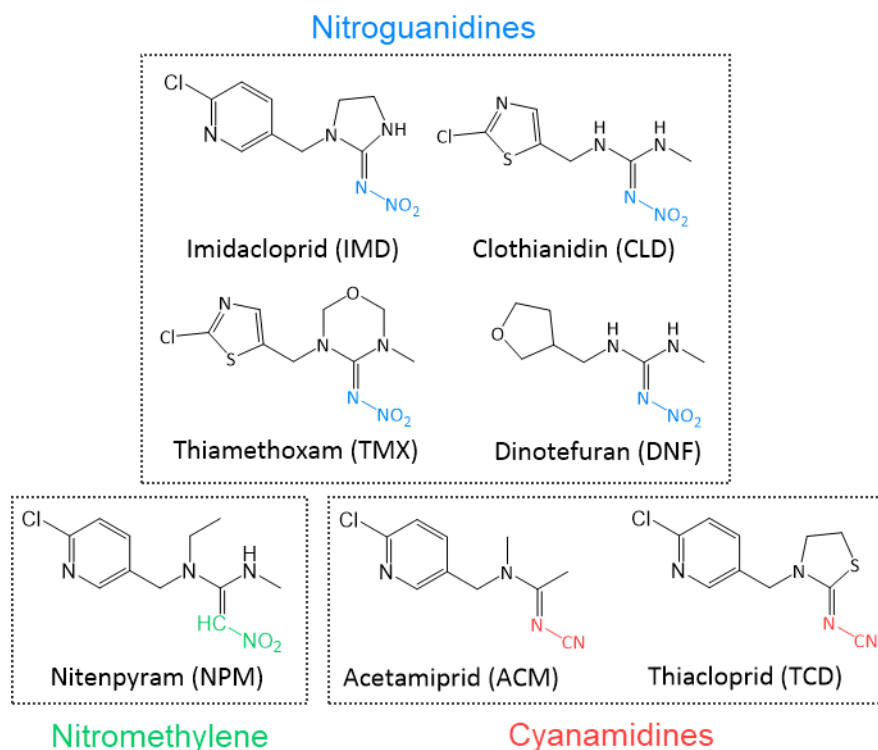


Figure 1.2 Neonicotinoid structures grouped by chromophore

Neonicotinoids are systemic pesticides, meaning they translocate throughout all plant tissue. This systemic nature is utilized to lower human exposure due to lower application frequencies<sup>15</sup> and application as seed coatings, where the NN becomes incorporated throughout the plant tissue during growth, further reducing human exposure from the application process.<sup>16,17</sup>

Despite their many advantages, the effect of NNs on non-target organisms has given cause for concern.<sup>14,18-20</sup> Numerous studies have identified a negative impact on pollinator health, including on disease tolerance and susceptibility, navigation ability, and honeybee colony collapse disorder.<sup>21-32</sup> While the EU introduced a moratorium on three of the NNs in 2013 (imidacloprid, clothianidin, and thiamethoxam) to protect honeybees,<sup>33</sup> the NNs

remain a major part of the international and US agricultural system (although use of the nitroguanidine subgroup was recently proposed to be restricted by the California Department of Pesticide Regulation in February 2022).<sup>34</sup>

Like other emerging contaminants, NNs can migrate through the environment and undergo chemical reactions in air, water, and soil. Indeed, NNs are commonly observed off-target: on soil and vegetative surfaces;<sup>25,35-38</sup> in pollen, honey, and nectar;<sup>39,40</sup> on blowing dust particles during planting;<sup>21,22</sup> and on neighboring wildflowers and untreated plants.<sup>35,41</sup> This is of concern not only because NNs have shown deleterious effects on honeybees and other non-target insects that play vital roles in our ecosystems, but also because their degradation products, such as a desnitro derivative, can have increased toxicity to mammals.<sup>42</sup> In the Woodcock et al. study,<sup>43</sup> NN effects on multiple bee species were evaluated at a number of different sites in the UK, Germany, and Hungary. The results were compound-, country- and species-specific, but interestingly, not always negative.<sup>43</sup> These location-specific effects suggest that environmental reactions of the NNs may be playing a significant role that leads to varying impacts in different locations. Their multi-media dispersal and complex multifunctional moieties make their environmental fates difficult to predict.<sup>44-47</sup>

Due to their systemic nature and widespread use, both the parent NNs and their degradation products have accumulated in the environment. For example, studies have shown the plant may leave behind more than 95% of the NN treatment in the soil,<sup>14,23,48</sup> and studies in Europe showed that NNs were still present in the soil even five years after the moratorium, with no clear declining trend.<sup>49</sup> Globally NNs have been found in 75% of honey

samples,<sup>39</sup> in non-target species further up the food chain such as birds,<sup>50,51</sup> and perhaps not surprisingly then, are often detected in human biological samples.<sup>52-55</sup>

Thus, NNs are mobile and have ample opportunity for multi-phase atmospheric chemistry on environmental surfaces that may affect their lifetimes and degradation products. Of crucial importance in understanding the environmental impact of NNs is identifying the environmental degradation products so that their toxicity on non-target species, including humans, can be assessed. An abundance of work is available on the reactions and fate of NNs in aqueous systems (they are highly water soluble),<sup>20,56-67</sup> but little is known about the heterogeneous reactions of the solids, for example on leaf, soil, and dust surfaces, with atmospheric gases.

#### **1.4 Goals of neonicotinoid multi-phase atmospheric chemistry experiments**

This work aimed to develop techniques to fully characterize the multi-phase atmospheric chemistry of NN pesticides by performing laboratory studies of their photochemistry and oxidation reactions. Chapter 3 presents the multi-phase photochemistry of an example NN (clothianidin, CLD). This chapter includes absorption cross sections, quantum yields, and expected atmospheric lifetimes.

Chapter 4 expands on the photochemistry of the NN by examining matrix effects in photochemistry with experiments using two NNs that are not covered in the EU moratorium, dinotefuran (DNF) and nitenpyram (NPM). Matrix effects were explored from the perspective of either their commercial formulations or their solid form, which is often dictated by pesticide application technique and may vary from crystalline to amorphous

films or deposits on solid surfaces such as dust. Major gas and solid-phase products are discussed, as well as comparisons of quantum yields and atmospheric lifetimes.

Chapter 5 details heterogeneous oxidation reactions of three structurally unique NNs with the most common daytime atmospheric oxidant, the OH radical. The three NNs are imidacloprid (IMD), clothianidin (CLD), and dinotefuran (DNF). Results include uptake coefficients, expected atmospheric lifetimes, solid-phase product identification, and the reaction mechanism.

### **1.5 Goals of wildfire effects on ozone attainment research**

A second project evaluated the impact of increasing number and severity of wildfires on California air quality. In contrast to the immediate safety and smoke hazards of wildfires, comparatively less is known about the residual effects of how transported smoke changes the secondary atmospheric chemistry across affected areas. It is particularly difficult to unravel the role that these increasing wildfires are playing in ozone pollution and attainment of the National Ambient Air Quality Standards (NAAQS).

Chapter 6 investigates the impact of wildfires on O<sub>3</sub> levels and formation regimes using ground and satellite observations in California. Two statistical methods were applied on 2018-2020 ground-level PM<sub>10</sub>, PM<sub>2.5</sub>, and CO measurements collected at 17 air monitoring sites across California to differentiate extreme air pollution event days (which are likely associated with wildfires, prescribed fires, or agricultural burning). Monthly aggregated data were then statistically evaluated to determine whether these extreme air pollution event days were associated with greater probability of 8-hour O<sub>3</sub> NAAQS exceedances.

Additionally, tropospheric column integrated formaldehyde (HCHO) and nitrogen dioxide (NO<sub>2</sub>) data from Tropospheric Monitoring Instrument (TROPOMI) on-board the Sentinel-5 Precursor (S5P) satellite were used as surrogates to study the simultaneous O<sub>3</sub>-NO<sub>x</sub>-VOC sensitivities relative to the ground-level air monitoring data. These results provide new insight into the 8-hour O<sub>3</sub> NAAQS exceedances during California fires and therefore precursor emission policy goals across the state.

## CHAPTER 2: PHOTOCHEMISTRY OF NEONICOTINOIDS

### 2.1 Research goals

This project analyzed the heterogeneous photochemistry of pure NN in thin films. Photodegradation analysis was underway when I joined the Finlayson-Pitts group in 2017, and I carried out studies for one of the NN, clothianidin (CLD). The NN solids were prepared as thin films on ATR crystals and then monitored in-situ via ATR-FTIR to calculate quantum yields. The quantum yields are used to calculate rate constants at atmospherically relevant light intensities from first principles to determine rate constants and atmospheric lifetimes in a variety of conditions.

### 2.2 Methods

#### 2.2.1. Thin film preparation

Solutions of the NN were prepared in acetonitrile (ACN) and interrogated by ATR-FTIR. The Ge ATR crystals (Pike technologies, 45°, 80 mm × 10 mm × 4 mm, 10 internal reflections) were prepared by rinsing with water and ACN, followed by argon plasma cleaning for 10 minutes. ATR samples were prepared by pipetting 10  $\mu$ L of NN solutions onto the crystals where the solvent evaporated immediately leaving behind a thin film. The samples were further dried for 15 minutes in a flow of 100 cm<sup>3</sup> min<sup>-1</sup> of N<sub>2</sub> before photolysis.

#### 2.2.2. Photolysis setup

The ATR-FTIR spectra of the NNs were recorded (4 cm<sup>-1</sup> resolution, 128 scans) before and during irradiation. During photolysis the thin film was exposed to light from two different lamps. An ozone-free mercury lamp with its main peak at 254 nm, and a broadband organophosphor-coated mercury lamp centered at 313 nm was also used. Since light at the

earth's surface is limited to >290 nm (the actinic region),<sup>68</sup> the 254 nm lamp is thus used not to represent ambient conditions, but to quickly evaluate experimental setup and to identify wavelength dependencies of quantum yields. A water filter was placed between the sample and the lamp to absorb heat, and a borosilicate glass slide was used to filter out light below 290 nm for the 313 nm lamp. The lamps were warmed up for at least 30 minutes prior to use.

### 2.3 Absorption cross sections

Absorption cross sections of the neonicotinoids were measured in acetonitrile using a UV-Vis spectrometer. The measured absorbance (base 10) was converted to absorption cross sections ( $\text{cm}^2 \text{ molecule}^{-1}$ , base e) via Beer's law, rearranged and shown in **equation 2.1**,

$$\sigma (\text{cm}^2 \text{ molecule}^{-1}) = \frac{A}{b (\text{cm}) \cdot c \left(\frac{\text{mol}}{\text{L}}\right)} \cdot \ln(10) \cdot \frac{1000 \text{ cm}^3}{\text{L}} \cdot \frac{\text{mol}}{6.022 \times 10^{23} \text{ molecules}} \quad (2.1)$$

where  $\sigma$  is absorption cross section in  $\text{cm}^2 \text{ molecule}^{-1}$ , A is absorbance (base 10), b is pathlength in cm, and c is concentration in  $\text{mol L}^{-1}$ .

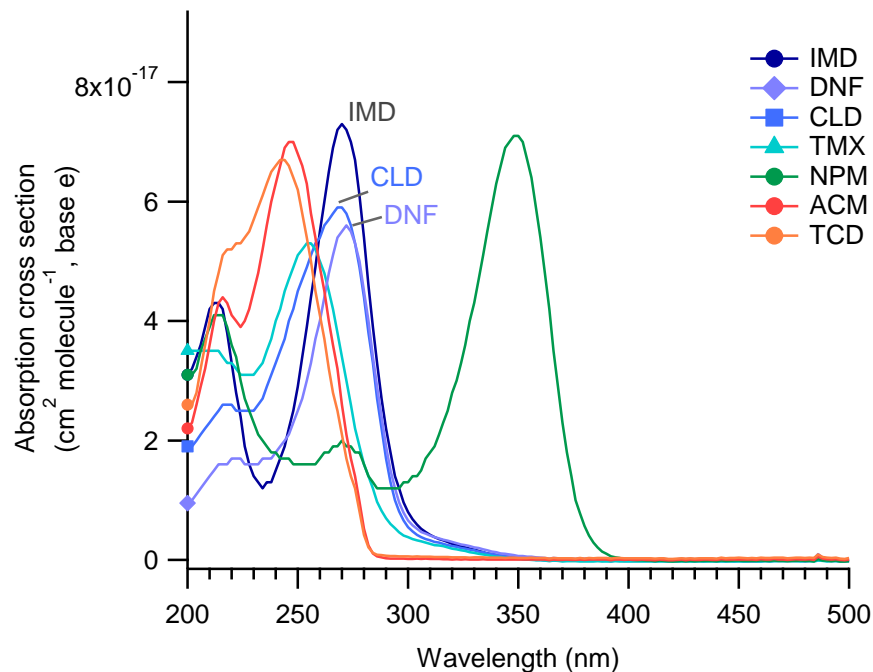


Figure 2.1 Absorption cross sections of the neonicotinoids in acetonitrile and TMX in methanol, where nitroguanidines are in blues, nitromethylenes are in green, and cyanamidines are in reds.

The absorption cross sections are shown in **Fig. 2.1** and show clear distinction based on their chromophore: nitroguanidine ( $=N-NO_2$ ), nitromethylene ( $=CH-NO_2$ ), or cyanamidine ( $=N-CN$ ). The cyanamidines (ACM and TPD) do not absorb in the actinic region ( $> 290$  nm). The nitroguanidines (IMD, DNF, CLD, and TMX) absorb up to  $\sim 360$  nm, and the nitromethylene nitenpyram absorbs strongly up to  $\sim 400$  nm, and are thus both expected to be photochemically active in the atmosphere.

## 2.4 Quantum yields and atmospheric lifetimes

Photodegradation analysis was conducted on a thin film of the NN and loss was monitored with attenuated total reflectance (ATR) FTIR, which allows direct analysis of the solid state in real time. The NN thin film on the ATR crystal is probed by the evanescent wave



at varying depths of penetration ( $d_p$ ), which is dependent on refractive index of the crystal, angle of incidence, and wavelength, shown in **equation 2.2**,<sup>69</sup>

$$d_p = \frac{\frac{\lambda}{n_1}}{2\pi[\sin^2\theta - \left(\frac{n_2}{n_1}\right)^2]^{1/2}} \quad (2.2)$$

where  $\lambda$  is the wavelength (at the IR peak of interest),  $n_1$  is the refractive index of the denser medium (4 for Ge),  $n_2$  is the refractive index of the rarer medium (1.0003 for air, which is appropriate for thin films), and  $\theta$  is the angle of incidence ( $45^\circ$  in the Ge ATR crystal). The calculated  $d_p$  on a Ge crystal is  $0.4 \mu\text{m}$  at  $1616 \text{ cm}^{-1}$ , relevant to the asymmetric  $-\text{NO}_2$  stretch in CLD.

Examples of both the initial absorbance spectrum and the difference spectrum for a thin film deposited from a 6.40 mM CLD solution irradiated with the 254 nm lamp are shown in **Fig. 2.2**. The initial absorbance spectrum (black) is generated using the initial single beam spectrum of the sample ( $S_0$ ) and a single beam spectrum of the clean ATR crystal. Difference spectra (blue trace), defined as  $\log S_0/S_t$  where  $S_0$  is the single beam of the NN before photolysis and  $S_t$  is the single beam at the selected reaction time, were obtained at timed intervals. In the difference spectra, positive peaks are products being formed while negative peaks are due to loss. An initial absorbance ( $A_0$ ) is recorded from the initial absorbance spectra and its loss ( $dA$ ) is recorded from the negative peak height seen in the difference spectra.

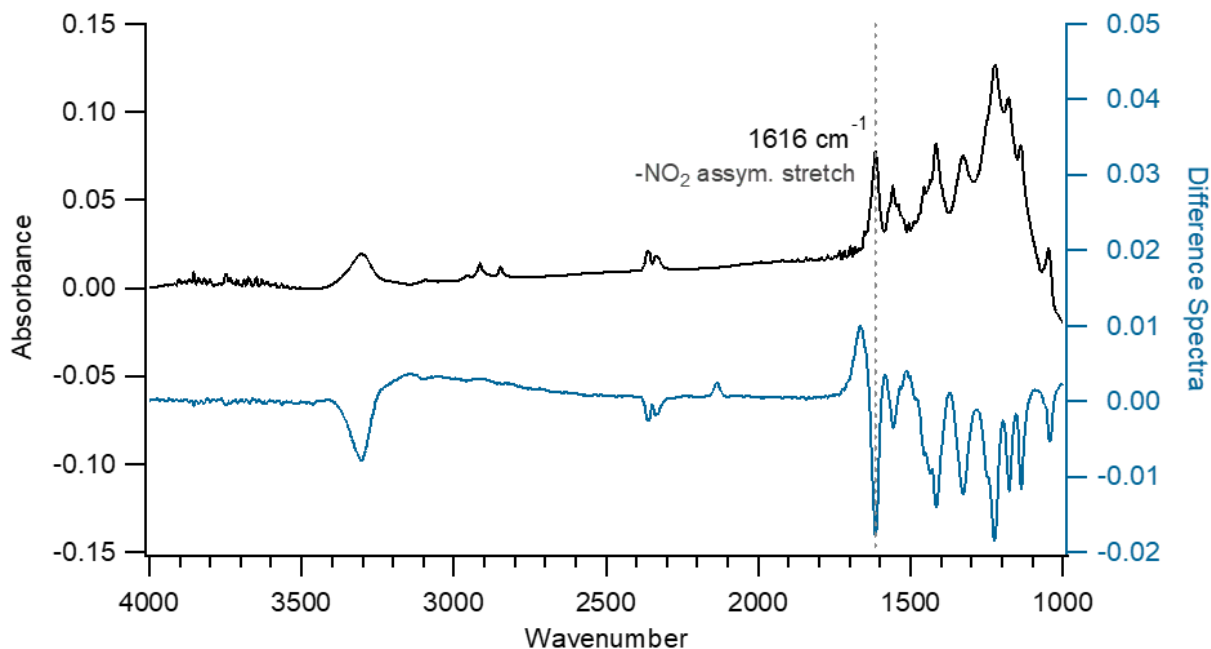


Figure 2.2 FTIR spectra of CLD before photolysis (black) and difference spectra after photolysis (blue), which is  $\log(S_0/S_t)$ , where  $S_0$  is the single beam spectra before photolysis and  $S_t$  is the single beam spectra at a given photolysis time, and positive peaks indicate product formation and negative peaks indicate reactant loss.

The photolysis-rate constants ( $k_p$ ) of IMD and CLD were obtained from plots of the first-order decays of the NN as a function of time following loss of the  $-\text{NO}_2$  asymmetric stretch (**Fig. 2.3**). The first order loss is plotted as  $\ln(A/A_0)$ , where  $A$  is  $(A_0 - dA)$ , versus time, and the negative of the slope is the rate constant ( $k_p$ ).

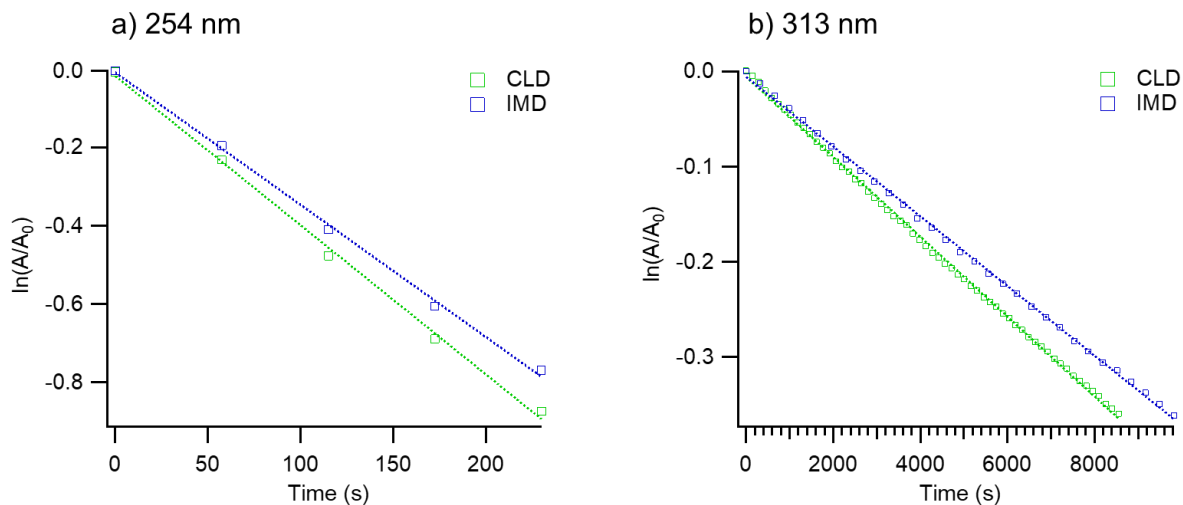


Figure 2.3 First-order degradation plots of CLD and IMD during 254 nm and 313 nm photolysis following loss of the  $-NO_2$  peak.

Once  $k_p$  is known, quantum yields ( $\Phi$ ) are calculated using **equation 2.3**,

$$k_p = \sum I(\lambda)\Phi(\lambda)\sigma(\lambda) \quad (2.3)$$

where  $I$  is the photon spectral flux density of the photolysis lamp in photons  $cm^{-2} s^{-1} nm^{-1}$  (as a function of wavelength, measured using an Ocean Optics UV-Vis spectrometer),  $\Phi$  is the quantum yield which is molecules decomposed per photon absorbed, and  $\sigma$  is the absorption cross section in  $cm^2 molecule^{-1}$ . This equation is appropriate for use in the low optical density limit, which was verified by calculating the transmittance in these conditions using **equation 2.4**,<sup>68</sup>

$$\frac{I}{I_0} = 10^{-\sigma Nl} \quad (2.4)$$

where  $\sigma$  is again the absorption cross section in  $cm^2 molecule^{-1}$ , base  $e$ ,  $N$  is the number of molecules,  $l$  is the pathlength, and the dimensionless exponent is the optical depth. For the NN thin films, the absorption cross section near 313 nm is  $\sim 5 \times 10^{-18}$  and the product  $Nl$  is

$\sim 1 \times 10^{16}$  molecules  $\text{cm}^{-2}$  based on data from calibration curves (discussed in detail later in **Fig. 4.5**). The resultant transmittance  $I/I_0$  is 0.89, indicating that 89% of the light makes it through the entire film.

Photon spectral flux density for the lamp had been measured in earlier studies in this lab using o-nitrobenzaldehyde as an actinometer.<sup>70</sup> As the sample setup had changed slightly at the time the studies of CLD were conducted, direct calculation of quantum yields using the lamp intensity was deemed less accurate than recreating the photolytic degradation of a different NN whose quantum yield had already been calculated (IMD), and comparing the ratio of the new recorded photolysis rate constant to obtain the quantum yield for CLD, as shown in **equation 2.5**,

$$\frac{k_{p,IMD}}{k_{p,CLD}} = \frac{\Phi_{IMD} \sum_{\lambda} [I_{rel}(\lambda) \cdot \sigma_{IMD}(\lambda)]}{\Phi_{CLD} \sum_{\lambda} [I_{rel}(\lambda) \cdot \sigma_{CLD}(\lambda)]} \quad (2.5)$$

Data for  $I_{rel}$  and  $\sigma$  were each averaged into 2 nm bins, and the product of  $I_{rel}$  and  $\sigma$  in each bin was summed. The results are reported in **Table 2.1**. As shown in **Fig. 2.1**, CLD has a slightly smaller absorption cross section than IMD, so when the ratio of the observed  $k_p$  is 1.0, the resultant quantum yield is slightly higher for CLD than IMD.

*Table 2.1: Quantum yield calculation for CLD*

Photolysis wavelength (nm)	n	Average $k_{p,IMD}$ ( $\text{s}^{-1}$ )	Average $k_{p,CLD}$ ( $\text{s}^{-1}$ )	Ratio	$\phi$
<b>254</b>	3	$(3.3 \pm 0.04) \times 10^{-3}$	$(3.4 \pm 0.4) \times 10^{-3}$	1.0	$7.4 \times 10^{-3}$
	4	$(2.0 \pm 0.3) \times 10^{-3}$	$(2.3 \pm 0.1) \times 10^{-3}$	1.2	$8.5 \times 10^{-3}$
Average ( $\pm 1s$ )					<b><math>(8.0 \pm 3.3) \times 10^{-3}</math></b>
<b>313</b>	4	$(3.6 \pm 0.05) \times 10^{-5}$	$(3.6 \pm 0.6) \times 10^{-5}$	1.0	<b><math>(2.2 \pm 0.9) \times 10^{-3}</math></b>

The quantum yield results obtained for CLD are compared to the other NN in similar experiments as well as to literature values in different conditions in **Table 2.2**.<sup>71</sup> **Table 2.2** shows that the quantum yields for NNs on surfaces are typically lower than those reported for aqueous solutions. This result demonstrates the cage effect is important in photolysis of the NN solid. The initially formed fragments are trapped in the high-viscosity solid phase leading to enhanced recombination and regeneration of the parent molecule. Thus, NN residues may persist longer in the environment on surfaces than in solution.

Table 2.2: Quantum Yields ( $\phi$ ) for photolysis of neonicotinoids at different wavelengths

NN	Wavelength	Condition	$\phi (\times 10^{-3})^a$	Reference
IMD	254 nm lamp	ATR crystal	$8.5 \pm 2.1$	Aregahegn et al. <sup>72</sup>
	313 nm lamp	ATR crystal	$1.6 \pm 0.6$	Aregahegn et al. <sup>72</sup>
	270 nm	bidistilled water	$0.86 \pm 0.17$	Redlich et al. <sup>73</sup>
	290–360 nm	borate buffer solution	$9.2 \pm 0.5$	Lu et al. <sup>74</sup>
	300 nm	borate buffer solution	15.1	von Gunten <sup>75</sup>
	natural sunlight	borate buffer solution	5.5	von Gunten <sup>75</sup>
CLD	254 nm lamp	ATR crystal	$8.0 \pm 3.3$	this work <sup>71</sup>
	313 nm lamp	ATR crystal	$2.2 \pm 0.9$	this work <sup>71</sup>
	290–360 nm	borate buffer solution	$13 \pm 1$	Lu et al. <sup>74</sup>
	300 nm	borate buffer solution	19.2	von Gunten <sup>75</sup>
	natural sunlight	borate buffer solution	7.3	von Gunten <sup>75</sup>
TMX	254 nm lamp	ATR crystal	$20 \pm 2$	Wang et al. <sup>71</sup>
	313 nm lamp	ATR crystal	$3.9 \pm 0.3$	Wang et al. <sup>71</sup>
	290–360 nm	borate buffer solution	$19 \pm 1$	Lu et al. <sup>74</sup>
DNF	254 nm lamp	ATR crystal	$8.6 \pm 2.3$	Wang et al. <sup>71</sup>
	313 nm lamp	ATR crystal	$3.3 \pm 0.5$	Wang et al. <sup>71</sup>
ACM	254 nm lamp	ATR crystal	$0.75 \pm 0.30$	Wang et al. <sup>71</sup>
	290–360 nm	borate buffer solution	$2.2 \pm 0.3$	Lu et al. <sup>74</sup>
	300 nm	borate buffer solution	33.9	von Gunten <sup>75</sup>
TCD	254 nm lamp	ATR crystal	$2.1 \pm 1.1$	Wang et al. <sup>71</sup>
	290–360 nm	borate buffer solution	$1.3 \pm 0.2$	Lu et al. <sup>74</sup>
	300 nm	borate buffer solution	46	von Gunten <sup>75</sup>

NPM	254 nm lamp	ATR crystal	$12 \pm 4$	Aregahegn et al. <sup>76</sup>
	313 nm lamp	ATR crystal	$1.0 \pm 0.3$	Aregahegn et al. <sup>76</sup>
	350 nm lamp	ATR crystal	$0.94 \pm 0.15$	Aregahegn et al. <sup>76</sup>

<sup>a</sup>Errors are  $\pm 1$ s. Quantum yield is defined as the rate of loss of the NN divided by the rate of absorption of photons. Each entry should be multiplied by  $10^{-3}$ , e.g. the first quantum yield is  $(8.5 \pm 2.1) \times 10^{-3}$

The measured UV-Vis absorption cross sections and quantum yields can be combined with known solar fluxes calculated by Madronich<sup>68</sup> to estimate lifetimes of NNs on solid surfaces in the troposphere. For a solar zenith angle of  $35^\circ$ , corresponding to a location at  $40^\circ$  N latitude on April 1 at noon, the lifetimes of IMD, CLD, TMX, and DNF are estimated to be 16,<sup>70</sup> 15, 10, and 11 h, respectively.<sup>71</sup>

## 2.5 Gas and solid phase products

Formation of solid phase products is apparent by the product peaks forming in the FTIR difference spectra in **Fig. 2.2** and will be discussed in detail in chapter 3.4 and 3.5.

The major gas phase product observed was  $N_2O$ , and yields will be discussed in further detail in chapter 3.7. In short, a previous study demonstrated cleavage of  $-NO_2$  from IMD as the first photolysis step, and proposed the  $NO_2$  and the nitrogen-centered organic radical generated simultaneously then recombine as a result of the “cage effect” in the solid.<sup>70</sup> The energy released during bond formation is sufficient to induce an intramolecular rearrangement in which an OH radical is formed by hydrogen abstraction from the N-H group in the five-membered ring. Held in the cage, OH is added back to the carbon on the five-membered ring, resulting in ejection of  $N_2O$ .

## **CHAPTER 3: MATRIX EFFECTS OF COMMERCIAL FORMULATIONS ON NEONICOTINOID DEGRADATION**

### **3.1 Research goals**

This project compared the photodegradation of pure NN to those in matrices expected in the environment. Matrix effects were explored from the perspective of either their commercial formulations or their solid form, which is often dictated by pesticide application technique and may vary from crystalline, to deposits on solid surfaces such as dust, or to amorphous films.

Photodegradation was followed in situ via FTIR of NN embedded in KBr pellets, as the thin film preparation technique used previously was incompatible with the complex commercial formulation chemical makeup. The additional formulation additives did not dissolve in the solvent system necessary for thin film formation, and thus prepared thin films of the formulations showed spectra identical to the pure compounds, suggesting the active NN had been extracted from the formulation. Analyzing the pure NN embedded in KBr pellets allowed for comparison of matrix effects between thin films and dense solid KBr pellets, as well as the comparison of pure NN in KBr pellets to their commercial formulations in KBr pellets.

A representative NN from each photoactive subgroup was used: the nitroguanidine dinotefuran (DNF) and the nitromethylene nitenpyram (NPM), as well as their respective commercial formulations, Safari and Capstar. Quantum yields were calculated for the commercial formulations and compared to those of the pure NN. Gas phase product formation was monitored using FTIR. Solid phase product identification was conducted

using direct analysis in real time (DART)-MS which allowed for direct sampling of the KBr pellets.

## **3.2 Methods**

### **3.2.1. Commercial formulations**

Neonicotinoids were used in either their pure or commercial formulations. Pure NNs used were DNF and NPM. Commercial formulations were Safari® and Capstar™, respectively. Safari® 20SG is 20% DNF w/w (Valent U.S.A. LLC, EPA Reg. No. 86203-11-59639) and also contains 1-5% sodium dodecylbenzene sulfonate buffer, and 72% patent-protected inactive ingredients.<sup>77</sup> Capstar™ (10% NPM w/w, NADA #141-175), marketed as a pressed tablet, is a veterinary treatment for flea control, which is 10% NPM and includes lactose monohydrate, cellulose, starch, colloidal silicon dioxide, and magnesium stearate as inactive ingredients.<sup>78</sup>

### **3.2.2. Preparation and IR analysis of KBr pellets**

To form the KBr pellets, potassium bromide (Fisher, Infrared grade) was ground in a mortar and pestle until it became a fine powder with a noticeable sheen. Known amounts of solid NN (either pure or in the solid commercial formulation) were mixed with ground KBr in a Wig-L-Bug® amalgamator for 10 seconds. Formulated NN were prepared at 5% w/w KBr mixtures, and pure NN pellets were prepared at corresponding w/w mixtures. Formulated DNF (which is 20% DNF w/w) was prepared at 1.0% w/w, and formulated NPM (which is 10% NPM w/w) was prepared at 0.5% w/w. Lower concentrations of both pure and formulated NN in KBr pellets were also prepared to explore concentration effects. A 40 mg sample of the NN/KBr mixture was added to a 13 mm KBr pellet die (Pike Technologies) with stainless steel anvils and pressed under vacuum at 6-9 metric tons for 10 minutes. The resulting pellet had a 13 mm diameter, and the thickness was calculated to be 0.1 mm using



the measured diameter and weight and the density of KBr ( $2.74 \text{ g cm}^{-3}$ ).<sup>79</sup> Several pellets were probed using SEM-EDS, which showed agglomerates of the NN distributed throughout the pellet. Typical images are shown in **Fig. 3.1**. (The nitroguanidine IMD was used for SEM imaging instead of DNF as the presence of a Cl atom is more easily detectable by SEM; other NNs are expected to show similar results). The results show that agglomerates of the NN were distributed throughout the pellet.

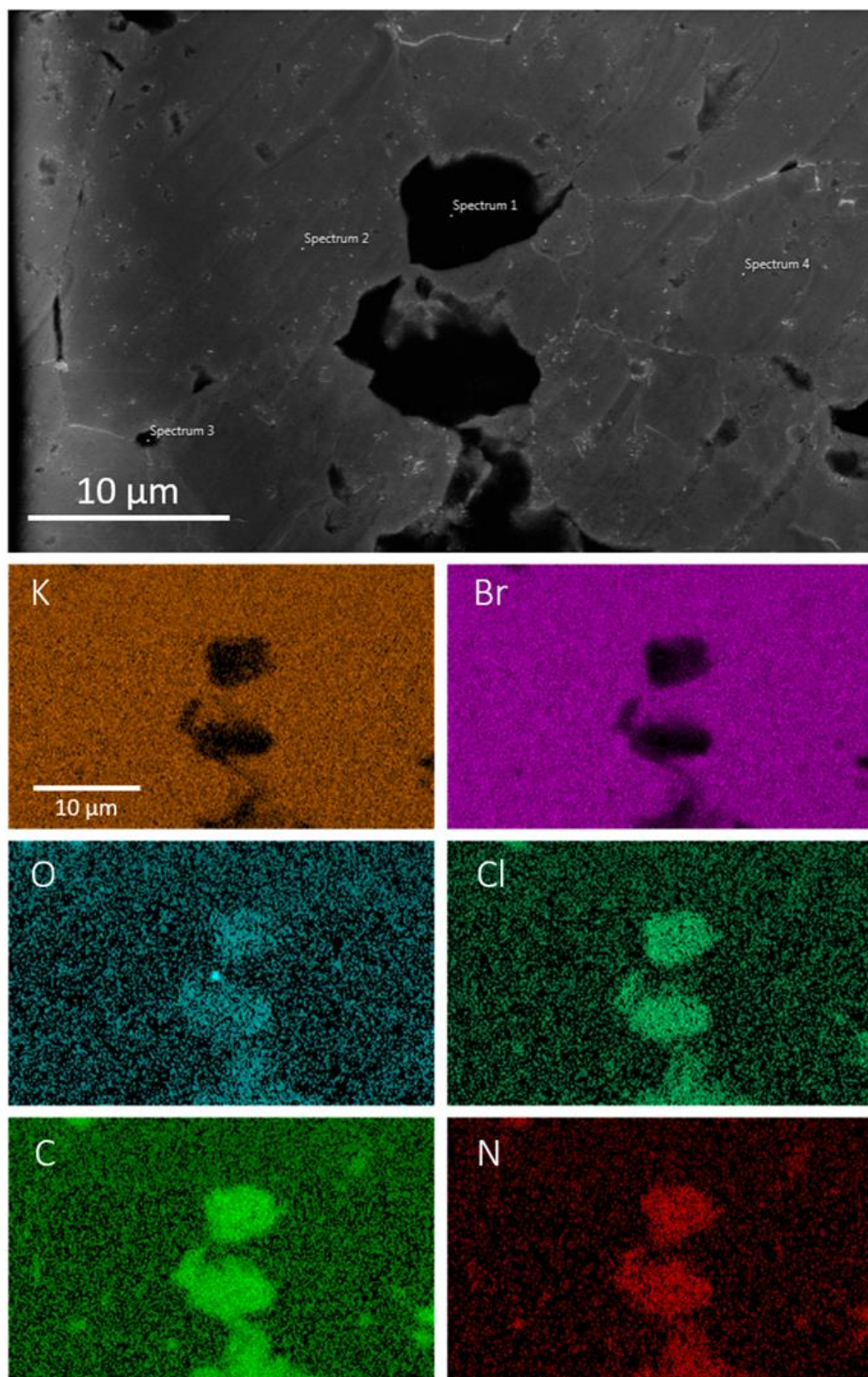
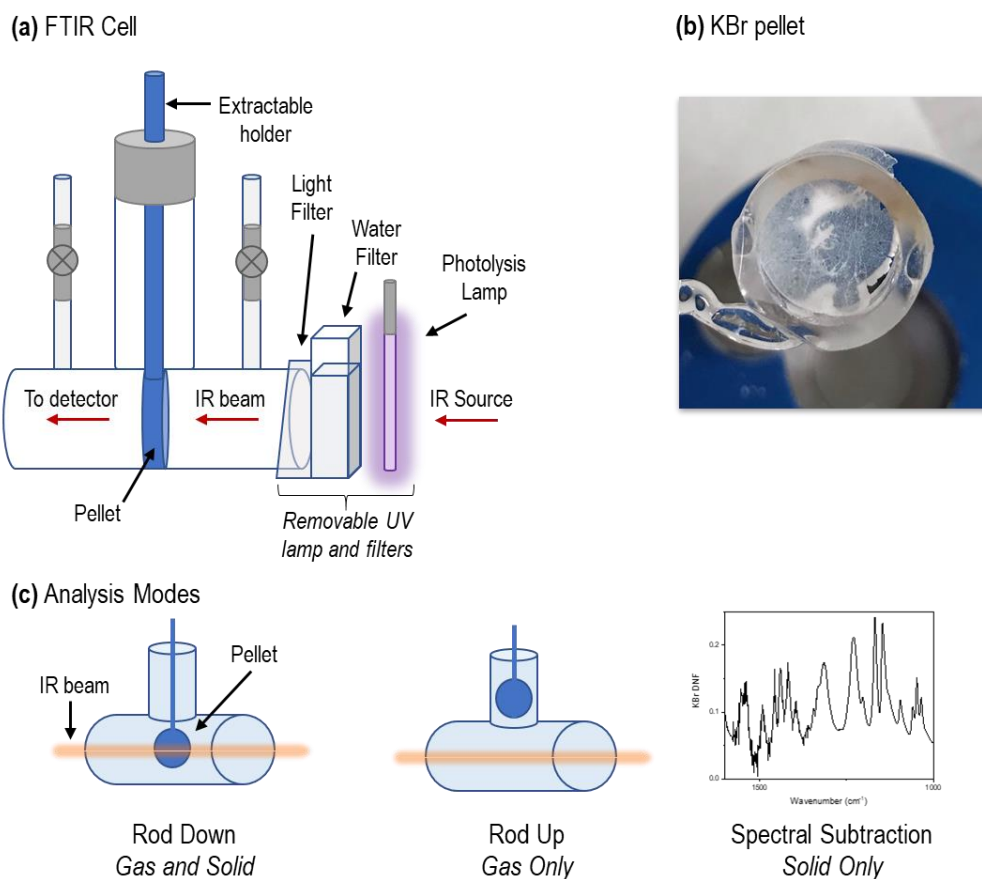


Figure 3.1 SEM-EDS image of 5% w/w imidacloprid (IMD)/KBr pellet surface mounted on carbon tape showing distribution of K, Br, O, Cl, C, and N. Colored areas show the presence of individual elements. IMD was used because of the presence of a Cl atom which has a strong SEM-EDS signal and facilitates detection.

The pellet was placed in a height-adjustable holder within a custom-built glass FTIR cell with  $\text{CaF}_2$  windows (transparent to both UV and IR light down to  $\sim 900\text{ cm}^{-1}$ ), shown in **Fig. 3.2**. The cell was evacuated and filled with 1 atm dry  $\text{N}_2$  (Praxair, Ultra High Purity). Earlier studies in our lab showed no significant differences between results in pure  $\text{N}_2$  and in dry ultra-zero air.<sup>71</sup> The pellets were probed at measured time intervals using Fourier Transform Infrared (FTIR) spectroscopy (Mattson Galaxy 5020 FTIR, cooled MCT detector) with 64 co-added scans at  $0.5\text{ cm}^{-1}$  resolution.



*Figure 3.2 (a) Schematic of the reaction cell. Samples were attached to a circular sample holder connected to a retractable rod and placed in a custom-built glass FTIR cell with  $\text{CaF}_2$  windows. Light below  $290\text{ nm}$  was removed using a glass filter and a water-filled cuvette was used to absorb heat from the lamp. The lamp, water compartment, and light filter were removed to probe the NN/KBr pellet with the IR beam. (b) A photo of a typical NN/KBr sample pellet. (c) The combined gas and solid spectra are measured with the rod in the down position and the gas phase only in the rod up position. Spectra of the solid pellet only were obtained by subtracting the gas phase spectrum from the combined gas and solid spectrum.*

Samples were irradiated using either a 254 nm low pressure mercury lamp (UVP, CPQ-5851) or one of two mercury lamps with organic phosphor coatings that gave broadband emissions. One broadband lamp was centered at 305 nm with emission from 280 to 365 nm (Jelight, 84-2061-2), and the other was centered at 350 nm with emission from 310 to 420 nm (UVP, D-28865). Lamp emission spectra are shown in **Fig. 3.3**. The 305 and 350 nm lamps provide tropospheric relevant radiation while the 254 nm lamp was used for time-sensitive experiments as they could be completed within hours, rather than days. For example, reaching 20% photolytic degradation of the parent NN requires several hours with the 254 nm lamp but one week with the 305 nm lamp. A water filter was placed between the sample and the lamp to absorb heat from the lamps and a borosilicate glass coverslip was used with the broadband lamps to filter out wavelengths below 290 nm.

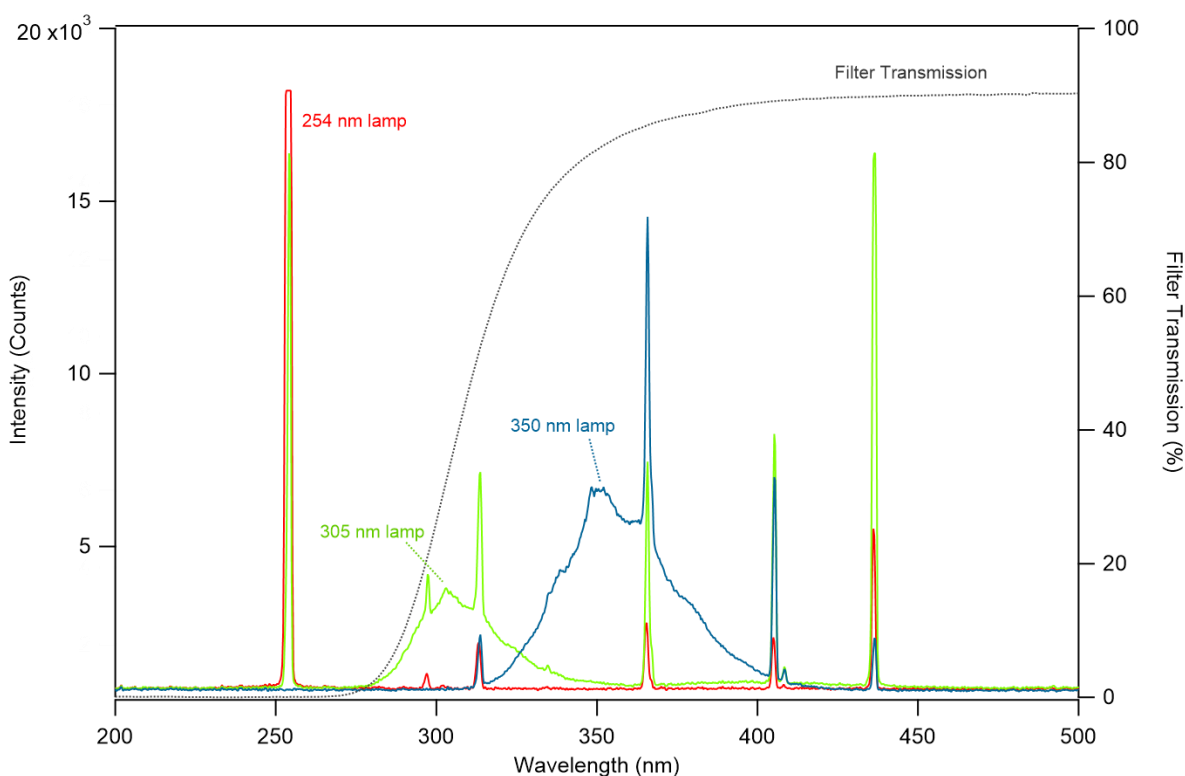


Figure 3.3 Relative emission spectra of UV lamps used for photolysis.

Spectra were recorded with the sample in one of two positions: (1) with the rod down so both the gas and solid KBr pellet were probed simultaneously; or (2) with the rod moved up so the pellet was out of the infrared beam and only the gas phase was measured (**Fig. 3.2c**). Subtraction of the gas phase spectrum from the combined gas and solid spectrum was used to obtain the solid-only spectrum. A single beam spectrum of a KBr pellet containing no NN was used as the background.

### **3.2.3. DART mass spectrometry**

Blank KBr pellets and NN/KBr pellets were further analyzed before and after photolysis using mass spectrometry. The pellets were attached to a spatula and analyzed using a triple quadrupole mass spectrometer (Xevo TQS, Waters) equipped with a commercial direct analysis in real time ion source (IonSense, DART SVP with Vapor Interface). DART-MS analysis allows direct sampling of KBr pellet surfaces without the need to dissolve the solid matrix and extract the organics. The DART-MS ion source was positioned directly in front of the mass spectrometer source inlet with a 4 cm space for the sample. Helium was used as the reagent gas flowing at 3.1 L min<sup>-1</sup> and subject to a grid electrode voltage of 350 V and a reagent gas temperature setting of 200 °C (for NPM) or 350 °C (for DNF). Mass spectra were collected from  $m/z$  2-1000 using MassLynx software in the positive-ion mode, where  $[M + H]^+$  are the expected parent peaks.

### **3.2.4. High resolution mass spectrometry (HRMS)**

To explore peaks present in the DART-MS spectra that were believed to be caused by in-source fragmentation of the NN rather than photolysis reaction, a UPLC-HRMS system was used. Solutions of NN standards were analyzed using an UPLC-DAD-HRMS platform

(ThermoScientific) equipped with a Vanquish Horizon UPLC system (including a binary LC pump, an autosampler, a column manager and a diode array detector) coupled to a high-resolution Q Exactive Plus orbitrap mass spectrometer. A Luna Omega A 1.6  $\mu\text{m}$  Polar C18 150  $\times$  2.1 mm column (Phenomenex) fitted with a SecurityGuard ULTRA cartridge (porous polar C18, 2.1 mm; Phenomenex) maintained at 30  $^{\circ}\text{C}$  was used for the separation. The mobile phase combination was (A) 0.1% formic acid (Fisher Chemical) in HPLC grade water (Fisher Chemical) and (B) 0.1% formic acid in HPLC grade acetonitrile (Fisher Chemical). The eluent gradient was as follows: 0-3 min hold at 5% B, 3-14 min linear gradient to 95% B, 14-16 min hold at 95% B, 16-22 min linear gradient back to 5% B with a flow rate of 300  $\mu\text{L min}^{-1}$ . UV-vis absorption spectra were acquired using the diode array detector (DAD) over the full 190-680 nm wavelength range. Exiting the DAD, the samples were introduced into the mass spectrometer using a heated electrospray source (HESI; ThermoScientific). Source conditions were as follows: capillary voltage, 3.50 kV; capillary temperature, 325  $^{\circ}\text{C}$ ; sheath gas flow rate, 50; auxiliary gas flow rate, 10; sweep gas flow rate, 1; S-lens RF level 50; auxiliary gas heater temp, 300  $^{\circ}\text{C}$ .

The analysis was done in ESI(+) ion mode using a full scan data-dependent MS/MS (FS-ddMS2) technique. In this approach, full MS scans were recorded over the  $m/z$  50-750 mass range with a resolution of 140,000 and an automatic gain control (AGC) target of  $10^6$  (max. injection time (IT) = 100 ms) while MS/MS scans were recorded for the top 3 most abundant ions from the adjacent full MS scan (resolution, 17,500; AGC target,  $5 \times 10^4$ ; max. IT, 50 ms) using normalized collision energies (NCE) of 10, 30 and 50. The resulting MS/MS spectra are the sum of all the fragment ions collected at all 3 collision energies.

The mass spectrometer was calibrated weekly for mass accuracy using the ThermoScientific Pierce LTQ Velos ESI positive calibration mixture containing butylamine, caffeine, MRFA and Ultramark-1621. The data were acquired using Xcalibur 4.2 software (ThermoScientific) and processed with Freestyle v1.6.

### **3.2.5. Preparation and analysis of thin films**

Thin films were also prepared for comparison to the KBr pellets. Solutions of the NN were prepared in acetonitrile (ACN, Fisher, HPLC grade) and interrogated by ATR-FTIR. For these, ATR Ge crystals (Pike technologies, 45°, 80 mm × 10 mm × 4 mm, 10 internal reflections) were prepared by rinsing with water and ACN, followed by argon plasma cleaning for 10 minutes. ATR samples were prepared by pipetting 10  $\mu$ L of NN solutions onto the crystals where the solvent evaporated immediately leaving behind a thin film. These ATR samples were photolyzed and analyzed by ATR-FTIR as described in earlier studies.<sup>70,71,76</sup> For analysis using DART-MS, solutions were applied to a mesh screen (stainless steel, 74 Mesh 0.094 mm diameter), and the solvent evaporated immediately. The NN on the mesh screen was exposed to the UV lamps and subsequently introduced into the DART source for product analysis.

### **3.2.6. Calculation of absolute number of molecules**

A calibration curve was generated by depositing known volumes of NN calibration solutions in acetonitrile (which gives the absolute number of molecules) onto the ATR crystal and recording the NN ATR-FTIR spectra absorbance immediately after the deposit dried into a thin film. The thin film thickness was calculated to be significantly less than the depth of penetration ( $d_p$ ) as described in chapter 2.4. ATR-FTIR absorbances were converted from

mM to molecules  $\text{cm}^{-2}$  using the coated surface area of the ATR crystal ( $\sim 4 \text{ cm}^2$ ). A calibration curve was generated based on the absorbance and known number of molecules  $\text{cm}^{-2}$ .

### **3.3 Infrared spectra analysis of the pure NNs versus commercial formulation**

DNF and NPM samples were analyzed either in fused solids (KBr pellets) or as thin films (on an ATR crystal). In KBr pellets, the NNs were analyzed in their pure form and in commercial formulations. Infrared spectra were compared in the different forms (**Fig. 3.4**) and no major differences in their IR absorption spectra were observed. The NN fingerprints were readily apparent even in the complex commercial formulation, which is only 20% DNF in Safari or 10% NPM in Capstar. For DNF in KBr, two peaks due to N-H stretches are seen in the  $3000 - 3500 \text{ cm}^{-1}$  region, while one broad peak is seen in the thin film spectrum. This may be due to the molecules being disordered/non-crystalline in the film, while crystalline in the KBr matrix.



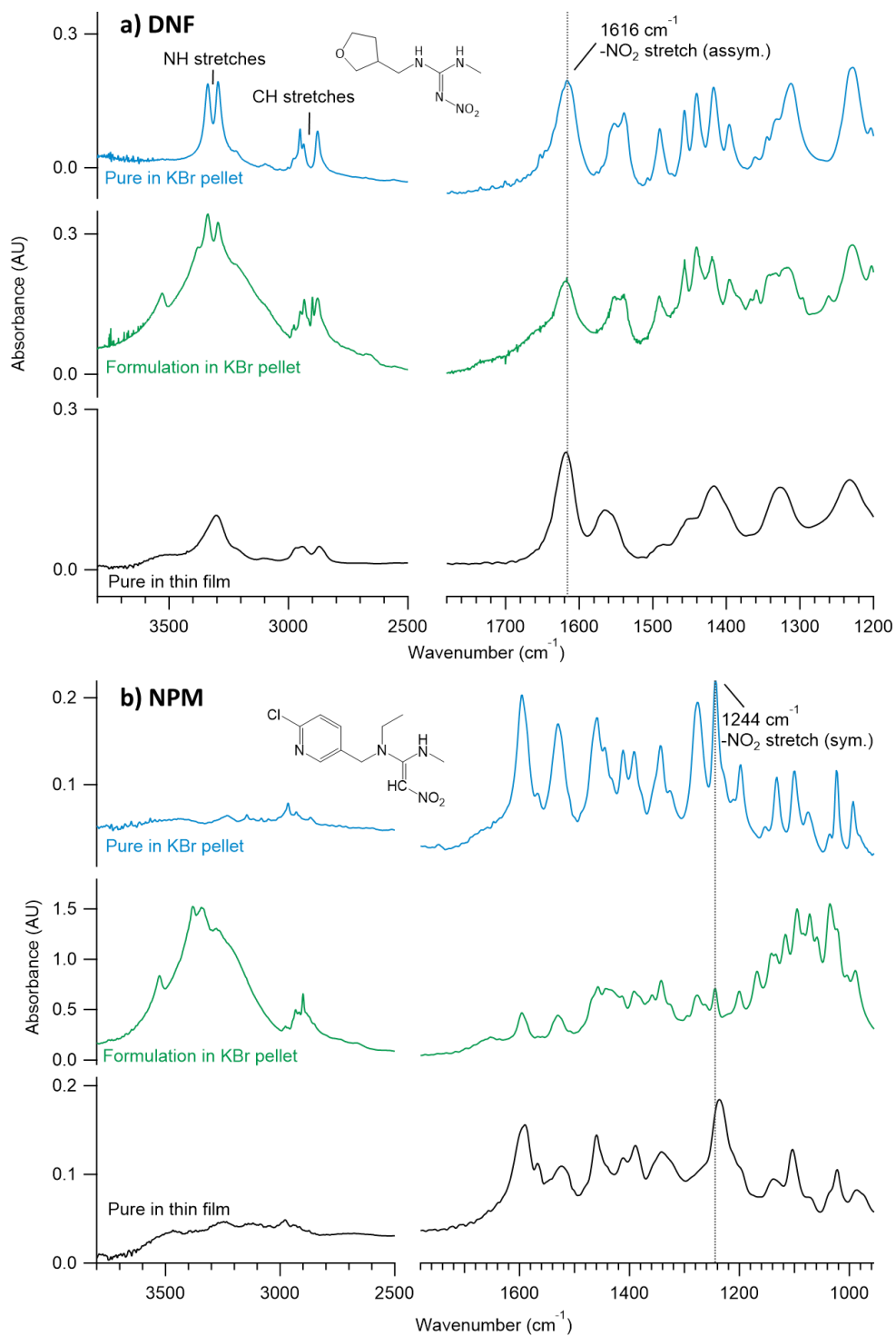


Figure 3.4 FTIR spectra of DNF and NPM in three solid forms. (a) DNF: (blue) pure DNF in a KBr pellet by transmission ( $3.9 \times 10^{14}$  molecules/ $\text{cm}^2$  DNF), (green) commercial formulation Safari in a KBr pellet by transmission ( $3.6 \times 10^{14}$  molecules/ $\text{cm}^2$  DNF), and (black) pure DNF in a thin film by ATR ( $3.1 \times 10^{14}$  molecules/ $\text{cm}^2$  DNF); and (b) NPM: (blue) pure NPM in a KBr pellet by transmission ( $1.8 \times 10^{15}$  molecules/ $\text{cm}^2$  NPM), (green) commercial formulation Capstar™ in a KBr pellet by transmission ( $2.3 \times 10^{15}$  molecules/ $\text{cm}^2$  NPM), and (black) pure NPM in a thin film by ATR ( $1.3 \times 10^{15}$  molecules/ $\text{cm}^2$  NPM).

The two distinct N-H stretches in the DNF KBr matrix spectrum reflect two different ways of H-bonding for each of the two N-H groups in the crystal structure. Le Questel et al.<sup>80</sup> reports that DNF has a dimer crystal structure with a pair of hydrogen bonds between the N-H group of one molecule and the ring-oxygen in the neighboring DNF, as well as intramolecular hydrogen bonds between an N-H group and one of the oxygen atoms of the NO<sub>2</sub> group (discussed in detail below in Section 3.6, **Fig. 3.12**). In the thin film, these N-H stretches overlap, suggesting a disordered film with a variety of H-bonding rather than having two distinct H-bonding possibilities as for the crystal form of the dimers. The thin films were created by evaporation from a solvent over a period of seconds, and the quick drying time may impede crystal formation.

### 3.4 Major NPM photolysis products

**Fig. 3.5** shows typical DART-MS spectra before and after irradiation for pure NPM in a KBr pellet, the commercial formulation Capstar™ in a KBr pellet, and a thin film of pure NPM on a mesh screen. Black traces are taken before photolysis and colored traces are after 3 hours of irradiation using a 350 nm broadband lamp. Similar results were observed using the 254 nm and 305 nm lamps. Spectra from samples before photolysis are consistent with NPM thin films reported by Aregahegn et al.,<sup>76</sup> showing a parent peak at  $m/z$  271 corresponding to [NPM + H]<sup>+</sup>, as well as two peaks at  $m/z$  212 and 240, corresponding to the protonated forms of the compounds shown in **Fig. 3.5**:

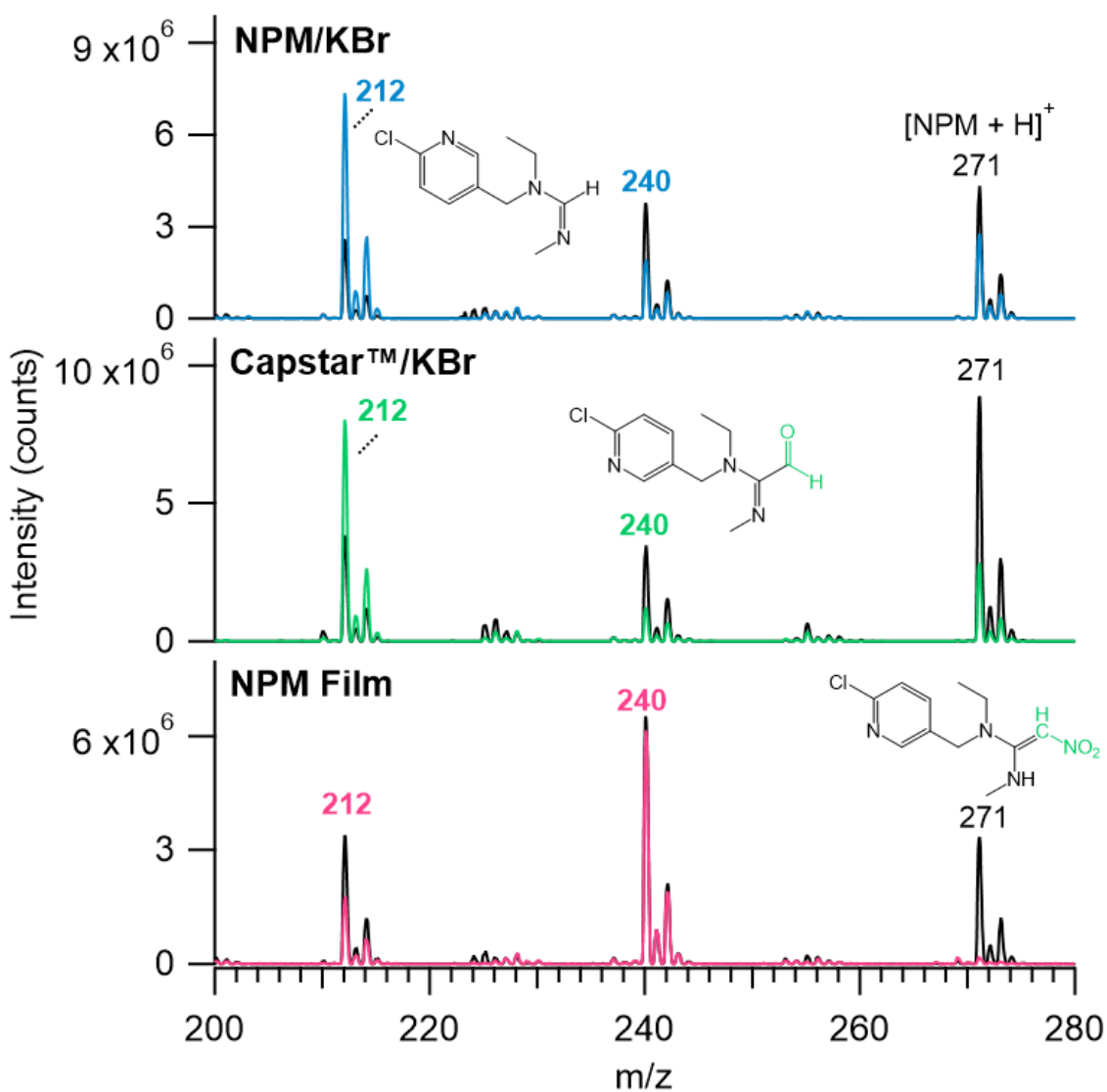


Figure 3.5 DART-MS of NPM before (black traces) and after (color traces) photolysis at 350 nm for 3 hours in three solid forms.

After photolysis, less contribution from NPM at  $m/z$  271 is observed, and the peak at  $m/z$  212 becomes dominant. The species responsible for this peak has also been previously reported in drinking water<sup>81</sup> and thin films.<sup>76</sup> The peak observed at  $m/z$  240 was also present in all solid forms both before and after irradiation. The relative contribution from  $m/z$  240

was higher in thin film samples both before and after photolysis, and may be due to its formation in the DART source itself.<sup>76</sup>

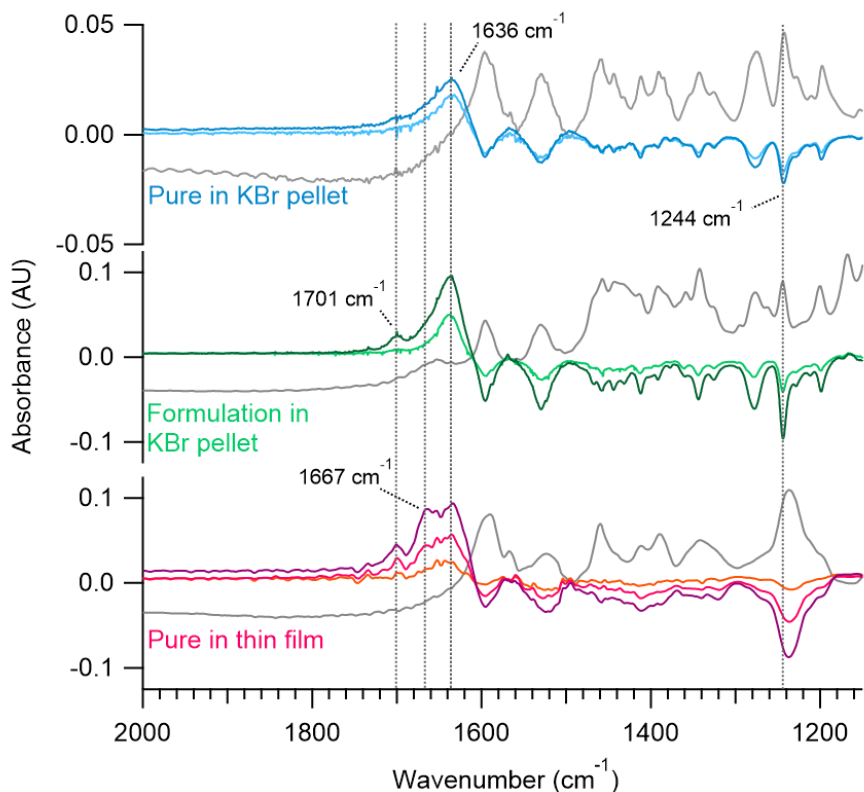


Figure 3.6 FTIR spectra for NPM irradiated at 305 nm in three solid forms: (**blues**) pure NPM in a KBr pellet ( $5.1 \times 10^{14}$  molecules/cm<sup>2</sup> NPM at 35% and 50% loss), (**greens**) commercial formulation Capstar™ in a KBr pellet ( $3.2 \times 10^{15}$  molecules/cm<sup>2</sup> NPM, 20% and 48% loss), and (**pinks**) pure NPM in a thin film ( $1.4 \times 10^{15}$  molecules/cm<sup>2</sup> NPM at 16%, 50% and 92% loss). Gray traces show initial absorbance spectra before photolysis. The initial absorbance spectrum of the commercial formulation has been multiplied by a factor of 0.1.

Evidence for both of these products is also found in the IR difference spectra of photolyzed NPM (**Fig. 3.6**), where positive peaks indicate formation of products and negative peaks indicate loss of NPM. In all three solid forms, a major positive product peak is observed at 1636 cm<sup>-1</sup>, a region characteristic of C=N bonds.<sup>82</sup> In thin films, a second product peak is also distinguishable at 1667 cm<sup>-1</sup>, and although not prominent in the pure and formulated NPM embedded in KBr, it is likely contributing to the broad 1636 cm<sup>-1</sup> peak

shape. Aregahegn et al.<sup>76</sup> attributed the 1667 cm<sup>-1</sup> peak to the C=N stretch of the *m/z* 212 species and a 1634 cm<sup>-1</sup> peak to the C=N stretch of the *m/z* 240 species, red-shifted due to conjugation with the C=O group. A small peak for the C=O stretch is also visible at 1701 cm<sup>-1</sup>.

The apparent smaller contribution of the *m/z* 212 species in the IR difference spectra compared to the DART-MS may be due to differences in absorptivity. Although reference standards of NPM degradation products were not available, those for products from the NN imidacloprid (IMD) which contain C=O and C=N bonds show that the C=O containing species has a higher infrared absorptivity at equimolar concentrations (available in the SI of Rohrbacher et al. 2021).<sup>83</sup> Similarly, DART-MS spectra are influenced by variable ionization efficiency across compounds, gas reagent temperature, vapor pressure of the species, and heterogeneity of the pellet. Thus, neither DART-MS nor FTIR relative intensities should be assumed to reflect their relative contributions. The combination of MS and FTIR data, however, suggest that both species are present as photolysis products in pure and commercial formulations.

### 3.5 Major DNF photolysis products: desnitro and urea pathways

**Fig. 3.7** shows typical DART-MS spectra for DNF in the three forms before photolysis and after 15 hours of irradiation using a 305 nm broadband lamp. Before photolysis (black traces), DNF (MW 202) shows a parent peak at *m/z* 203 corresponding to [DNF + H]<sup>+</sup>, as well as a dimer ion at *m/z* 405 corresponding to [2DNF + H]<sup>+</sup> (data not shown). MS/MS analysis of *m/z* 203 showed fragments at *m/z* 157, 129 and 113, consistent with the literature for DNF.<sup>84-88</sup>

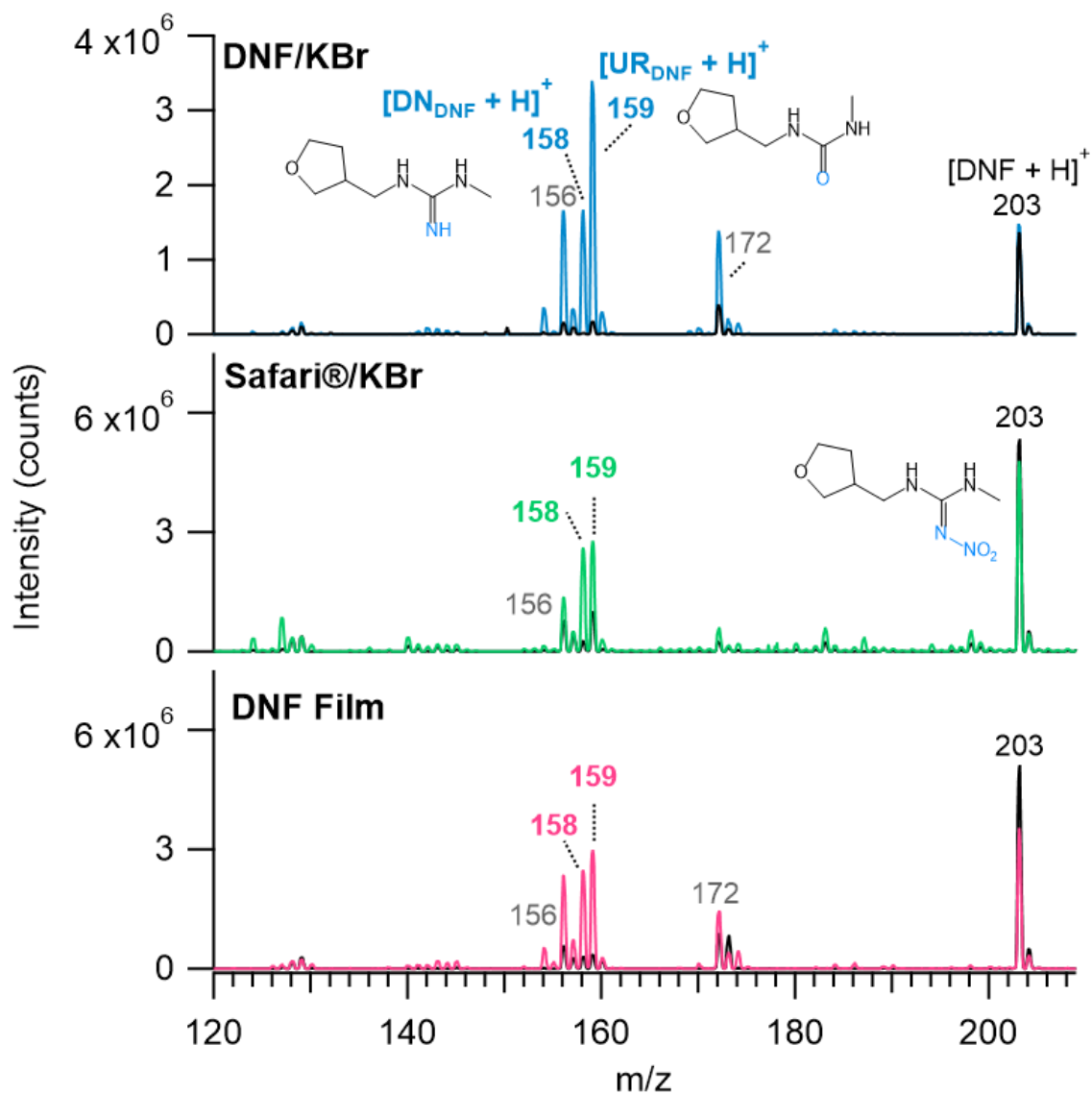


Figure 3.7 DART-MS of DNF before (black traces) and after (color traces) photolysis at 305 nm in three solid forms.

After photolysis (Fig. 3.7, colored traces), product peaks corresponding to urea (UR<sub>DNF</sub>) and desnitro (DN<sub>DNF</sub>) derivatives appear, which are commonly observed for samples containing DNF and its metabolites.<sup>84,86,87,89</sup> UR<sub>DNF</sub> (MW 158) is seen at  $m/z$  159 corresponding to [UR<sub>DNF</sub> + H]<sup>+</sup>, as well as  $m/z$  317 and  $m/z$  361 (data not shown) corresponding to [2UR<sub>DNF</sub> + H]<sup>+</sup>, and [UR<sub>DNF</sub> + DNF + H]<sup>+</sup> respectively. The peak at  $m/z$  158

corresponds to  $[\text{DN}_{\text{DNF}} + \text{H}]^+$  for the desnitro derivative  $\text{DN}_{\text{DNF}}$  (MW 157). MS/MS spectra are available in the SI of Rohrbacher et al. 2021.<sup>83</sup> Peaks were also observed at  $m/z$  156 and  $m/z$  172 before and after photolysis. These peaks were further explored using UPLC-DAD-HRMS which identified them as  $[\text{C}_7\text{H}_{14}\text{ON}_3]^+$ , attributed to  $[\text{DNF} - \text{NO}_2]^+$ , and  $[\text{C}_7\text{H}_{14}\text{O}_2\text{N}_3]^+$ , attributed to  $[\text{DNF} - \text{NO}]^+$ .<sup>83</sup> The species' retention time and peak shape was identical to that of the parent  $m/z$  203 species and are thus believed to be due to in-source fragmentation, in agreement with their presence in the pre-photolysis DART-MS spectra. Therefore, for DNF in all matrices,  $\text{DN}_{\text{DNF}}$  and  $\text{UR}_{\text{DNF}}$  are the major solid photolysis products and their proposed formation mechanism is shown in **Fig. 3.8**.

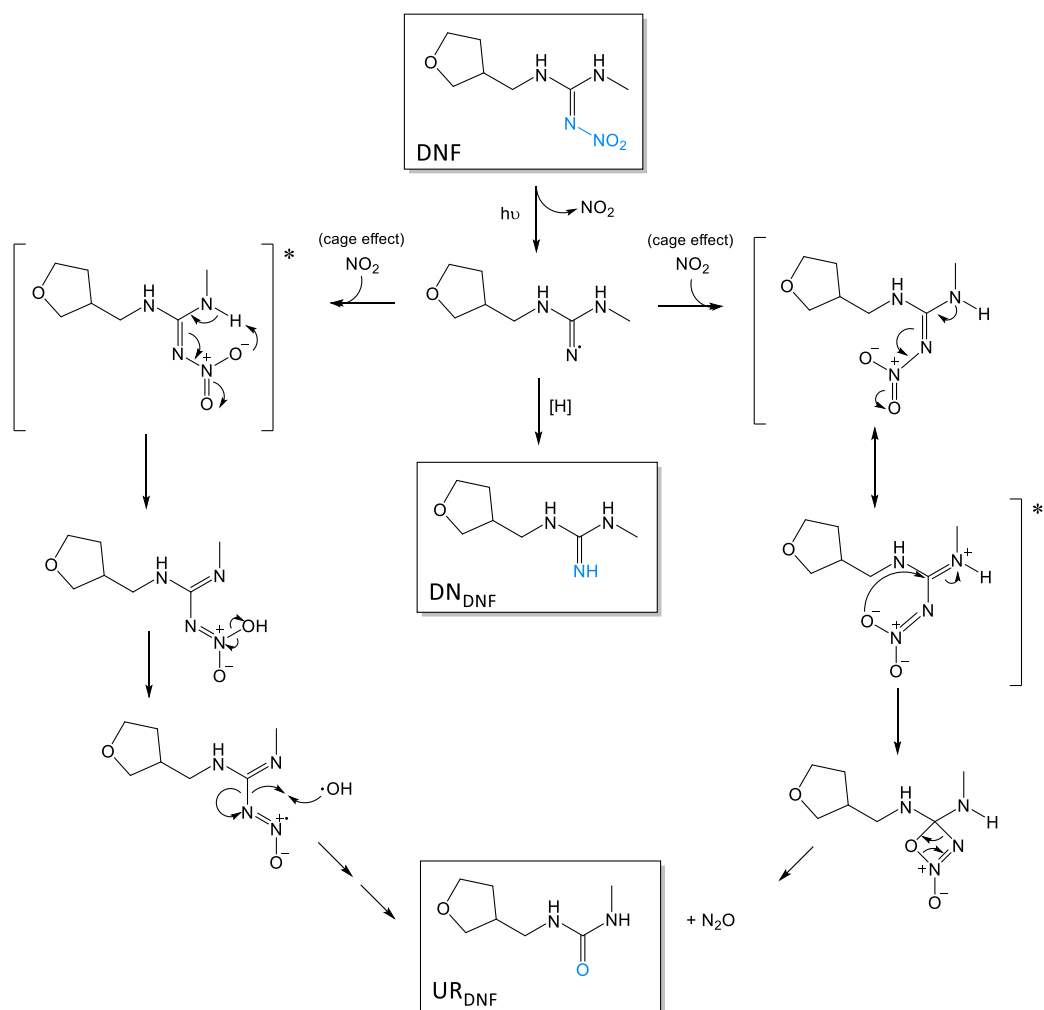


Figure 3.8 Proposed DNF degradation mechanism, based on Wang et al. 2019<sup>46</sup> and Aregahegn et al. 2016.<sup>47</sup>

The IR difference spectra of photolyzed DNF (**Fig. 3.9**) show a product peak near  $1665\text{ cm}^{-1}$ . The broad peak shape again likely indicates overlapping contributions from the C=O and C=N stretch signals of the urea and desnitro products.



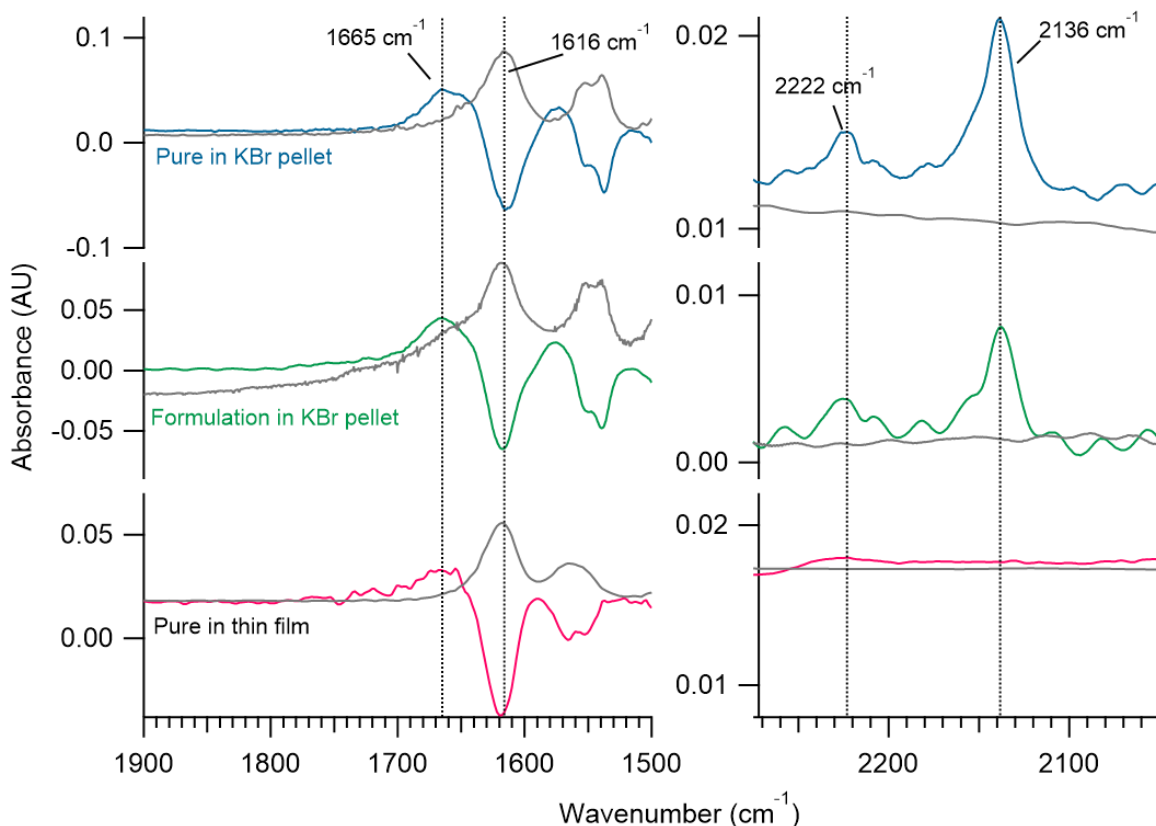


Figure 3.9 Solid-phase difference spectra of DNF irradiated at 305 nm in three matrices: (**blue**) pure DNF in a KBr pellet by transmission ( $3.9 \times 10^{14}$  molecules/cm<sup>2</sup> DNF, 43 % loss), and (**green**) commercial formulation Safari® in a KBr pellet by transmission ( $3.6 \times 10^{14}$  molecules/cm<sup>2</sup> DNF, 31% loss), and (**pink**) pure DNF in a thin film by ATR ( $3.1 \times 10^{14}$  molecules/cm<sup>2</sup> DNF, 36% loss). Gray traces show initial absorbance spectra before photolysis for reference, and these spectra in the 1900-1500 region cm<sup>-1</sup> are not to scale.

The formation of the urea and desnitro derivatives is of great importance for two reasons. First, both are still expected to exhibit insect toxicity. Second, while the urea derivative has low toxicity to mammals, the desnitro derivative may show a large increase in mammalian toxicity. For example, Chao and Casida<sup>42</sup> reported that for IMD degradation products, DN<sub>IMD</sub> has an oral LD<sub>50</sub> of 7-24 mg/kg in rats, an increase from the 424 mg/kg of the parent IMD, and is more toxic than nicotine, which has an oral LD<sub>50</sub> of 50 mg/kg. These photolysis products are expected to remain on surfaces, where they can be a risk for both pollinators due to their insect toxicity, as well as to consumers of treated foods due to the

increased mammalian toxicity of the desnitro derivative. There are no direct mammalian toxicity measurements of UR<sub>DNF</sub> and DN<sub>DNF</sub> which would be important for a full evaluation of their environmental impacts.

### 3.6 “Solid phase” products unique to DNF

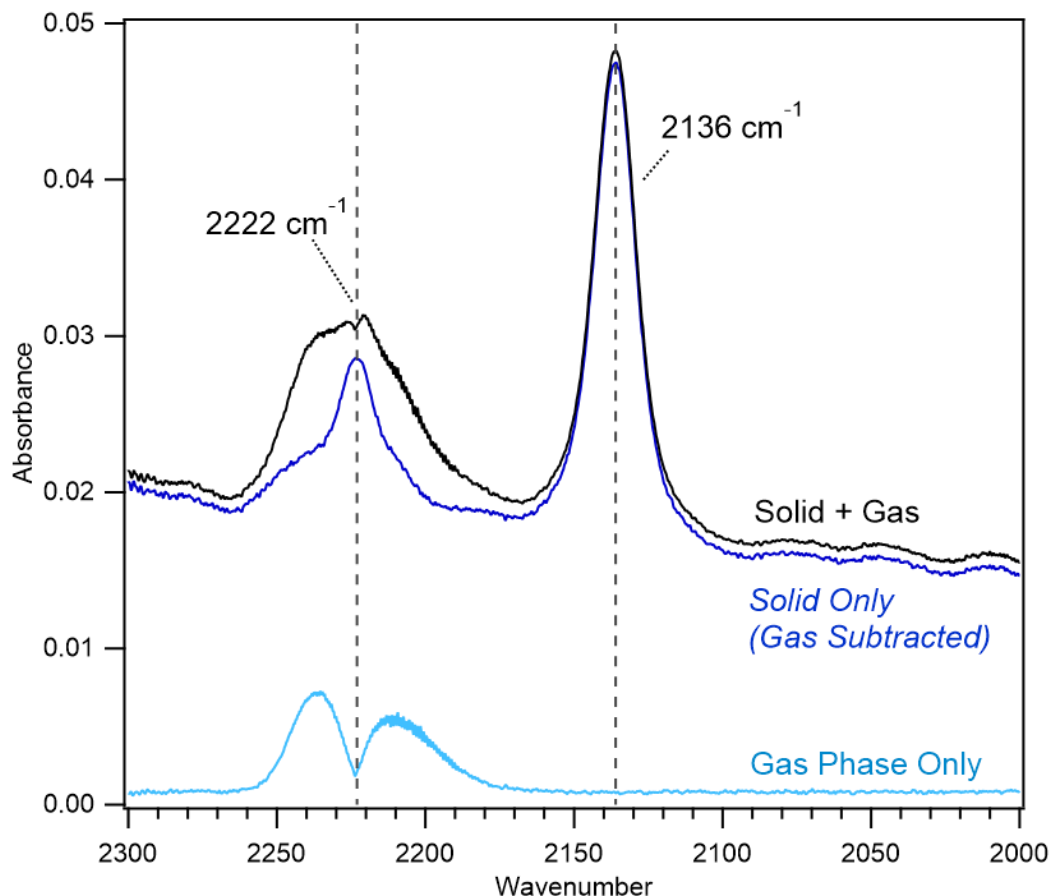


Figure 3.10 FTIR spectra comparing solid and gas phase products of 0.5% DNF/KBr photolyzed at 254 nm to 59% loss DNF.

DNF difference spectra (**Fig. 3.9**) also show new solid-phase product peaks at 2222 and 2136 cm<sup>-1</sup>, a region characteristic of  $\nu(\text{NO})$  stretches.<sup>90</sup> These products were observed in both pure and formulated DNF samples in the KBr matrix, indicating again that the presence of the additional ingredients in the formulations did not affect the product

distribution. These peaks, however, were not strongly seen in irradiated thin films of DNF, suggesting that the dense solid KBr pellets do affect the photodegradation.

The 2222  $\text{cm}^{-1}$  solid-phase peak overlapped with product peaks observed in the gas phase. **Fig. 3.10** shows a broad peak around 2222  $\text{cm}^{-1}$  is observed with the sample rod in the down position, probing both the solid and gas phase simultaneously. When the rod was raised to probe the gas phase only,  $\text{N}_2\text{O}$ , with its distinct *P* and *R* branches,<sup>91</sup> was clearly evident. In earlier studies,  $\text{N}_2\text{O}$  was hypothesized to be formed from cleavage of the N- $\text{NO}_2$  bond in nitroguanidines (such as DNF) and the C- $\text{NO}_2$  bond in NPM, followed by intramolecular rearrangements in the solids.<sup>70,71,76</sup> Subtraction of the gas phase from the combined gas and solid spectrum reveals a broad peak in the solid centered at 2222  $\text{cm}^{-1}$ . This product in the solid-phase was observed also for a number of NNs (**Fig. 3.11**), all of which form  $\text{N}_2\text{O}$  in the gas phase when irradiated as thin films.<sup>71</sup> Dows<sup>92</sup> and Yamada and Person<sup>93</sup> showed that condensed  $\text{N}_2\text{O}$  at 80 K has a single peak in this region, with some variation in peak shape, and Hisatsune<sup>94</sup> showed a temperature dependence for this peak's location and shape. Thus, we assign the 2222  $\text{cm}^{-1}$  peak seen in the solid-only spectrum to  $\text{N}_2\text{O}$  that is trapped in the KBr pellet solid.

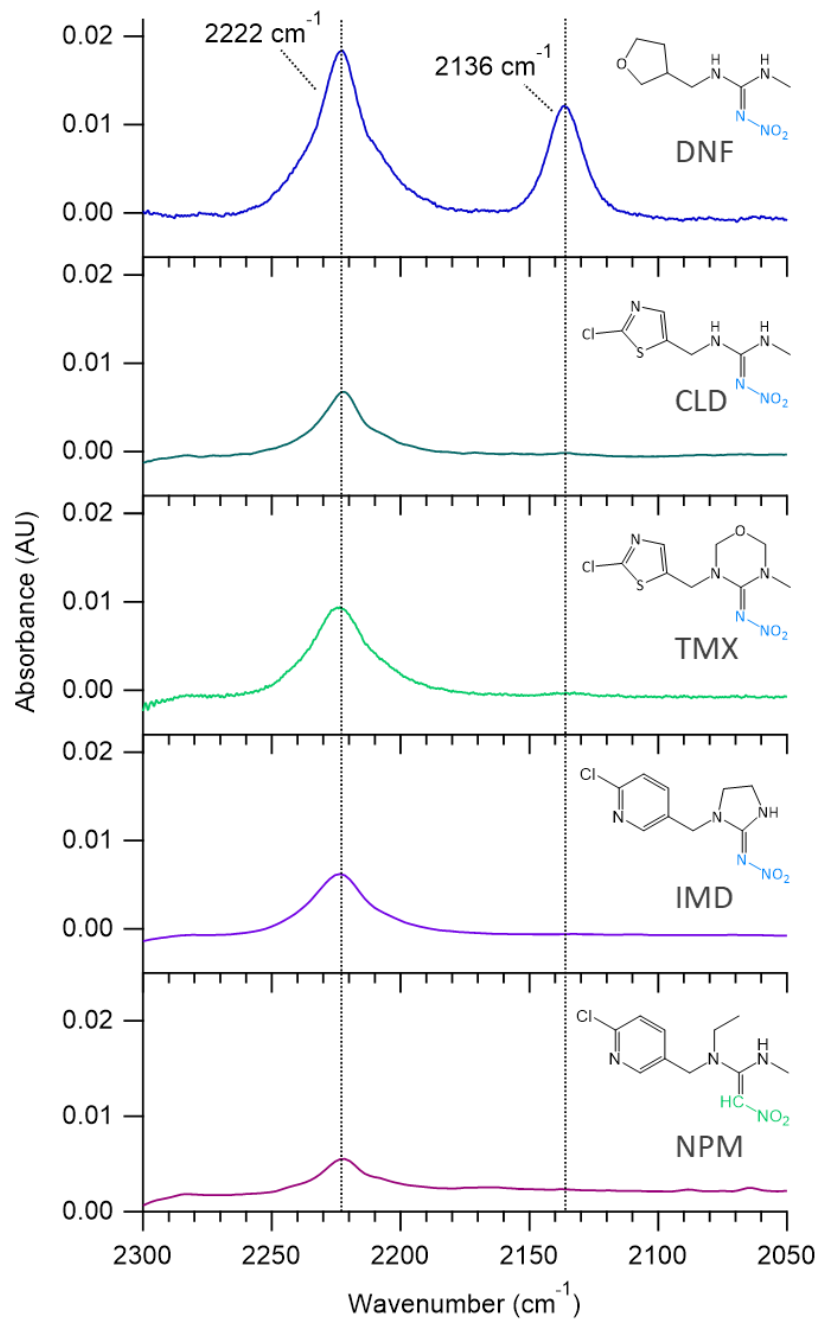


Figure 3.11 Comparison of solid phase product formation in KBr pellets at w/w concentrations of 0.49% DNF/KBr, 1.04% CLD/KBr, 0.94% TMX/KBr, and 0.94% IMD/KBr, and 0.67% NPM/KBr. Nitroguanidines were irradiated at 254 nm for ~30 min, and NPM for 10 hours.

This peak was not seen when irradiating DNF in a solid pellet made of Cabosil®, which is an ultrafine silica oxide powder, but N<sub>2</sub>O was observed in the gas phase, suggesting the

N<sub>2</sub>O was not efficiently trapped in the Cabosil<sup>®</sup> environment. The reason for the difference between Cabosil<sup>®</sup> and KBr matrix is not clear but may be due to the strongly ionic environment in KBr or to differences in the particle size and packing that can influence the trapping.

DNF in a KBr pellet also showed a product peak at 2136 cm<sup>-1</sup> (**Fig. 3.9, 3.11**). Bands in this region have often been identified as being due to the nitrosonium ion (NO<sup>+</sup>)<sup>95-103</sup> in studies of the interaction of NO<sub>x</sub> with zeolites (although adsorbed NO<sub>2</sub> has also been suggested).<sup>104</sup> This peak was also not seen in the Cabosil<sup>®</sup> matrix, suggesting that NO<sup>+</sup> is stabilized by the ionic KBr environment.

If the NO<sub>2</sub> generated upon bond cleavage is free to migrate in the matrix, it could react with the KBr to form NO<sup>+</sup>. To test this, a KBr pellet (with no NN present) was exposed to 293 ppm NO<sub>2</sub> in both static and flow modes, with and without photolysis, but a peak at 2136 cm<sup>-1</sup> was not observed. As expected, gas phase NO<sub>2</sub> peaks (1617 and 2906 cm<sup>-1</sup>), a BrNO peak (~1800 cm<sup>-1</sup>), and a solid NO<sub>3</sub><sup>-</sup> (1358 cm<sup>-1</sup>) peak were observed, consistent with earlier studies of the reaction of NO<sub>2</sub> with NaBr.<sup>105</sup> None of these were observed in the DNF/KBr photolysis experiments. This suggests that when NO<sub>2</sub> is formed in the DNF photolysis, it undergoes the recombination and intramolecular rearrangements shown in **Fig. 3.8** rather than reacting with KBr. This is reasonable since the DNF exists as agglomerates of the NN within the KBr matrix (**Fig. 3.1**), rather than as individually distributed molecules.

The 2136 cm<sup>-1</sup> peak was only seen in the solid phase spectra and was only weakly present, if at all, in the other NNs in KBr pellets (**Fig. 3.11**). In thin films of DNF and the structurally similar nitroguanidine clothianidin, CLD, a small peak is seen initially but

disappears within minutes (**Fig. 2.2**), while in the KBr pellet it is detectable for days. A possible explanation is the crystal structure of DNF (**Fig. 3.12**) reported in Le Questel et al.<sup>80</sup> DNF crystallizes into a dimer structure, connected by hydrogen bonds between the ring and one of the secondary amines in the nitroguanidine group.

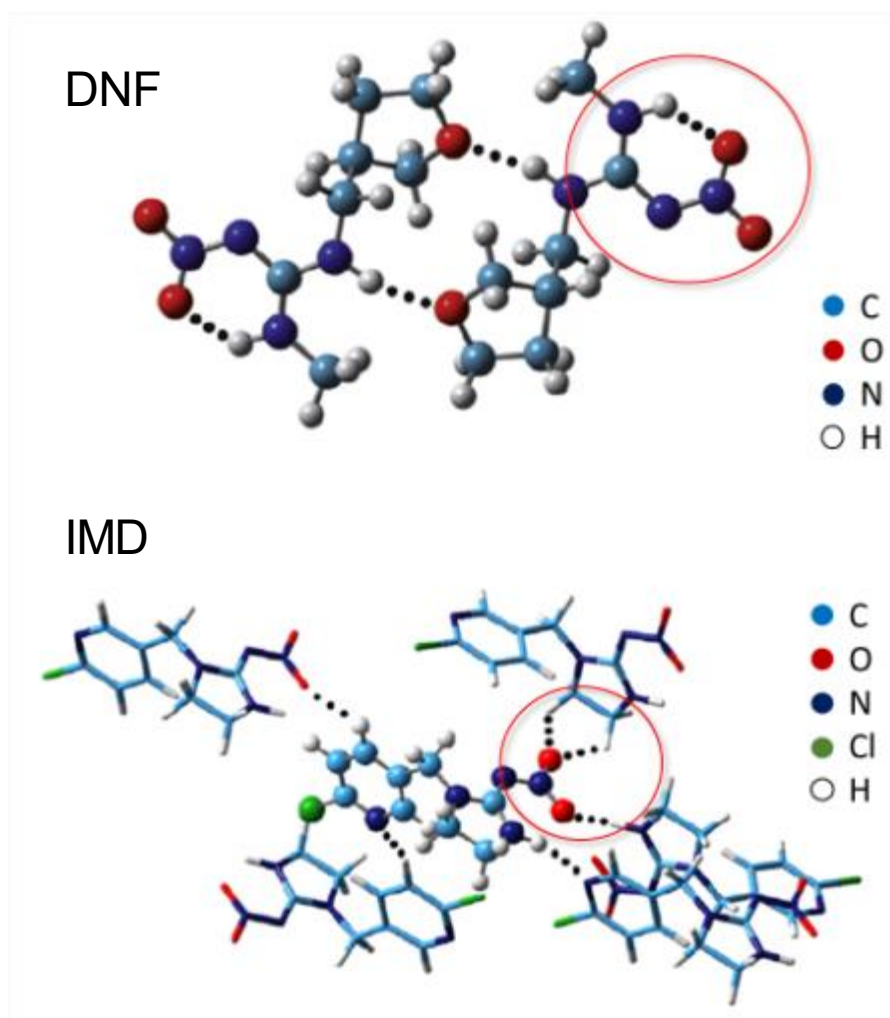


Figure 3.12 Crystal structures of DNF (top) and IMD (bottom) adapted from Le Questel et al.<sup>51</sup> The red circles highlight the differences between DNF and IMD in  $-NO_2$  hydrogen bonding.

Note that only one of the  $-NO_2$  group oxygen atoms is intramolecularly hydrogen bonded, in contrast to IMD, for example. This may assist in isomerization to  $-ONO$ , which is

a known intermediate in the photolysis of nitro-organics,<sup>106,107</sup> and subsequent generation of  $\text{NO}^+$  (**Fig. 3.13**). For example, Bhattacharya et al.<sup>108</sup> in an experimental and theoretical study of the photolysis of dimethylnitramine,  $(\text{CH}_3)_2\text{N}-\text{NO}_2$ , which shares structural features similar to DNF, report that a nitro/nitrite isomerization mechanism is the major channel of decomposition from the excited electronic state for photolysis in a dense gaseous medium. In the IMD crystal structure in **Fig. 3.12**, on the other hand, there are three intermolecular hydrogen bonds with the  $-\text{NO}_2$  group. Thus the  $-\text{NO}_2$  may be too constrained for isomerization to  $-\text{ONO}$ . The other nitroguanidines, with similar ring structure to IMD, may be expected to behave the same way. This further suggests that samples in the fused solid KBr pellet are in their crystalline form, but in a disordered form in the thin films with a variety of hydrogen bonding possibilities.

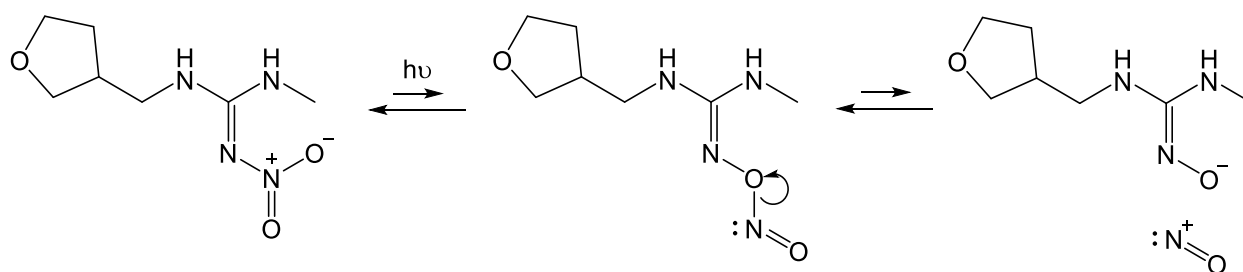


Figure 3.13 Proposed isomerization of  $-\text{NO}_2$  to  $-\text{ONO}$  to produce  $\text{NO}^+$ .

### 3.7 Change in products after photolysis

If the  $2222\text{ cm}^{-1}$  peak is due to  $\text{N}_2\text{O}$  trapped in the solid, it might be expected over time to decrease as the  $\text{N}_2\text{O}$  diffuses to the gas phase. To test this, the DNF/KBr pellet was irradiated with the 254 nm lamp to  $\sim 20\%$  loss of DNF, then the light was turned off, and FTIR spectra were continually recorded to monitor both products in the KBr pellet as well as the gas phase. These experiments were conducted using the 254 nm lamp to give relatively

rapid photodegradation and product formation compared to the longer times over which diffusion is expected to occur. **Fig. 3.14** shows signal intensities in either solid phase or gas phase spectra for reactant and product peaks from before photolysis (time = 0 minutes), during photolysis (first 30 minutes), and for four days after the lamp is shut off (grey area). The corresponding changes in the FTIR spectra are shown in **Fig. 3.15**. The first data point in **Fig. 3.14**, taken before photolysis begins, shows a non-zero value only for the DNF signal. The second data point, obtained after the sample has been irradiated for 30 minutes, shows a decrease in DNF, and positive values for all the products formed.



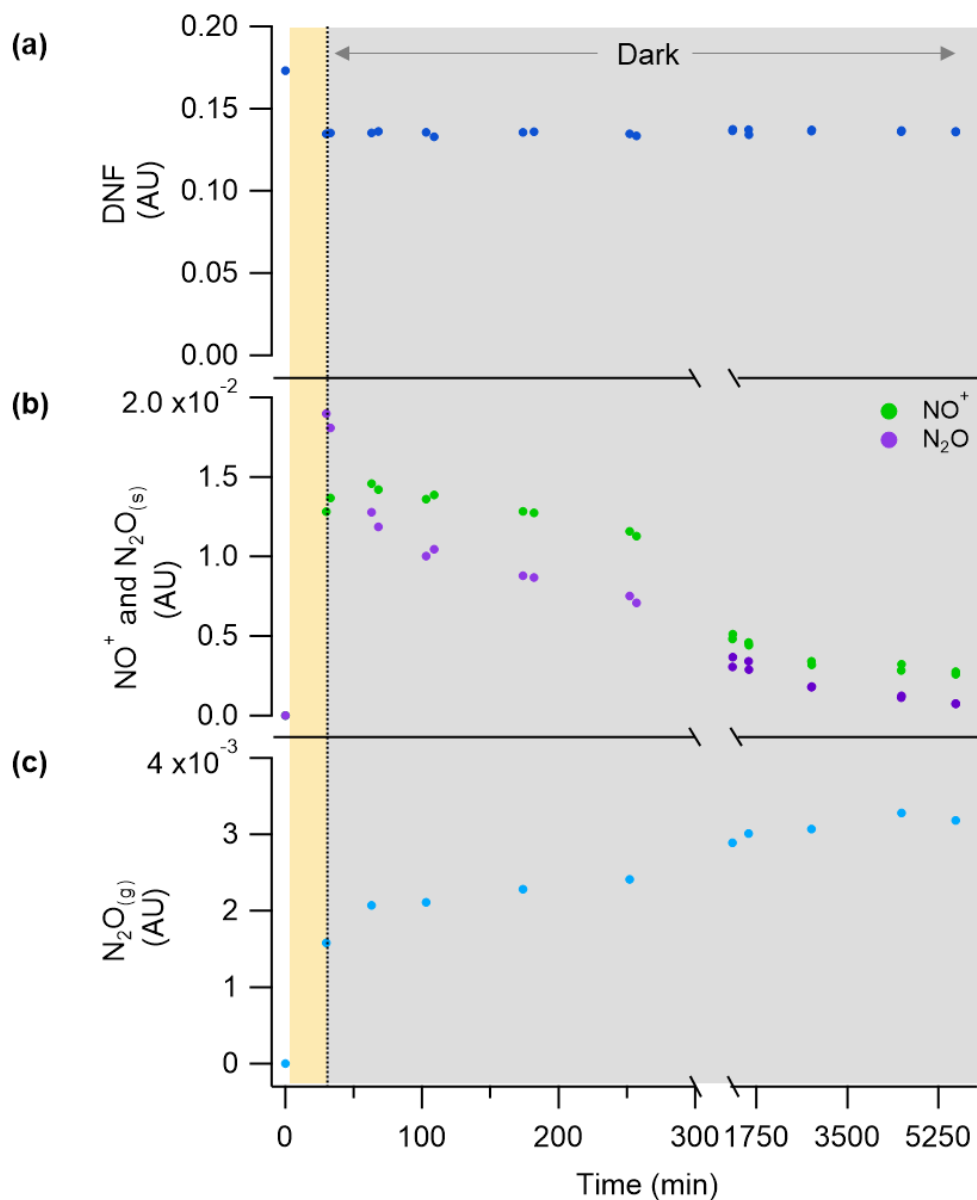


Figure 3.14 0.49% DNF/KBr irradiated at 254 nm to 21% loss DNF (dashed line), and then monitored for 4 days in dark conditions. Frames (a) and (b) are of solid phase only spectra (gas phase has been subtracted) and results in (c) for N<sub>2</sub>O(g) are taken from gas phase only spectra. Y-axis is absorbance peak height for (a) DNF at 1616 cm<sup>-1</sup>, (b) product peak heights for NO<sup>+</sup> (2136 cm<sup>-1</sup>) and N<sub>2</sub>O<sub>(s)</sub> (2222 cm<sup>-1</sup>) products, and (c) N<sub>2</sub>O<sub>(g)</sub> peak measured at 2235 cm<sup>-1</sup> from the gas phase spectra.

The DNF signal is nearly constant over the four-day dark period. The peak at 2222 cm<sup>-1</sup>, assigned to trapped N<sub>2</sub>O, decreased to near zero by the end of the four days. The same was true of the 2136 cm<sup>-1</sup> peak assigned to NO<sup>+</sup>. Simultaneously, gas phase N<sub>2</sub>O increased, as

expected if the  $\text{N}_2\text{O}$  trapped in the solid was diffusing out into the gas phase. No other new peaks, e.g., due to  $\text{NO}$ ,  $\text{NO}_2$ , or  $\text{BrNO}$  were detected in the gas phase, suggesting that recombination to reform the nitrite ( $-\text{ONO}$ ) and DNF may be the major fate of  $\text{NO}^+$  (**Fig. 3.13**). In this case, the relative change of DNF signal may be too small to show a significant signal change over time.

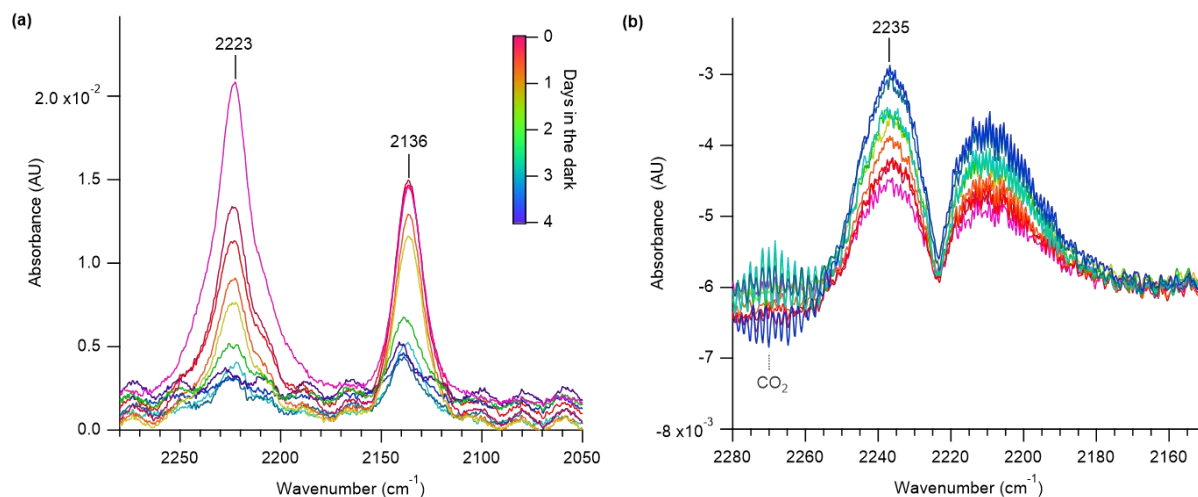


Figure 3.15 0.49% DNF/KBr irradiated with a 254 nm lamp for 30 min (pink trace). The photolysis lamp was shut off and the sample was then monitored for 4 days in dark conditions. Spectra are (a) solid phase only and (b) gas phase only.

The DNF/KBr pellet from the light/dark study was also analyzed using DART-MS after the four-day dark period. There were no new peaks observed after the dark period when compared to the sample analyzed immediately after photolysis. Similar light/dark experiments using the 305 nm lamp, which required a week of photolysis to reach 20% loss of DNF, gave qualitatively similar results but less solid  $\text{N}_2\text{O}$  infrared peaks due to the slower rate of formation relative to diffusive loss to the gas phase. When the lamp was removed to begin the dark period, the solid  $\text{N}_2\text{O}$  peak completely disappeared within one day and the

N<sub>2</sub>O (g) signal increased slightly during this first day corresponding to escape from the solid phase.

### 3.8 6. N<sub>2</sub>O yields

Gas-phase N<sub>2</sub>O yields ( $\Delta$  moles N<sub>2</sub>O/ $\Delta$  moles NN) were calculated for the KBr pellet experiments after the solid phase peak at 2222 cm<sup>-1</sup> had disappeared and the gas phase N<sub>2</sub>O signal had stabilized. KBr pellet experiments showed a yield of  $0.51 \pm 0.10$  for both pure DNF and the commercial formulation Safari®. **Table 3.1** shows these values are in agreement with previously reported values for pure solid deposits on windows using transmission mode, but lower than when ATR was used on thin films.<sup>71</sup> This suggests the branching ratio that leads to N<sub>2</sub>O is altered in the KBr pellets and the window deposits compared to the thin ATR films.

The major source of tropospheric N<sub>2</sub>O is known to be nitrification and denitrification in soils and aquatic systems. Nitrous oxide soil emissions are characterized by very high spatio-temporal variability resulting in “hot spots” and “hot moments,”<sup>109</sup> which are believed to be driven mainly by abiotic inputs such as fertilizers.<sup>110-112</sup> While N<sub>2</sub>O from photolysis of the NNs will be a minor contributor to the overall global burden,<sup>70,71</sup> it could contribute to these hot spots.

Table 3.1 Nitrous oxide yields ( $\Delta$ [N<sub>2</sub>O]/ $\Delta$ [NN]) from photolysis of dinotefuran in different matrices

Matrix	Method	N <sub>2</sub> O Yield <sup>a</sup>
Pure in KBr pellet	Transmission	$0.51 \pm 0.10$
Formulation in KBr pellet	Transmission	$0.51 \pm 0.10$
Pure NN deposits on window <sup>71</sup>	Transmission	$0.57 \pm 0.38$
Pure in thin film <sup>71</sup>	ATR	$0.94 \pm 0.40$

<sup>a</sup>Errors are 2 $\sigma$ , calculated as  $\sigma = \left(\frac{\sum(x_i - \mu)^2}{N}\right)^{1/2}$

### 3.9 Quantum yield calculations for loss of NN during photolysis

Loss of DNF and NPM was followed using the 1616 and 1244  $\text{cm}^{-1}$  peaks (assigned to the asymmetric and symmetric  $-\text{NO}_2$  stretches, respectively).<sup>71,82</sup> The decays followed first-order kinetics. Photolysis quantum yields ( $\phi$ ) for loss of either DNF or NPM were calculated using **equation 3.1**,<sup>68</sup>

$$k_p = \phi \sum \sigma(\lambda) \cdot I_{rel}(\lambda) \cdot CF \quad (3.1)$$

where  $\phi$  is the quantum yield which is molecules decomposed per photon absorbed,  $\sigma$  is the absorption cross section in  $\text{cm}^2 \text{molecule}^{-1}$  (discussed in chapter 2.3),  $I$  is the photon spectral flux density of the photolysis lamp in photons  $\text{cm}^{-2} \text{s}^{-1} \text{nm}^{-1}$  (as a function of wavelength, measured using an Ocean Optics UV-Vis spectrometer), and the correction factor,  $CF$ , converts relative to absolute lamp intensities as described in the SI of Rohrbacher et al. 2021.<sup>83</sup> The photon spectral flux density was measured using 2-nitrobenzaldehyde (2NB) as an actinometer with a well-established photolysis quantum yield of 0.5 in a solid.<sup>113-116</sup>

An interesting pattern was observed in the photodegradation rate constants from 254 nm irradiation (**Fig. 3.16**),<sup>83</sup> where higher concentrations of NN in the KBr pellets resulted in lower photolysis rate constants. Since the SEM-EDS images showed the NN present as agglomerates spread throughout the pellet, this suggests that at higher concentrations these agglomerates may be scattering light and physically shielding NN molecules located deeper in the pellet. The latter suggests that the KBr pellets are not optically thin, and as discussed in chapter 2.4, a calculation of the transmittance can reveal insight into the optical density. In the case of KBr pellets, we have changed from a  $d_p$  of  $\sim 0.4 \mu\text{m}$  to agglomerates of NN that are  $\sim 10 \mu\text{m}$  (**Fig. 3.1**) for an increase by a factor of 40. The resultant transmittance is

therefore  $I/I_0 = 10\exp[-(2 \times 10^{-18})(1 \times 10^{16})(40)] = 0.01$ . Since **equation 3.1** is appropriate only within the optically thin limit, these quantum yields were used only for comparison of the pure NN to the formulated NN, and not used for atmospheric lifetime calculations. Furthermore, only lower concentration photolysis rate data were used as they were considered to be more accurate for quantum yield calculations.

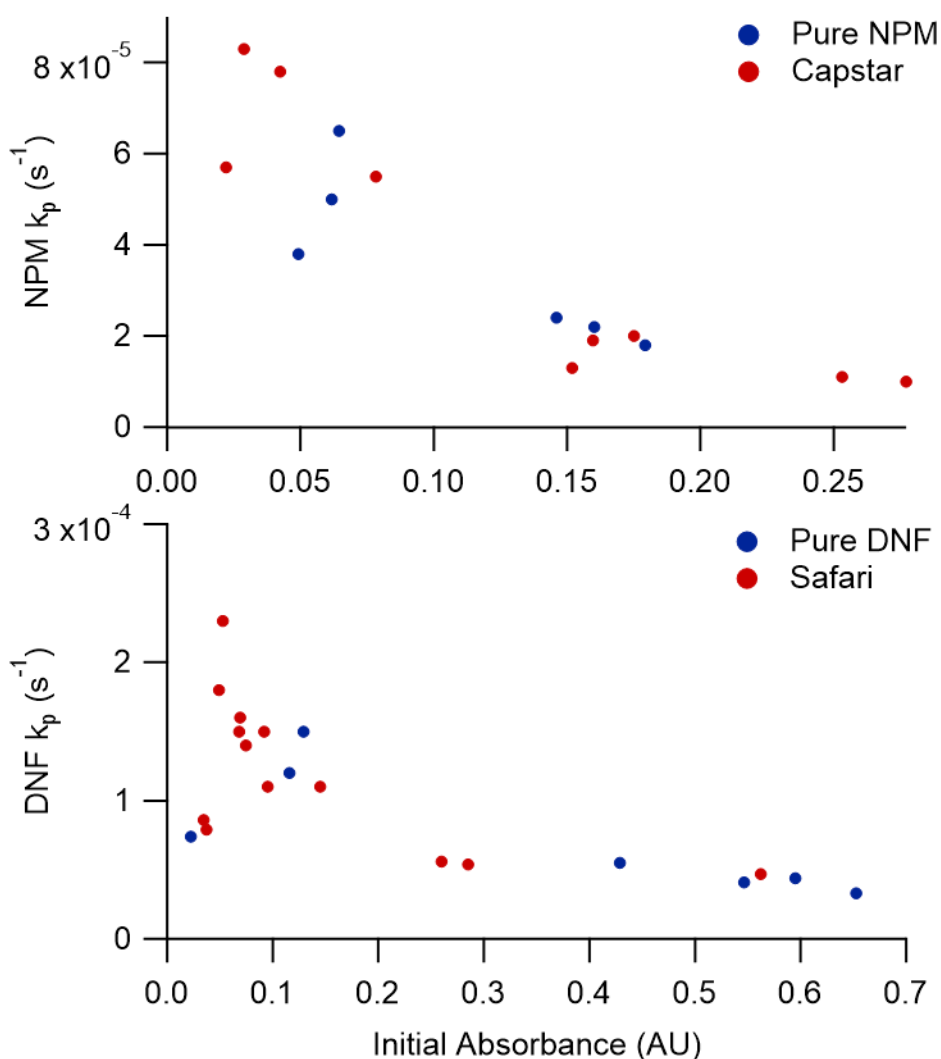


Figure 3.16 Photolysis rate constants ( $k_p$ ) at varying initial absorbances (proportional to concentration) recorded for NPM and Capstar (top) and DNF and Safari (bottom).

Photolysis rate constants ( $k_p$ ) for the NN were obtained from their first-order plots. The quantum yields relevant to the actinic region for both DNF and NPM measured using the 305 nm and 350 nm broadband lamps are reported in **Table 3.2** and **Fig. 3.17**. Quantum yields at 254 nm and in previous work<sup>71,76</sup> probing thin films of pure NNs are also provided for comparison.

Table 3.2 Comparison of quantum yields in three matrices

Neonicotinoid	Formulation	Lamp (nm)	$\phi$ ( $\times 10^{-3}$ ) <sup>a</sup>		
			Pure NN (KBr pellet)	Formulation (KBr pellet)	Pure NN (thin film) <sup>71,76</sup>
Dinotefuran	Safari®	254	1.5 ± 0.6	1.8 ± 0.7	8.6 ± 2.3
		305	0.35 ± 0.14	0.37 ± 0.19	3.3 ± 0.5
Nitenpyram	Capstar™	254	1.1 ± 0.5	1.6 ± 0.5	12 ± 4
		305	0.21 ± 0.11	0.21 ± 0.08	1.0 ± 0.3
		350	0.20 ± 0.06	0.084 ± 0.04 <sup>b</sup>	0.94 ± 0.15

<sup>a</sup> Quantum yield ( $\phi$ ) is defined as the rate of loss of the NN divided by the rate of absorption of photons. Each entry should be multiplied by  $10^{-3}$ , e.g., the first quantum yield is  $(1.5 \pm 0.6) \times 10^{-3}$ . Standard deviation ( $1 \sigma_\phi$ ) is determined by uncertainties in the NN photolysis rate constants ( $k_{NN}$ ) and the measurement of the intensity correction factor (CF) from the 2NB photolysis rate constant ( $k_{2NB}$ ), calculated as:  $\frac{\sigma_\phi}{\phi} = \left[ \left( \frac{\sigma_{k_p}}{k_p} \right)^2 + \left( \frac{\sigma_{CF}}{CF} \right)^2 \right]^{\frac{1}{2}}$

where uncertainties in  $\Sigma\sigma I$  are taken to be negligible compared to those in  $k_p$  and CF.

<sup>b</sup> The quantum yield at 350 nm for NPM has not been corrected for a possible change in absorption cross section due to adsorbed water. The value shown is therefore a lower limit.

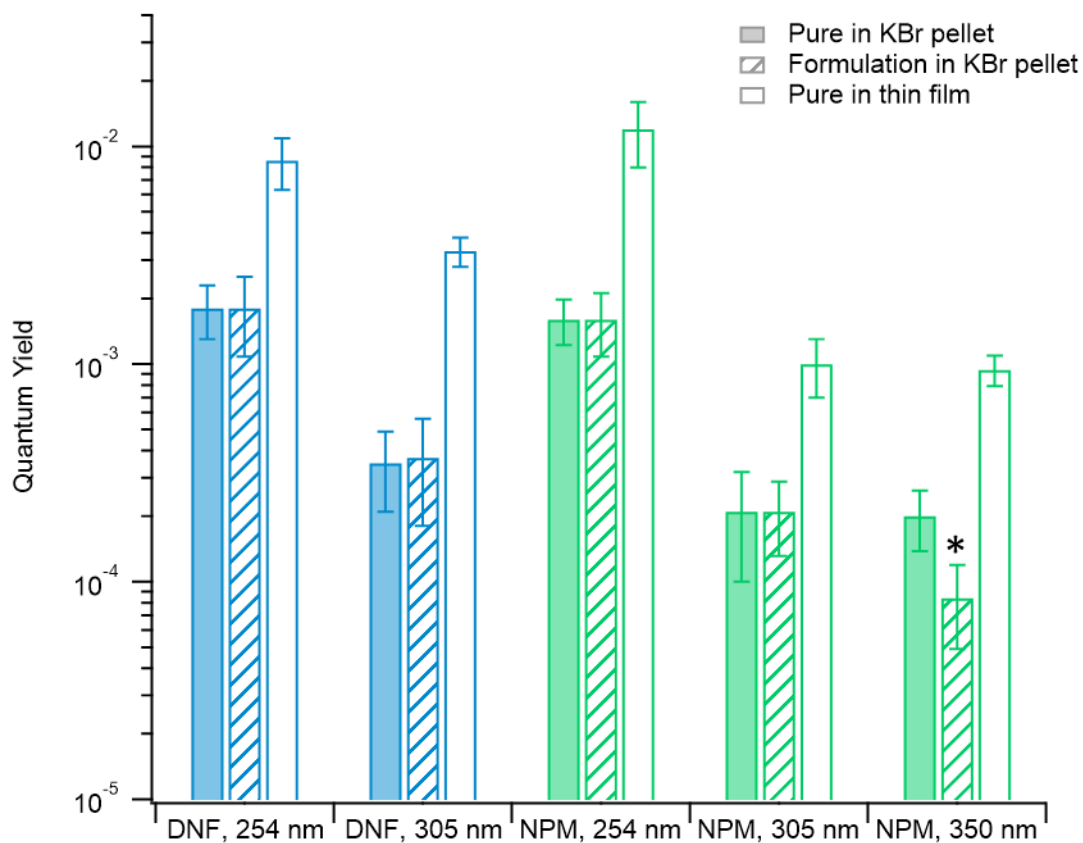


Figure 3.17 Quantum yields for pure NN in thin films and pure and formulated NN in KBr pellets. Errors are  $\pm 1 \sigma$ . The asterisk (\*) indicates that the quantum yield at 350 nm for NPM has not been corrected for a possible change in absorption cross section due to adsorbed water. The value shown is therefore a lower limit.

In KBr pellets, quantum yields are lower by a factor of ~5-10 than in thin films across all irradiation wavelengths. This is likely due in part to the high optical density of the pellet shielding the NN, as well as the high density KBr matrix affecting the photolysis reaction. As discussed in detail in previous papers<sup>70,71,76</sup> and shown in **Fig. 3.8**, the first step in the photolysis is scission of the  $-\text{NO}_2$  bond. Recombination with the organic fragment simultaneously formed releases the bond energy into the regenerated molecule, precipitating a set of internal rearrangements and reactions that lead to the observed

products. The presence of the high-density solid matrix likely damps some of the excess energy, resulting in the lower quantum yields observed in the KBr pellets.<sup>44,117</sup>

There were no significant differences in quantum yields at 254 and 305 nm between the pure and formulated DNF in a KBr matrix (**Table 3.2**). This was also true for NPM at both wavelengths. However, at 350 nm, the NPM quantum yield in the formulation decreased by about a factor of two compared to pure NPM in KBr pellets. UV-Vis absorption cross sections for NPM in the 350 nm region are known to be greatly reduced in the presence of water,<sup>118</sup> and thus uptake of water into the KBr pellet by the additional ingredients in the commercial formulation, which includes such compounds as silica (a well-known desiccant), cellulose, and starch, could alter the effective absorption cross section at 350 nm. As shown in **Fig. 3.18a**, UV-Vis absorption spectra do indeed show reduced relative absorption near 350 nm for the Capstar™/KBr pellets compared to pure NPM in the KBr pellet or NPM in acetonitrile solution. Comparison to the lamp emission spectra also shown in **Fig. 3.18b** shows this shift in absorbance would affect quantum yield calculations for the 350 nm lamp much more than the 305 nm lamp calculations. In that case, the true quantum yield may in fact not change significantly at 350 nm in different matrices.



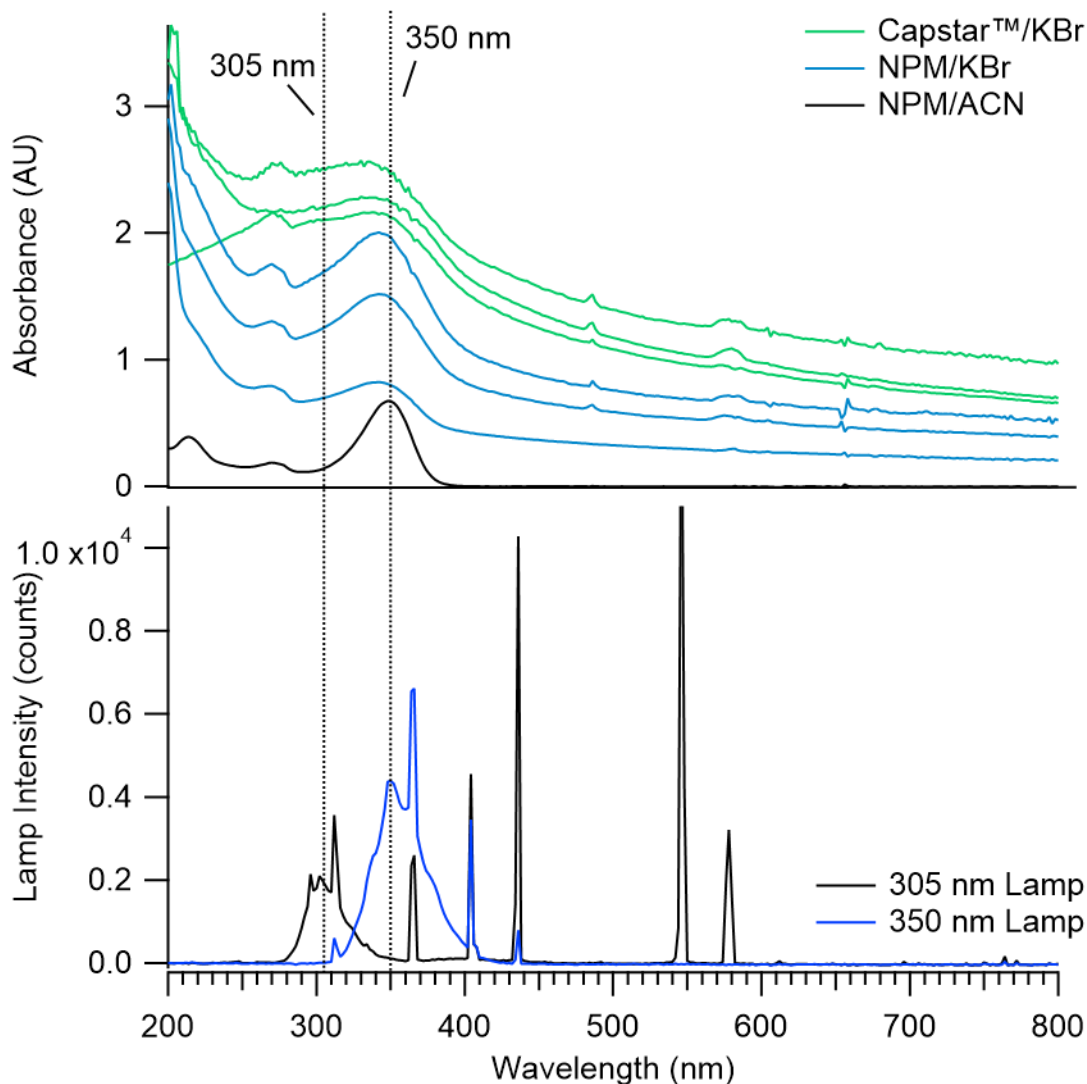


Figure 3.18 UV-Vis absorbance spectra (top) of 0.36 mM NPM in acetonitrile, 0.48% NPM/KBr (w/w), and 4.8% Capstar™/KBr and photolysis lamp emission spectra (bottom). Obtaining quantitatively reproducible spectra of solids is difficult due to the inhomogeneity of the pellets and light scattering differences so three runs of each were carried out, green are replicate runs of Capstar™ in KBr and blue are NPM in KBr.

It should be noted that the absorption cross sections used for the calculated quantum yields of NN in KBr pellets were for the NN in solution. Absorption cross sections in the KBr pellet were highly variable due to pellet inhomogeneity (**Fig. 3.18**) but did not show significant differences qualitatively from the solution spectra. Thus, for the purpose of

comparing the pure NN to the commercial formulation, we found it sufficient to use one consistent absorption cross section represented by the NN in solution.

### **3.10 Conclusions**

When considering the fate of the NNs in the environment, it is important to note that the high-pressure environment required to form KBr pellets, which is responsible for the difference in degradation rates observed here, is not representative of field conditions. Therefore, quantum yields, lifetimes, and products predicted using thin films are likely more relevant to field conditions. The KBr pellet process was essential, however, to compare the commercial formulation to the pure NN, which showed that laboratory experiments using the pure reagents can be representative of the commercial formulations.

The present studies show that the  $N_2O$  and quantum yields from photolysis of DNF and NPM are relatively insensitive to the presence of inert commercial formulation ingredients. Calculated quantum yield values for loss of NPM at 350 nm, however, were reduced by about a factor of two in the commercial formulation which is attributed to reduced absorption cross sections arising from uptake of water by the additional formulation ingredients. Major photodegradation products in KBr pellets were also similar in the pure NNs and the commercial formulations. Major DNF photodegradation products include a desnitro and urea derivative. By analogy to IMD, the desnitro product may have increased toxicity<sup>42</sup> compared to the parent compound.

There were two unexpected products observed by IR in the fused solid KBr matrix of both the pure and commercial formulations that are not observed in the thin film irradiations. One which was observed in significant intensity only in the photolysis of DNF

was assigned to  $\text{NO}^+$ . Structural insights into why this NN behaved differently points to the dimer crystal structure of DNF where only one of the oxygens in the  $-\text{NO}_2$  group is involved in hydrogen bonding, in contrast to IMD, for example, where both  $-\text{NO}_2$  oxygens are hydrogen bonded. The single hydrogen bond in DNF may facilitate isomerization to  $-\text{ONO}$  in the excited state, which led to production of  $\text{NO}^+$  in the ionic KBr matrix.

The second unexpected product using KBr pellets was determined to be  $\text{N}_2\text{O}$  trapped in the solid phase, which was observed to diffuse to the gas phase over time. This was seen in all NNs that generate gas phase  $\text{N}_2\text{O}$ . Trapped  $\text{N}_2\text{O}$  was observed in fused solid KBr pellets but not in fused solid Cabosil<sup>®</sup> pellets, suggesting the  $\text{N}_2\text{O}$  trapping is sensitive to the environment.  $\text{N}_2\text{O}$  yields were observed to be lower in the fused solids than in earlier measurements of thin films on ATR crystals, but were similar to the yields measured from pure NN deposits on transmission windows.

In summary, the quantum yields and products from the commercial formulations in KBr are very similar to those for the pure NNs in KBr, suggesting that the use of the pure compounds in laboratory studies yields data relevant to actual use in the field. The one exception is photolysis of NPM at 350 nm, where increased water uptake by the additional ingredients in the formulation reduces the absorption cross section of NPM and hence its calculated quantum yield, whose true value may not in fact change in the absence of water uptake.

## CHAPTER 4: HYDROXYL RADICAL OXIDATION REACTIONS WITH NEONICOTINOIDS

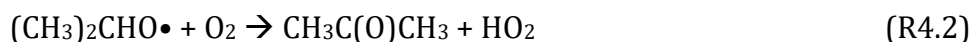
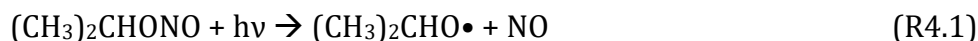
### 4.1 Research Goals

In this study, in situ attenuated total reflection (ATR) FTIR spectroscopy and mass spectrometry are used to investigate the heterogeneous reactions of solid imidacloprid (IMD), dinotefuran (DNF) and clothianidin (CLD) thin films with OH radicals at room temperature. Reaction probabilities and corresponding estimated lifetimes are reported. Product identification was carried out using UPLC-HESI-HRMS and ambient DART-MS and a reaction mechanism is proposed.

### 4.2 Methods

#### 4.2.1. OH generation

Photolysis of isopropyl nitrite (IPN, Karl Industries, Ohio) in a stream of O<sub>2</sub> (Ultrahigh purity, > 99.993%, AirGas) carrier gas was used to generate OH via a series of reactions described in detail elsewhere.<sup>119,120</sup>



The carrier gas passed over the IPN at 263 K and the IPN concentration was measured before and after each reaction using infrared spectroscopy in a 10 cm cell. An absorption cross section of  $1.61 \times 10^{-18} \text{ cm}^2$  (base e) at  $1664 \text{ cm}^{-1}$ <sup>119</sup> was used, giving concentrations ranging from  $(1.5\text{-}2.8) \times 10^{16} \text{ molecules cm}^{-3}$ .

During the experiment, a high pressure Xe lamp (Ushio 300 W bulb, UXL-302-0) mounted in a housing with a power source (Newport model 69911) was used to photolyze the IPN vapor above the NN film. The light beam passed through a water filter and a 360 nm optical filter (Newport longpass colored glass alternative filter, 20CGA-360), and the beam was directed into the cell via a reflecting mirror.

#### 4.2.2. OH measurement

OH concentrations were measured by monitoring formation of  $^{13}\text{CO}_2$  from the reaction of  $^{13}\text{CO} + \text{OH}$  under static conditions. A known concentration of  $^{13}\text{CO}$  was added to the IPN/ $\text{O}_2$  gas mixture in a FTIR gas cell and photolyzed for 20 seconds to two minutes in static conditions. The evolution of  $^{13}\text{CO}_2$  was monitored over time using its absorbance at  $2268\text{ cm}^{-1}$  (**Fig. 4.1a**) and a calibration curve (**Fig. 4.1b**) to convert absorbance to molecules  $\text{cm}^{-3}$ . The concentration of OH was then calculated using the following rate equation,

$$\frac{d^{13}\text{CO}_2}{dt} = k_{\text{CO}+\text{OH}}[^{13}\text{CO}][\text{OH}] \quad (4.1)$$

where  $k_{\text{OH}+\text{CO}}$  at 298 K is  $2.4 \times 10^{-13}\text{ cm}^3\text{ molecule}^{-1}\text{ s}^{-1}$ ,<sup>121</sup>  $d^{13}\text{CO}_2/dt$  is the amount of  $^{13}\text{CO}_2$  generated at time  $t_n$  minus the amount of  $^{13}\text{CO}_2$  generated at  $t_{n-1}$  (**Fig. 4.1c**). A polynomial fit of the calculated OH concentrations at each time interval was then used to obtain the initial concentration at 0 seconds (**Fig. 4.1d**). The concentration of OH using this technique was calculated to be in the range of  $(5.4 \pm 1.8) \times 10^8\text{ molecules cm}^{-3}$ .

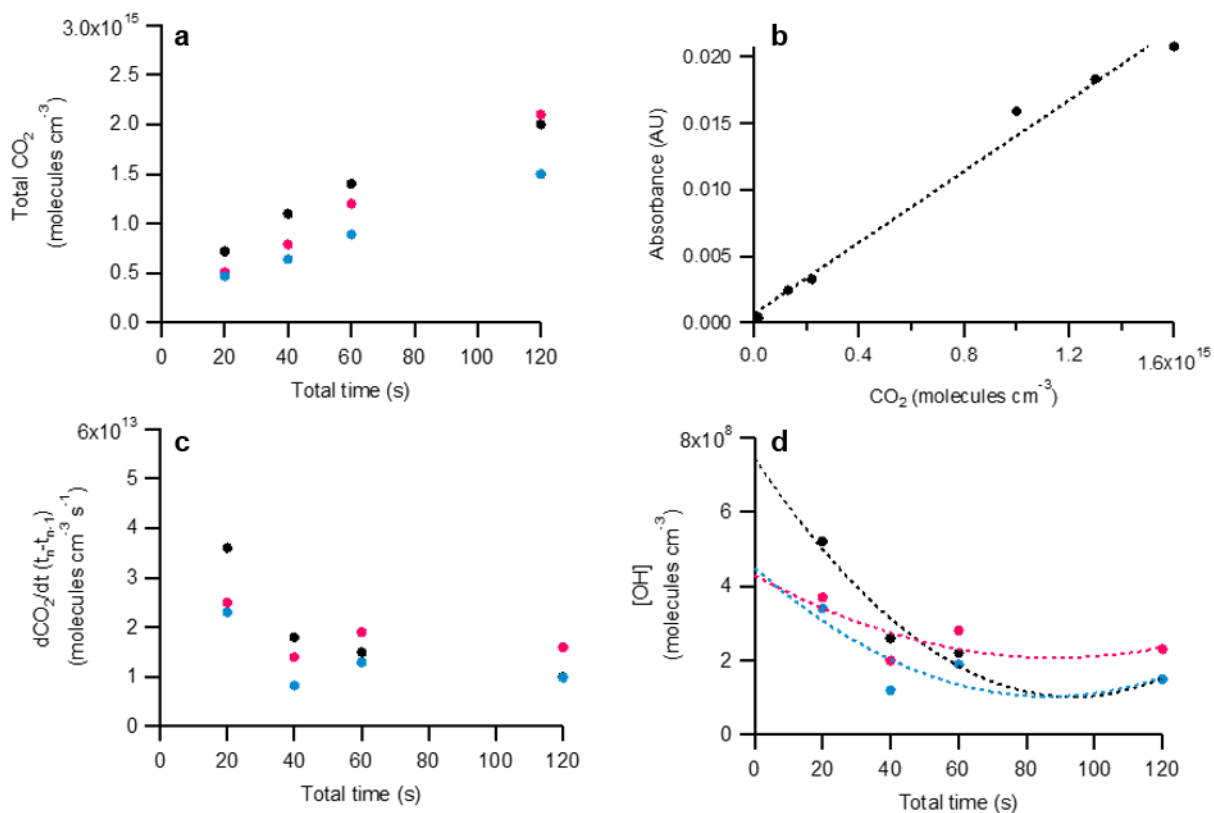


Figure 4.1: (a) observed total  $^{13}\text{CO}_2$  from  $2268 \text{ cm}^{-1}$  peak in FTIR, (b) calibration curve for  $^{13}\text{CO}_2$  using  $2268 \text{ cm}^{-1}$  peak, (c) amount of  $^{13}\text{CO}_2$  generated in each photolysis interval, and (d) calculated OH concentration from  $^{13}\text{CO} + \text{OH}$  reactions and their polynomial fits to determine  $[\text{OH}]$  at  $t=0$ . Colors represent three different trials.

### 4.2.3. NN thin film preparation

The neonicotinoids used were IMD (Sigma-Aldrich, PESTANAL<sup>TM</sup>), DNF (ChemService, 99.5% purity), and CLD (ChemService, 99.5% purity) and were prepared in 20 mM mixtures in acetonitrile (Fisher Chemical, HPLC-grade). A 10  $\mu\text{L}$  aliquot of the solution was pipetted on to the surface of a ZnSe ATR crystal and dried under a stream of  $\text{O}_2$ , forming a thin film as the solvent evaporated. The ATR crystal (Pike Technologies) is trapezoidal shaped with dimensions of 80 mm (l) x 10 mm (w) x 4 mm (d), a 45 degree entrance angle, and 10 bounces, resulting in a depth of penetration ( $d_p$ )<sup>69</sup> of 0.72 to 0.74  $\mu\text{m}$  at  $1615\text{-}1560 \text{ cm}^{-1}$  where the NNs were monitored. After each use, the ATR crystal with the thin NN film was rinsed with Nanopure water and acetonitrile followed by 10 minutes of

argon plasma cleaning (Harrick, PDC-32G). The ATR crystal was mounted in a custom reaction cell<sup>120</sup> and held in the stream of O<sub>2</sub> carrier gas for 15 minutes in the dark before reaction.

#### 4.2.4. ATR FTIR cell measurements

The ATR cell is mounted on an ATR horizontal holder (Pike Technologies) with a quartz window at the top to allow photolysis from the top down. An optical filter is placed on top of the quartz window to remove light below 360 nm in order to reduce photolysis of the NN whose light absorption is weak in this region (**Fig. 4.2**). The carrier gas flow was controlled at 500 sccm using a mass flow controller (Alicat, Model # MC500-SCCM-D/5M) and could either flow directly into the cell, or be routed into the headspace of a trap containing liquid IPN at 263 K.

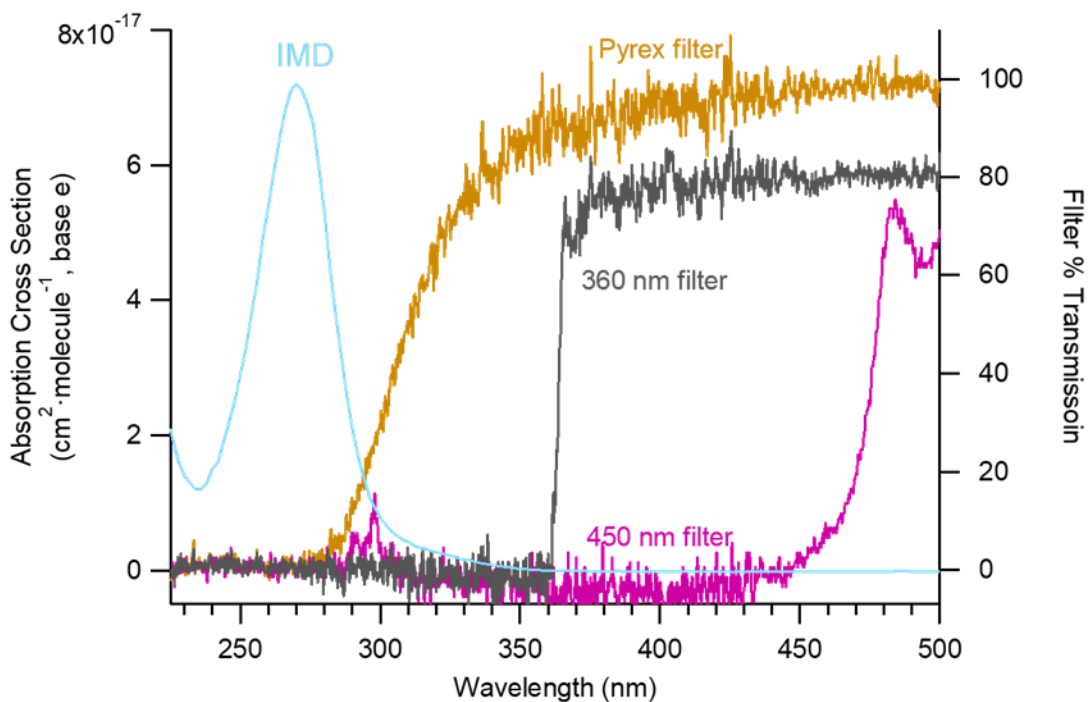


Figure 4.2: Lamp filter cut offs (right axis) overlaid with the IMD absorption cross section (left axis). DNF and CLD have similar absorption cross sections.

Before reaction with OH, a reference spectrum of the dry NN film was taken using 16 scans at a resolution of  $0.5\text{ cm}^{-1}$ . FTIR spectra were then recorded at 30-minute intervals. Absorbance data were converted to number of NN molecules  $\text{cm}^{-2}$  using a calibration curve to convert absorbance to number of molecules and dividing by the usable area of the ATR crystal ( $4\text{ cm}^2$ ). The calibration curve was generated by adding a known number of molecules (10  $\mu\text{L}$  aliquots of 4-40 mM solutions) to the ATR crystal and recording the absorbance of the thin films after evaporation of the solvent. (**Fig. 4.3**)

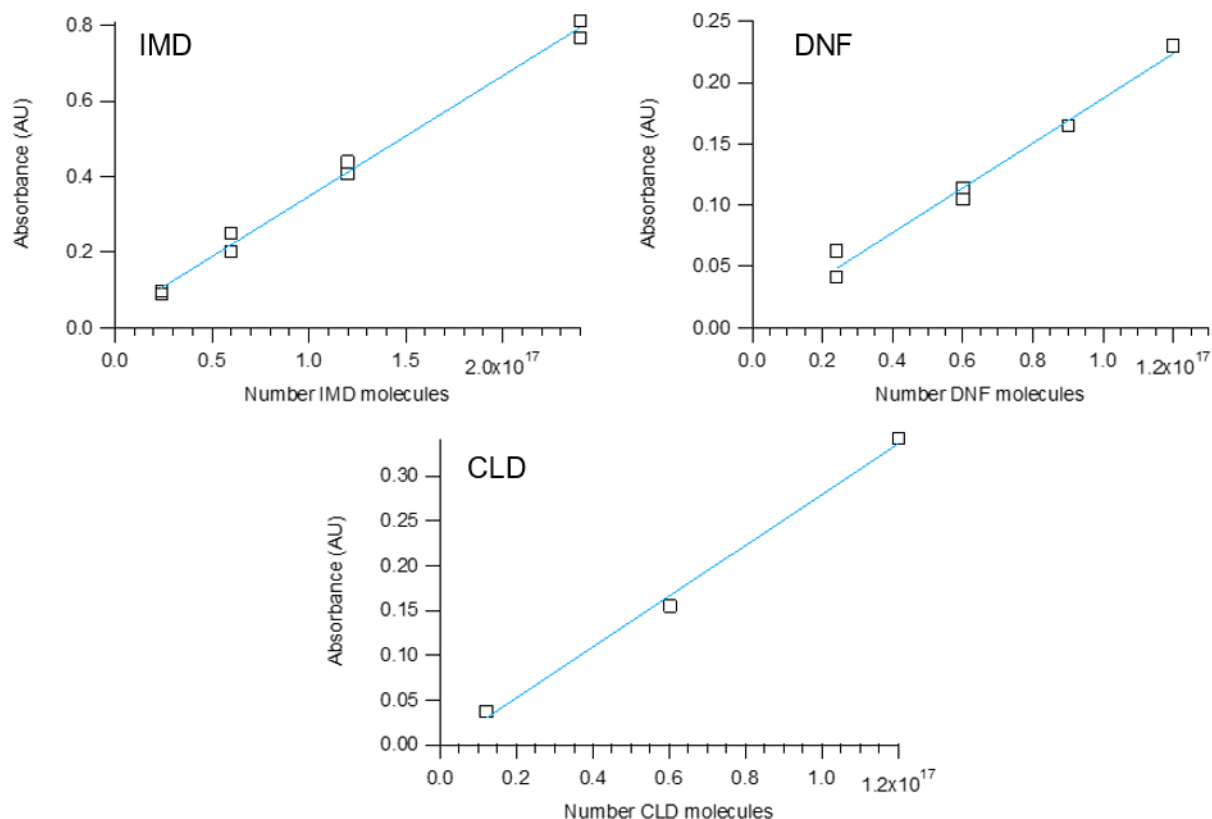


Figure 4.3: Calibration curves of thin films of NN on ZnSe crystals using FTIR.



After the reaction, the ATR crystal was removed from the holder, and the reacted film was analyzed via mass spectrometry, either directly on the ATR crystal by DART-MS or HRMS on extracted samples, as described below.

#### **4.2.5. Product Analysis by Mass Spectrometry (HRMS and DART-MS)**

##### *HRMS*

Accurate mass measurements were performed using a high-resolution mass spectrometer on the UPLC-HESI-HRMS system (ThermoScientific), which includes a Vanquish Horizon UPLC system (with a binary LC pump, an autosampler, a column manager and a diode array detector) coupled to a high-resolution Q Exactive Plus Orbitrap mass spectrometer. The molecular formulae of products were obtained from the high-resolution MS, and the UPLC system allowed for the separation of isomers. This technique requires the sample to be extracted from the surface in a liquid solvent but provides a highly reproducible bulk measurement of the sample. A 1 mL mixture of 90% nanopure water/10% acetonitrile (HPLC grade) was used to extract the NN films from the ATR crystal.

The sample injection volume was 10  $\mu\text{L}$ . A Luna Omega 1.6  $\mu\text{m}$  Polar C18 150  $\times$  2.1 mm column (Phenomenex) fitted with a SecurityGuard ULTRA cartridge (porous polar C18, 2.1 mm; Phenomenex) was maintained at 30  $^{\circ}\text{C}$ . The mobile phase combination was (A) 0.1% formic acid (Fisher Chemical) in HPLC-grade water (Fisher Chemical) and (B) 0.1% formic acid in HPLC-grade acetonitrile (Fisher Chemical). The flow rate was set to 300  $\mu\text{L min}^{-1}$  with the following gradient: 0-3 min hold at 5% B, 3-14 min linear gradient to 95% B, 14-16 min hold at 95% B, 16-22 min linear gradient back to 5% B.

The samples were introduced into the mass spectrometer using a heated electrospray source (HESI; ThermoScientific). Source conditions were as follows: capillary voltage, 4.0 kV; capillary

temperature, 325 °C; sheath gas flow rate, 35; auxiliary gas flow rate, 10; sweep gas flow rate, 8; S-lens RF level 30; auxiliary gas heater temp, 300 °C. The analysis was conducted in ESI(+) ion mode using the full scan data-dependent MS/MS (FS-ddMS2) technique, in which full MS scans were recorded over the  $m/z$  50-750 mass range while MS/MS scans were recorded for the top 3 most abundant ions from the adjacent full MS scan. MS scans have a resolution of 140,000, an automatic gain control (AGC) target of  $10^6$ , and maximum injection time (IT) = 100 ms. MS/MS scans have a resolution of 17,500; AGC target of  $5 \times 10^4$ , maximum IT 50 ms. The MS/MS scans use normalized collision energies of 10, 30 and 50, and the resultant MS/MS spectra are the sum of all the fragment ions observed at all 3 collision energies.

The mass spectrometer was calibrated weekly for mass accuracy using the ThermoScientific Pierce LTQ Velos ESI positive calibration mixture containing butylamine, caffeine, MRFA and Ultramark-1621. The data were acquired using Xcalibur 4.2 software (ThermoScientific) in positive mode where  $[M + H]^+$  are the expected parent peaks and processed with Freestyle v1.6 and MZmine 3.<sup>122</sup>

#### *DART-MS*

The second technique, Direct Analysis in Real Time (DART)-MS, provides ambient sampling of the surface directly without the need for solvent extraction. Volatilization from the ATR crystal surface into the source requires high temperatures (reagent gas flow temperature set at 500 °C). Results from DART are sensitive to the individual location sampled and are thus more variable if there is heterogeneity in the sample. This approach used a commercial DART ion source (IonSense, DART SVP with Vapor Interface) interfaced to a triple quadrupole mass spectrometer (Xevo TQS, Waters). The DART-MS ion source was positioned directly in front of the mass spectrometer source inlet with a 4 cm space for the sample. Helium was used as the reagent gas flowing at  $3.1 \text{ L min}^{-1}$  and subject to a grid electrode voltage of 350 V and a reagent gas

temperature set to 500 °C. After photolysis of the NN thin film, the ATR crystal was held at the ion exit of the DART accessory and mass spectra were collected from  $m/z$  2 to 1000 using MassLynx software in the positive ion mode, where  $[M + H]^+$  are the expected parent peaks.

### 4.3 In situ monitoring using ATR FTIR

**Figure 4.4** shows the ATR-FTIR spectra before and after reaction. The grey traces are the initial FTIR spectra of IMD, DNF, and CLD showing the characteristic  $-\text{NO}_2$  asymmetric stretches in the 1615-1560  $\text{cm}^{-1}$  region.<sup>82</sup> Difference spectra, defined as  $\log S_0/S_1$  where  $S_0$  is the single beam of the NN in the dark under the flow of  $\text{O}_2$  and  $S_1$  is the single beam at the selected reaction time, were obtained at 30-minute intervals. The blue traces are the difference spectra after ~16 hours reaction with OH. Negative peaks indicate reactant loss and positive peaks indicate product formation. For all three NNs, absorption bands due to product formation are observed in the ~1600 – 1800 region, characteristic of C=O (1850-1550  $\text{cm}^{-1}$ ), as well as C=N (1690-1620  $\text{cm}^{-1}$ ) and C=C (1680-1620  $\text{cm}^{-1}$ ) groups.<sup>82</sup> Loss of C-H (3000-2800  $\text{cm}^{-1}$ ) and N-H (3500-3300  $\text{cm}^{-1}$ ) stretches<sup>82</sup> are also observed.

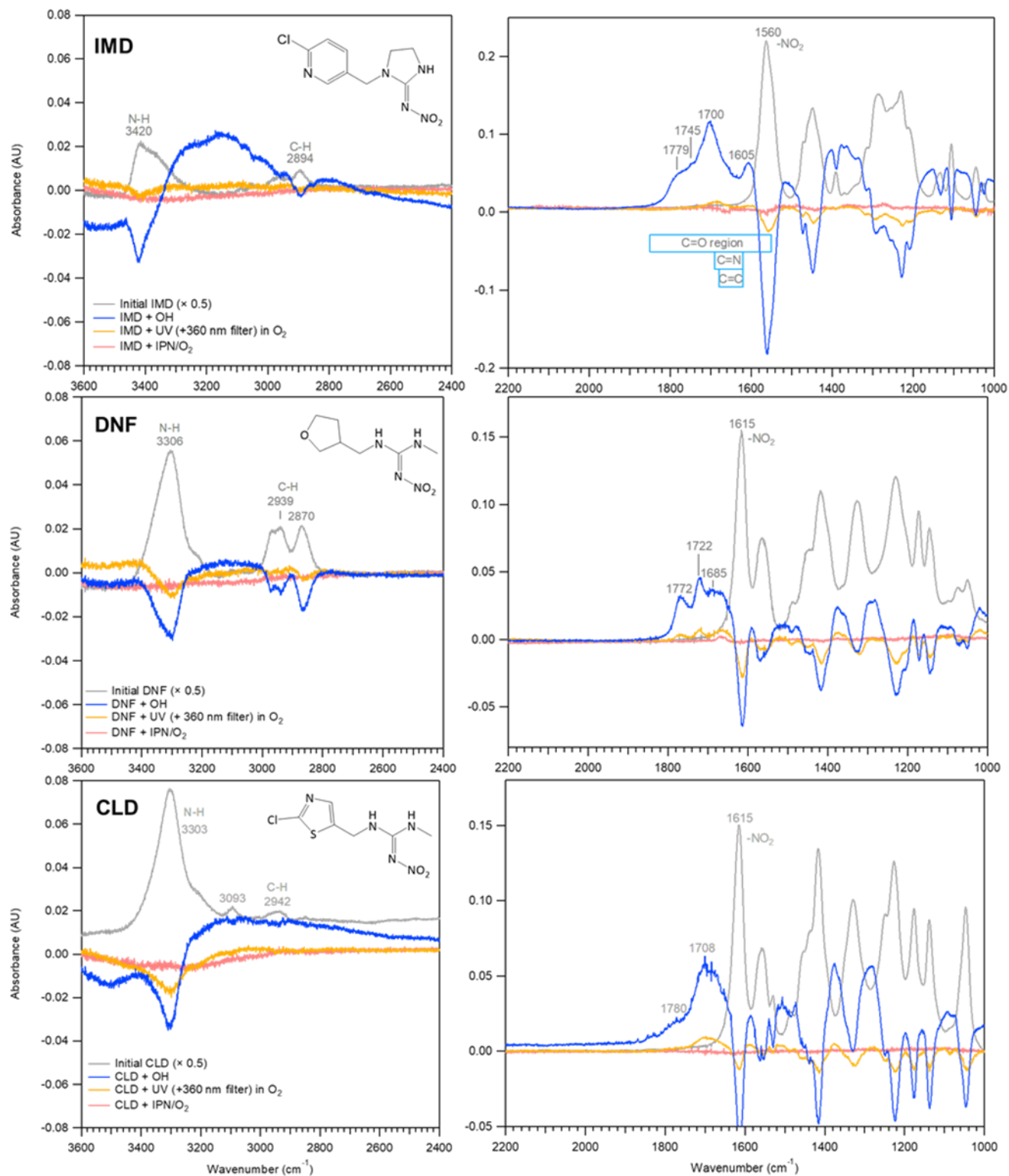


Figure 4.4: FTIR spectra of IMD, CLD, and DNF (grey) and difference spectra after reaction, which show  $\log S_0/S_1$  where  $S_0$  is the single beam of the NN before reaction and  $S_1$  is the single beam at the selected reaction time. The first is reaction with OH (blue), the second is exposure to UV and the 360 nm filter, and the third is exposure to IPN in the dark (pink). Initial absorbance spectra have been scaled by a factor 0.5.

To test for the loss of the NN in the absence of OH, difference spectra were also acquired in control studies of IPN either without the lamp and filter (pink traces, “NN + IPN/O<sub>2</sub>”) or without IPN (yellow traces, “NN + UV (360 nm filter)”). Some loss and product formation were observed under NN + UV (360 nm filter) conditions but no significant changes were detected in the NN + IPN/O<sub>2</sub> flow.

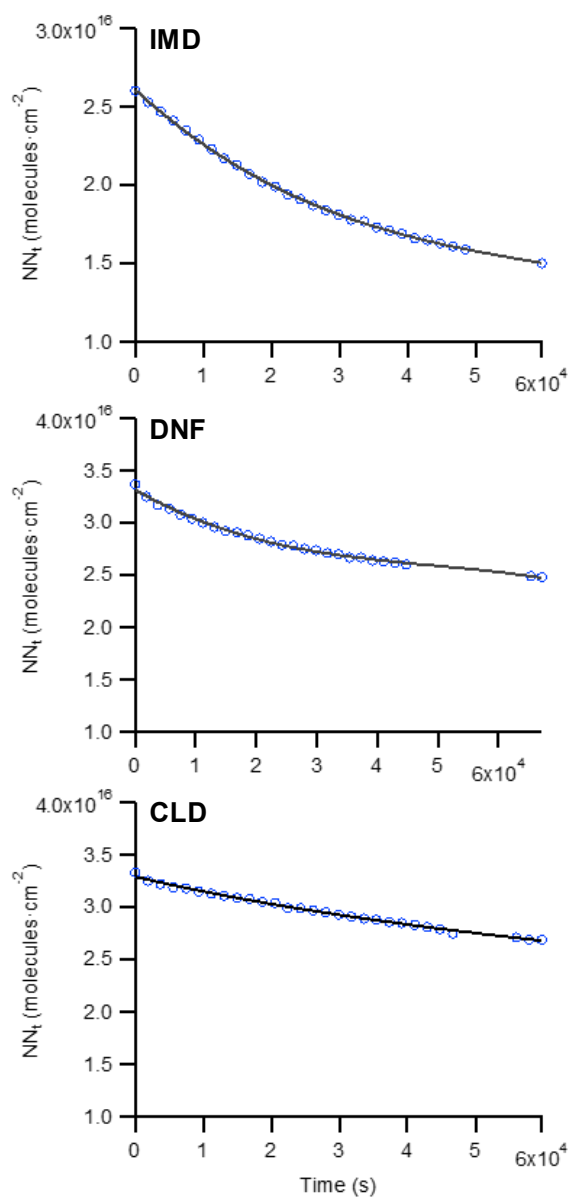


Figure 4.5: Observed loss of IMD ( $1560 \text{ cm}^{-1}$ ), DNF ( $1615 \text{ cm}^{-1}$ ), and CLD ( $1615 \text{ cm}^{-1}$ ) thin films during OH reactions, where the slope at  $t = 0$  on the left graphs is the initial number of reactions  $\text{cm}^{-2} \text{ s}^{-1}$  ( $R_0$ ).

The loss of the -NO<sub>2</sub> asymmetric stretch in **Fig. 4.4** during OH treatment was followed to generate plots of the number of NN molecules per cm<sup>2</sup> (NN<sub>t</sub>) as a function of time (**Fig. 4.5**). A polynomial curve fit is used to determine the slope at t = 0 in **Fig. 4.5**, which is equal to the initial rate of reaction,  $R_0$ :

$$R_0 = \frac{\# \text{ rxns}}{\text{cm}^2 \cdot \text{s}} \quad (4.2)$$

To determine the net uptake coefficient ( $\gamma$ ) for the NN + OH reaction, which is equal to the net rate of uptake of the gas normalized to the rate of gas-surface collisions,<sup>68</sup> the initial number of reactions cm<sup>-2</sup> s<sup>-1</sup> ( $R_0$ ) is divided by the gas concentration and the number of collisions expected from kinetic molecular theory.<sup>68,123</sup>

$$\gamma = \frac{\# \text{ reactions}}{\# \text{ collisions}} = \frac{R_0}{[\text{OH}] \cdot \sqrt{\frac{RT}{2\pi M}}} \quad (4.3)$$

where  $R_0$  is obtained using **Eqn. 4.2**, [OH] is the gas concentration (molecules cm<sup>-3</sup>),  $R$  is the gas constant,  $T$  is temperature (K) and  $M$  is molar mass of OH (kg mol<sup>-1</sup>). The average uptake coefficients ( $\pm$  one standard deviation) are then calculated. As seen in **Table 4.1**, they range from  $(1.7 \pm 0.3) \times 10^{-2}$  for CLD to  $(4.0 \pm .14) \times 10^{-2}$  for IMD.

Table 4.1:  
Uptake coefficients of heterogeneous NN + OH reactions

NN	n	$R_0$ (Initial # rxns $\text{cm}^2 \text{s}^{-1}$ $\pm 1\sigma$ )	$\gamma \pm 1\sigma$	$\gamma$ ratio to IMD
IMD	5	$(3.1 \pm 1.1) \times 10^{11}$	$(4.0 \pm 1.4) \times 10^{-2}$	1
DNF	5	$(2.8 \pm 0.7) \times 10^{11}$	$(3.6 \pm 0.9) \times 10^{-2}$	0.90
CLD	4	$(1.3 \pm 0.2) \times 10^{11}$	$(1.7 \pm 0.3) \times 10^{-2}$	0.41

Abstraction of hydrogens from C-H groups is expected to be the primary reaction step. Using known structure-reactivity relationships (SAR) from gas phase OH reactions with alkanes, relative reactivities for the hydrogen abstraction can be calculated for the three NNs.<sup>68,124,125</sup> The SAR predict that  $k^{\circ}_{\text{sec}}(\text{CH}_2) = 9.34 \times 10^{-13} \text{ cm}^3 \text{ molecule}^{-1} \text{ s}^{-1}$ , with neighboring group factors  $F(>\text{C}<)$  of 1.23 and  $F(-\text{NH}_2)$  of 10. The SAR takes into account effects of adjacent molecules with the neighboring group factors, and thus predicts that C-H groups neighboring N groups will be the most reactive. Evaluation of the NN from the sum of the reactivity of their aliphatic C-H groups predicts gas phase rate constants of  $3.45 \times 10^{-11}$ ,  $2.80 \times 10^{-11}$ , and  $1.28 \times 10^{-11} \text{ cm}^3 \text{ molecule}^{-1} \text{ s}^{-1}$  for IMD, DNF, and CLD respectively. This gives ratios to IMD of 0.93 for DNF and 0.37 for CLD. These ratios for predicted gas phase reaction rates are consistent with the uptake coefficients measured here: DNF is observed to be 0.90 times that of IMD, and CLD is observed to be 0.41 times that of IMD. This calculation ignores the potential reactivity of the N-H groups (which SAR predict to be very reactive but were not observed to be reactive in these studies based on the products observed, as discussed below) and the C-H groups in the aromatic ring structures of IMD and CLD (which SAR do not predict to be as reactive as the aliphatic C-H groups).

## 4.4 Product Identification

### 4.4.1. Imidacloprid

**Fig. 4.6a** shows typical results from HRMS analysis of an OH-reacted IMD sample (blue trace). Similar data are shown for samples before reaction, in which the NN film was formed on the ATR crystal and immediately extracted (grey trace) and in lamp-only conditions (tan trace, in which the sample was exposed to the lamp with a 360 nm filter, but no IPN was present). The parent IMD is observed at  $m/z$  256.0594, where  $[M+H]^+ = C_9H_{11}O_2N_5Cl$ . The dominant products observed from the OH reaction were  $m/z$  270.0387 and 272.0543, each with multiple peaks separated chromatographically. Many smaller peaks were also identified, including peaks at  $m/z$  211.0748, 225.0535, and 254.0438. **Table 4.2** summarizes the major species molecular formulae, number of isomers observed, and proposed structures.



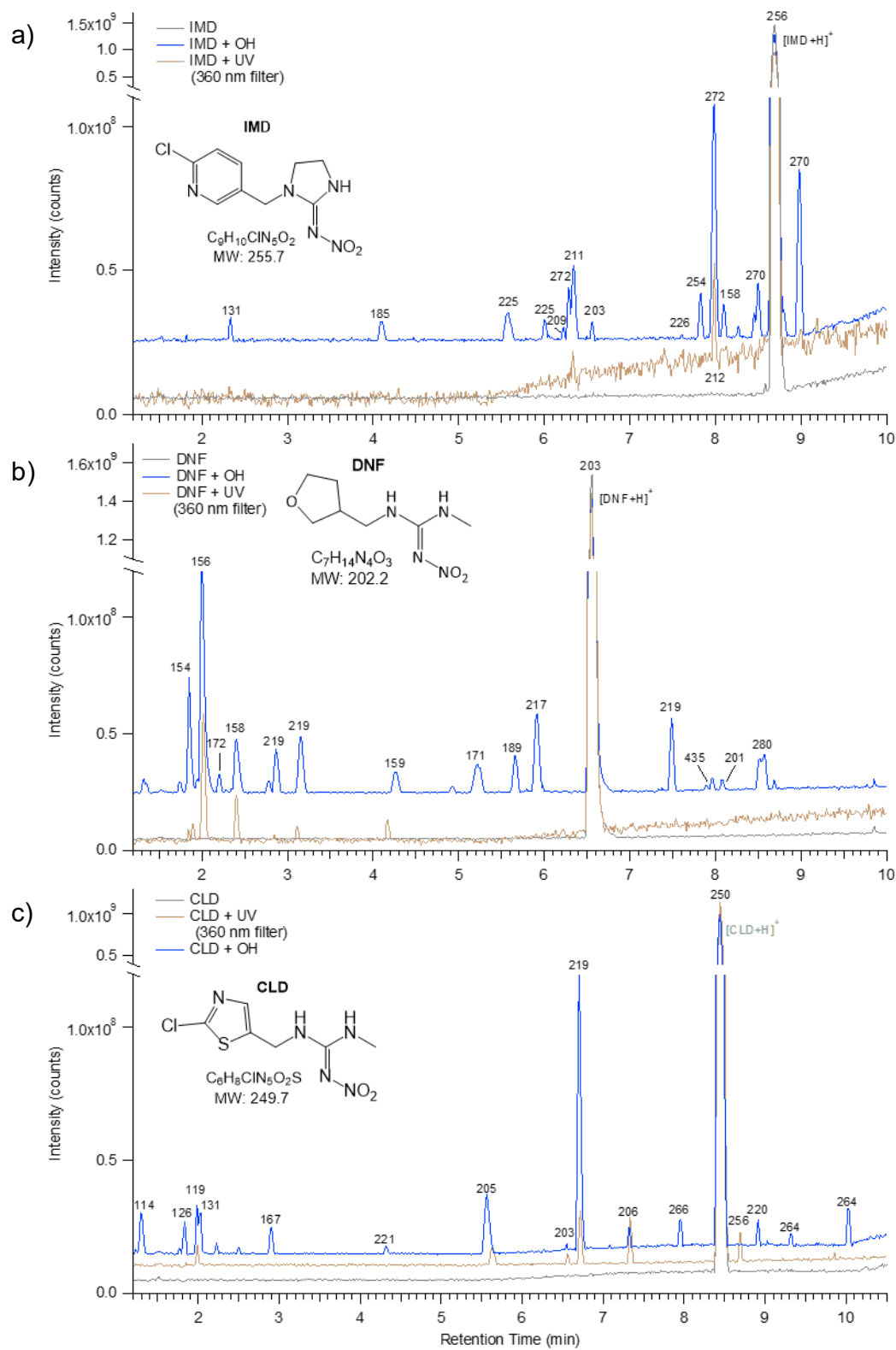
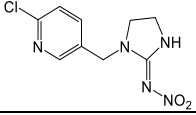
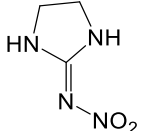
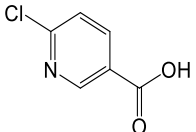
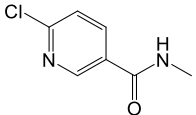
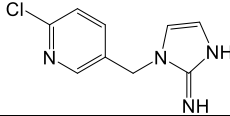
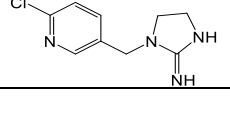
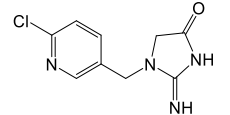
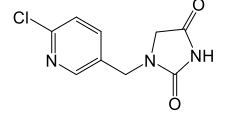
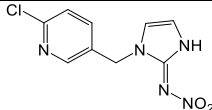
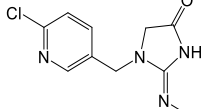
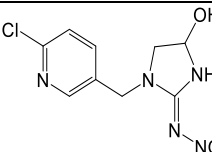
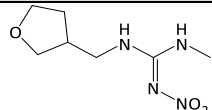
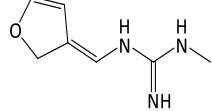
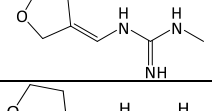
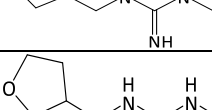

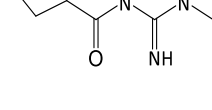


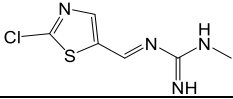
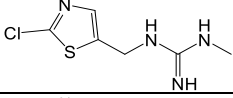
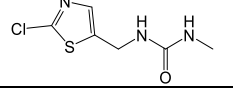
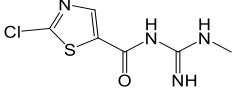
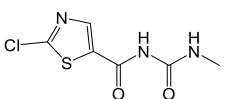
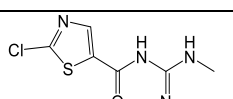
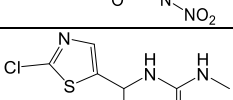
Figure 4.6 Typical HRMS total ion chromatogram (TIC) for (a) IMD, (b) DNF, and (c) CLD after reaction with OH (blue traces), as well as control studies of before reaction (grey traces) and in UV + 360 nm filter conditions (tan traces). Chromatogram peaks are labeled with the major ion observed within that peak.

Table 4.2: Products observed in the oxidation of solid NN by gas phase OH radicals

NN	Precursor Ion	Identity ([M+H] <sup>+</sup> )	Error (ppm)	Isomers <sup>a</sup>	Notes	Proposed Structure <sup>b</sup>
IMD	256.0594	IMD C <sub>9</sub> H <sub>11</sub> O <sub>2</sub> N <sub>5</sub> Cl	-0.75	1		
IMD	131.0562	C <sub>3</sub> H <sub>7</sub> O <sub>2</sub> N <sub>4</sub>	-1.17	1		
IMD	158.0003	6-chloronicotinic acid, C <sub>6</sub> H <sub>5</sub> O <sub>2</sub> NCl	-0.27	1		
IMD	171.032	C <sub>7</sub> H <sub>8</sub> ON <sub>2</sub> Cl	0.38	1	1 major peak associated with only this ion, but also weakly contributing in many other peaks	
IMD	209.0585	C <sub>9</sub> H <sub>10</sub> N <sub>4</sub> Cl	1.47	1, & in source	Largely formed in-source (largest EIC peak is parent IMD peak), but there is a separate smaller peak	
IMD	211.0745	Desnitro IMD, C <sub>9</sub> H <sub>12</sub> N <sub>4</sub> Cl	0.11	1	Likely formed via photolysis, not directly by OH chemistry	
IMD	212.0585	IMD Urea, C <sub>9</sub> H <sub>11</sub> ON <sub>3</sub> Cl	0.01	1 and in source	Likely formed via photolysis, not directly by OH chemistry.	
IMD	225.0535	C <sub>9</sub> H <sub>10</sub> ON <sub>4</sub> Cl	-0.11	2+	Formed via OH reaction with desnitro IMD, Broad peak (RT 5.58) likely two coeluting isomers, and one smaller peak	
IMD	226.0378	C <sub>9</sub> H <sub>9</sub> O <sub>2</sub> N <sub>3</sub> Cl	-0.20	1+	1 broad, asymmetrical peak observed	

NN	Precursor Ion	Identity ([M+H] <sup>+</sup> )	Error (ppm)	Isomers <sup>a</sup>	Notes	Proposed Structure <sup>b</sup>
IMD	254.0438	C <sub>9</sub> H <sub>9</sub> O <sub>2</sub> N <sub>5</sub> Cl	-0.72	1+	1 large isomer peak (RT 7.83), one much smaller	
IMD	270.0387	C <sub>9</sub> H <sub>9</sub> O <sub>3</sub> N <sub>5</sub> Cl	-0.54	2+	1 large and 1 small peak: large peak (RT 8.98) likely two isomers (C=O on 5-membered ring) co-eluting	
IMD	272.0543	C <sub>9</sub> H <sub>11</sub> O <sub>3</sub> N <sub>5</sub> Cl	-0.52	2+	1 large and 1 small peak: large peak (RT 7.98) likely two isomers (C=O on 5-membered ring) co-eluting	
DNF	203.1142	DNF, C <sub>7</sub> H <sub>15</sub> O <sub>3</sub> N <sub>4</sub>	1.4	1		
DNF	154.0976	C <sub>7</sub> H <sub>12</sub> ON <sub>3</sub>	0.2	1+	Peak is somewhat broad and asymmetrical, may have coeluting isomers	
DNF	156.1128	C <sub>7</sub> H <sub>14</sub> ON <sub>3</sub>	-1.14	1+		
DNF	158.1284	Desnitro DNF, C <sub>7</sub> H <sub>16</sub> ON <sub>3</sub>	-1.09	1	Likely formed via photolysis, not directly by OH chemistry.	
DNF	159.1124	DNF Urea, C <sub>7</sub> H <sub>15</sub> O <sub>2</sub> N <sub>2</sub>	-1.13	1	Likely formed via photolysis, not directly by OH chemistry.	
DNF	171.1001	Unknown		1+		
DNF	172.108	C <sub>7</sub> H <sub>14</sub> O <sub>2</sub> N <sub>3</sub>	-0.83	5		

NN	Precursor Ion	Identity ([M+H] <sup>+</sup> )	Error (ppm)	Isomers <sup>a</sup>	Notes	Proposed Structure <sup>b</sup>
DNF	189.0982	C <sub>6</sub> H <sub>13</sub> O <sub>3</sub> N <sub>4</sub>	0.42	1		
DNF	201.0988	C <sub>7</sub> H <sub>13</sub> O <sub>3</sub> N <sub>4</sub>	2.30	3+	1 major (RT 4.93) and then several overlapping smaller peaks (RT ~8.08)	
DNF	217.0928	C <sub>7</sub> H <sub>13</sub> O <sub>4</sub> N <sub>4</sub>	-1.09	4	1 major, 4 minor	
DNF	219.1083	C <sub>7</sub> H <sub>15</sub> O <sub>4</sub> N <sub>4</sub>	-1.33	4	3 major, 1 minor	
DNF	280.0886	C <sub>7</sub> H <sub>14</sub> O <sub>7</sub> N <sub>5</sub>	-1.33	2	Not observed in DART	Unknown
DNF	403.2042	C <sub>14</sub> H <sub>27</sub> O <sub>6</sub> N <sub>8</sub>	-0.65	2	Confirmed <i>m/z</i> 201 dimer by MS/MS analysis in DART, but chromatographically separated in HRMS	<i>m/z</i> 201 dimer
DNF	419.1992	<i>m/z</i> 201 + 217			Confirmed <i>m/z</i> 201 and 217 dimer by MS/MS analysis in DART, not strongly observed in HRMS	<i>m/z</i> 201 + 217
DNF	435.1943	C <sub>14</sub> H <sub>27</sub> O <sub>8</sub> N <sub>8</sub>	-0.9	3+	MS/MS suggests <i>m/z</i> 201 complex	
CLD	250.0158	CLD, C <sub>6</sub> H <sub>9</sub> O <sub>2</sub> N <sub>5</sub> ClS	-0.89	1		
CLD	167.0564	C <sub>6</sub> H <sub>7</sub> O <sub>2</sub> N <sub>4</sub>	-0.01	1		Unknown

NN	Precursor Ion	Identity ([M+H] <sup>+</sup> )	Error (ppm)	Isomers <sup>a</sup>	Notes	Proposed Structure <sup>b</sup>
CLD	203.1144 (RT 6.55)	C <sub>7</sub> H <sub>15</sub> O <sub>3</sub> N <sub>4</sub>	2.45	1		Unknown
CLD	203.0157 (RT 4.70)	C <sub>6</sub> H <sub>8</sub> N <sub>4</sub> ClS	2.04	3	Largest peak in HRMS is in CLD ( <i>m/z</i> 250) peak, but also two very small, separated peaks	
CLD	205.0311	<i>Desnitro CLD</i> , C <sub>6</sub> H <sub>10</sub> N <sub>4</sub> ClS	0.93	1	Likely formed via photolysis, not directly by OH chemistry.	
CLD	206.0152	<i>CLD Urea</i> , C <sub>6</sub> H <sub>9</sub> ON <sub>3</sub> ClS	1.27	1	Likely formed via photolysis, not directly by OH chemistry.	
CLD	219.0101	C <sub>6</sub> H <sub>8</sub> ON <sub>4</sub> ClS	-0.66	2	One peak is much smaller than the other	
CLD	219.9940	C <sub>6</sub> H <sub>7</sub> O <sub>2</sub> N <sub>3</sub> ClS	-1.04	2	Peaks are similar size	
CLD	263.9950	C <sub>6</sub> H <sub>7</sub> O <sub>3</sub> N <sub>5</sub> ClS	-1.13	2		
CLD	266.0108	C <sub>6</sub> H <sub>9</sub> O <sub>3</sub> N <sub>5</sub> ClS	-0.42	2		

<sup>a</sup> Based on number of peaks in extracted ion chromatogram. A + is included after the number of peaks if one of the peaks appears broad, is suspected to be co-eluting isomers, or if there is a small peak with many ions present making it difficult to ascertain if only ion is responsible for the peak.

<sup>b</sup> Only one isomer shown for simplicity. Additional isomers expected.

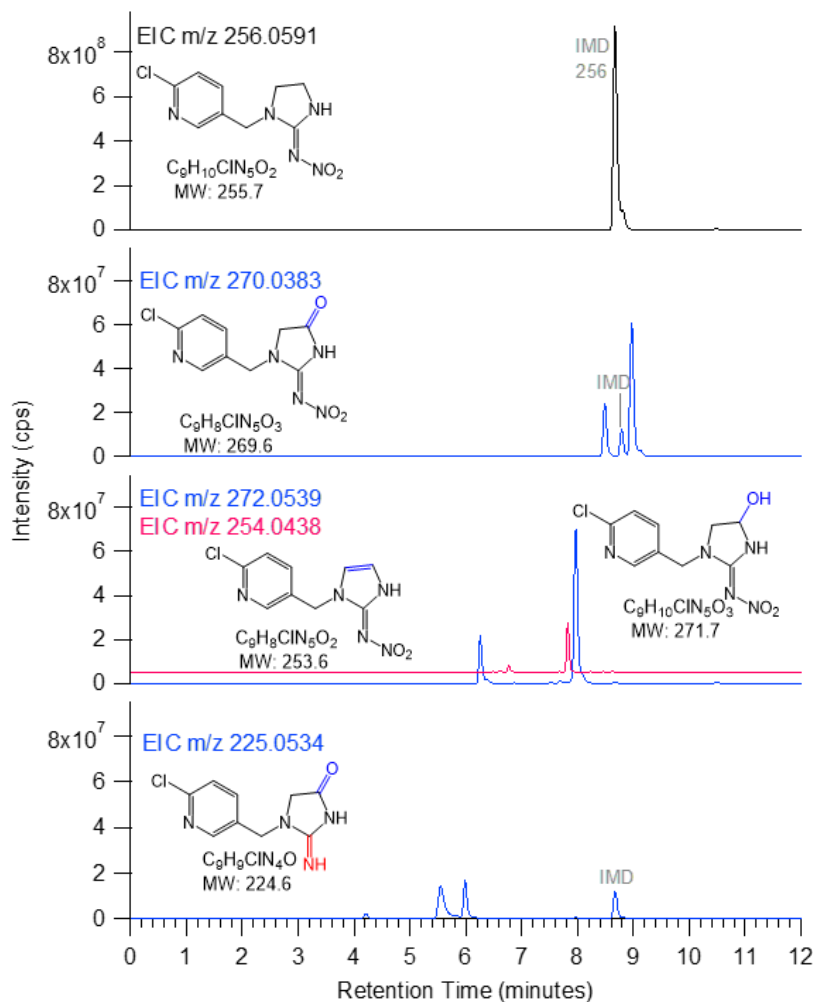


Figure 4.7: Extracted ion chromatogram (EIC) of HRMS peaks at  $m/z$  256, 270, 272, 254 (offset for clarity) and 225 for IMD + OH reactions.

The peaks at  $m/z$  270.0387 are identified as carbonyl-containing products,  $[M+H]^+ = C_9H_9O_3N_5Cl$ , and  $m/z$  272.0543 as alcohol-containing products,  $[M+H]^+ = C_9H_{11}O_3N_5Cl$ . Two isomers are clearly observed for both products in the extracted ion chromatograms (EIC) in **Fig. 4.7** ( $m/z$  270 at 8.49 and 8.98 minutes, and  $m/z$  272 at 6.28 and 7.98 minutes). If these products are formed via hydrogen abstraction from one of the aliphatic C-H groups, three isomers would be expected. However, it is likely that the two potential isomers formed on the 5-membered ring are unable to be resolved chromatographically. Additionally, in both

cases, one of the observable isomer peaks is significantly larger. Thus, either one isomer is formed preferentially and the third is not formed at all, or more likely, the larger peak intensity is in fact due to the contribution of both 5-membered ring isomers. These results are consistent with Rozsa et al. 2019,<sup>126</sup> who found the Cl-pyridine ring carbons to be unreactive with respect to OH in aqueous solution.

Although direct photolysis was minimized by using the 360 nm filter, it appears that some photolysis of the NN did contribute to the observed products. The major solid phase photolysis products are the desnitro and urea derivatives, which form from cleavage of the N-N bond in the C=N-NO<sub>2</sub> chromophore, resulting in a C=NH (desnitro) or C=O (urea) group.<sup>70,83</sup> These products were observed in the IMD + OH reaction, but were likely formed from photolysis rather than direct OH attack. The desnitro IMD product is observed at *m/z* 211.0748, and *m/z* 225.0535 is identified as desnitro IMD with a carbonyl group addition. In the latter case, the OH likely reacted with the desnitro IMD photodegradation product similarly to its reaction with the parent IMD species, producing the desnitro-carbonyl final product. This species would be expected to show three isomers, but two major peaks are observed. One of the peaks appears broader than the others (RT 5.58, **Fig. 4.7**), again suggesting the two 5-membered ring isomers may be coeluting. The IMD urea product is observed at *m/z* 212.0585 with a RT of 7.98 minutes only in the control photolysis studies (underneath *m/z* 272 peak observed in OH reaction in the TIC, **Fig. 4.6**).

Seeing product formation from lamp-only control studies was surprising, since these NNs have very little if any absorption beyond 360 nm (**Fig. 4.2**). Additional studies were

conducted to confirm the desnitro and urea products were formed from photolysis and not from thermal reactions; details are given in the SI of Anderson et al.<sup>127</sup>

Product analysis from direct sampling of the ZnSe ATR surface using DART-MS after OH reaction is shown in **Fig. 4.8**. Panel **a** shows a typical DART-MS spectra of the NN on a ZnSe ATR crystal before reaction with OH. The major peaks due to the chlorine isotopes for [IMD+H]<sup>+</sup> are observed at  $m/z$  256/258.

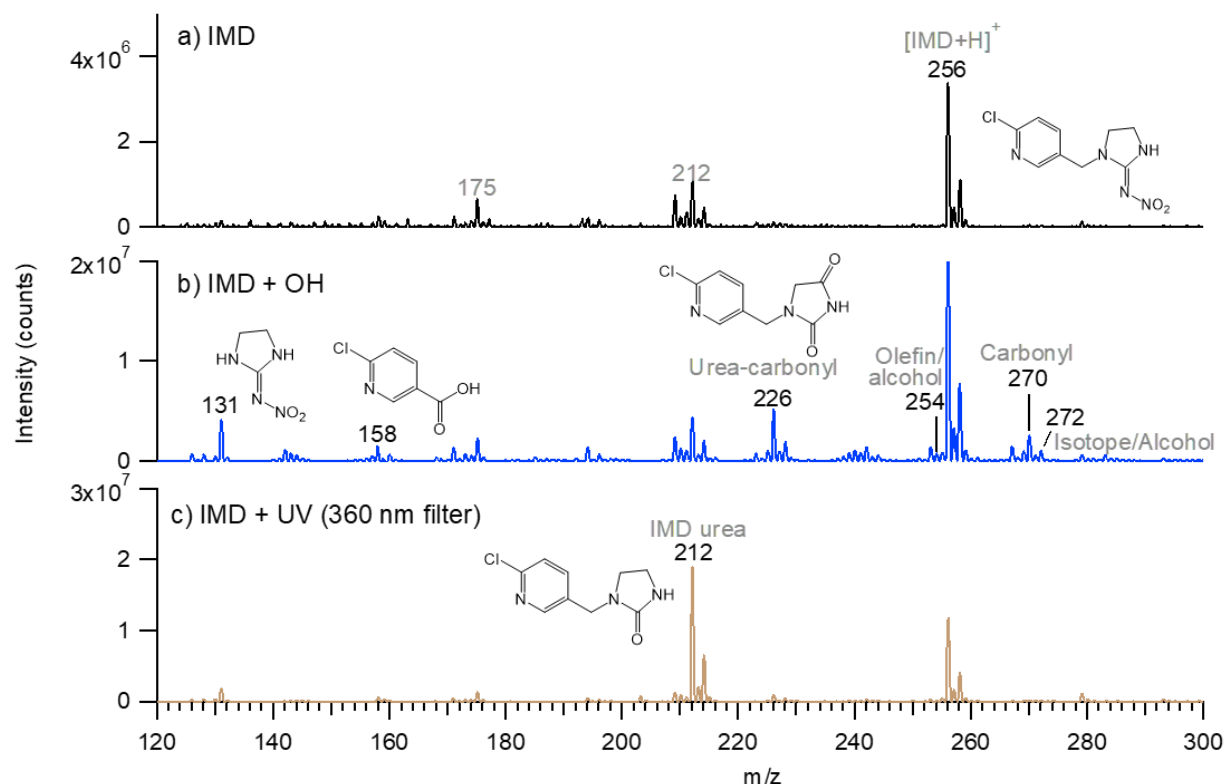


Figure 4.8: Typical DART-MS spectra of IMD samples. The top pane (a) shows IMD on ZnSe before reaction. The second pane (b) shows representative IMD spectra after 15 hours reaction with OH. The bottom pane (c) shows IMD after 20 hours of photolysis with a 360 nm optical filter. Spectra of background room air has been subtracted.



Panel **b** and **c** show product spectra for OH reactions and the control experiments in which the sample was exposed to the lamp with a 360 nm filter, but no IPN was present. Similar to the HRMS results, peaks at  $m/z$  270 and 272, near the ratio expected for the  $^{35}\text{Cl}$  and  $^{37}\text{Cl}$  isotopes, of the carbonyl product are observed after reaction with OH. However, the product at  $m/z$  272 may have some contribution from the alcohol species which observed in the HRMS samples. Additionally, a small product peak is observed at  $m/z$  254, which was identified in HRMS as  $[\text{M}+\text{H}]^+ = \text{C}_9\text{H}_9\text{O}_2\text{N}_5\text{Cl}$ , with an olefin as the proposed structure. Although this double bond may be formed from dehydration of the alcohol in the DART-MS high temperature gas flow, comparison to the HRMS data showed that the alcohol and olefin chromatographically separated (**Fig. 4.7**), and we thus conclude that the olefin is formed as its own unique product of the OH reaction. Additionally, products are observed at  $m/z$  131 and 158 and identified in HRMS as the 5-membered nitroguanidine ring and 6-chloronicotinic acid which has been observed as an oxidation product in a number of aqueous studies.<sup>60,63-65,126,128</sup> These two products are likely to form via further reactions of the  $m/z$  270 carbonyl product with OH.

DART-MS also shows a major peak at  $m/z$  226, which was identified as the IMD urea product with an additional carbonyl moiety based on the HRMS chemical formula. Similar to the desnitro-carbonyl product, this urea-carbonyl product is likely formed by OH reaction with the urea derivative formed from photolysis. The desnitro photolysis product was not directly observed in DART samples, however, separate control experiments of a desnitro IMD standard applied to the ZnSe crystal showed very weak signal in the DART at a range of reagent gas temperatures, suggesting the species is not easily volatilized from the surface. Thus, DART-MS data generally support the conclusions from the HRMS data in showing

formation of the expected photolysis products under these reaction conditions and that these photolysis products undergo further C-H abstraction to form carbonyl products.

#### 4.4.2. Dinotefuran

In HRMS samples of DNF (**Fig. 4.6b**), the peak for the parent DNF is observed at  $m/z$  203.1142, where  $[M+H]^+ = C_7H_{15}O_3N_4$ . Major products unique to the DNF + OH reaction included  $m/z$  217.0928, identified as a carbonyl product,  $[M+H]^+ = C_7H_{13}O_4N_4$ , and  $m/z$  219.1083,  $[M+H]^+ = C_7H_{15}O_4N_4$ , assigned to an alcohol product. While IMD had three potential locations for aliphatic C-H hydrogen abstraction, DNF has six (four CH<sub>2</sub> groups, one CH<sub>3</sub> group, and one CH group). For the  $m/z$  217.0928 carbonyl product, the most intense peak in the EIC (**Fig. 6**) appears at 5.92 minutes, with much smaller peaks at retention times of 3.93 (broad), 5.21, 6.34, and 7.45 minutes, reflecting isomers formed from attack of OH at the different C-H sites. Similarly, for the  $m/z$  219.1083 alcohol product, three significant peaks (2.87, 3.15, and 7.49 minutes) and at least one smaller peak (7.34 minutes) are observed.

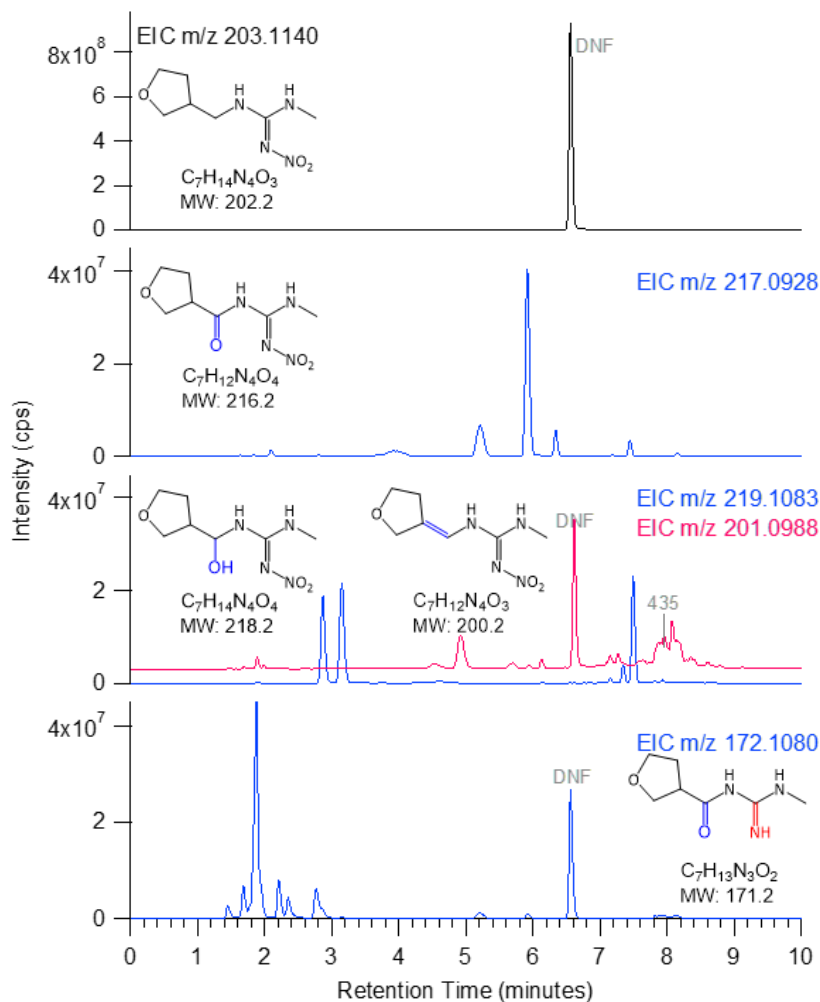


Figure 4.9: Extracted ion chromatograms (EIC) for species with  $m/z$  203, 217, 219, 201 (offset for clarity) and 172 in DNF + OH reaction.

The desnitro and urea photolysis products for DNF are observed in **Fig. 4.6b** at  $m/z$  158.1286,  $[M+H]^+ = C_7H_{16}ON_3$  and  $m/z$  159.1126,  $[M+H]^+ = C_7H_{15}O_2N_2$ , and were also observed in the control DNF + UV (360 nm filter) conditions. Both DNF + OH and DNF + UV (360 nm filter) reactions show a strong signal for a product at  $m/z$  156.1130, identified as the  $[M+H]^+$  peak of  $C_7H_{14}ON_3$ . The proposed structure of this product is a desnitro-olefin. A

desnitro-carbonyl DNF product is also observed in the DNF + OH reaction at  $m/z$  172.1080 with 1 major and 5 minor isomers eluting before 3 min. (**Fig. 4.9**).

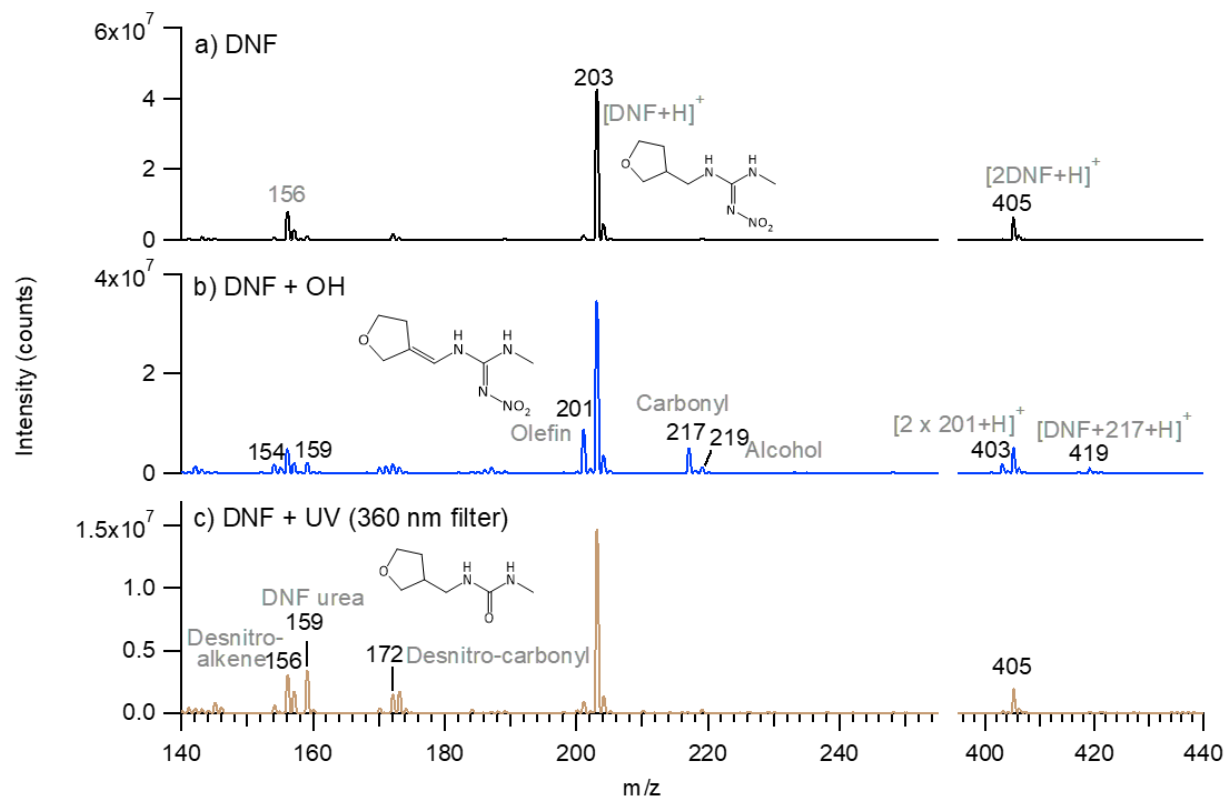


Figure 4.10: Typical DART-MS spectra of DNF samples. The top pane (a) shows DNF on ZnSe before reaction. The second pane (b) shows representative DNF spectra after 16 hours reaction with OH. The bottom pane (c) shows DNF after 18 hours of photolysis with a 360 nm optical filter. Spectra of background room air has been subtracted.

In the DART-MS spectra (**Fig. 4.10**), the major peak due to  $[DNF+H]^+$  is observed at  $m/z$  203 as well as the dimer  $[2DNF+H]^+$  at  $m/z$  405 (**Fig. 4.10a**). In the DNF + OH reaction (**Fig. 4.10b**), products include a carbonyl signal at  $m/z$  217 and a smaller alcohol signal at  $m/z$  219 (note this can be unambiguously attributed to the alcohol because DNF does not have an overlapping Cl isotope). A significant signal is also observed at  $m/z$  201, which was identified in the HRMS as the olefin product. In DART-MS, the olefin is the major signal while

in HRMS, it is much smaller relative to the other product peaks (**Fig 4.6b**). This suggests that the alcohol product may be dehydrated at the higher temperature of the DART-MS, and both OH reaction product formation and in-source formation routes are likely contributing to the signal observed in DART. Dimers of these products were also observed and identified by MS<sup>2</sup> analysis at  $m/z$  403,  $[2 \times 201 + H]^+$ , and  $m/z$  419,  $[DNF + 217 + H]^+$ .

Reactions of DNF also show evidence that the desnitro and urea products are formed from the photolysis-only conditions in agreement with HRMS observations. Similar to IMD, the desnitro DNF product was not directly observed in DNF reactions, although the desnitro-carbonyl and desnitro-olefin species are. Analytical standards of the desnitro DNF (nor desnitro CLD) species are not commercially available to explore their DART sensitivity, but it is likely that these desnitro products are similarly difficult to volatilize from the ATR crystal surface.

#### 4.4.3. Clothianidin

In HRMS samples of the CLD + OH reaction (**Fig. 4.6c**), the major products are similar to those from the IMD and DNF reactions. These include a desnitro-carbonyl product at  $m/z$  219.0101, desnitro CLD at  $m/z$  205.0311, CLD urea at  $m/z$  206.0152, a carbonyl product at  $m/z$  263.9950, and an alcohol product at  $m/z$  266.0108. Both the carbonyl and alcohol show the expected two isomers reflecting attack at the two possible sites for C-H hydrogen abstraction:  $m/z$  263.9950 at 9.32 and 10.02 minutes and  $m/z$  266.0108 at 6.11 and 7.94 minutes (**Fig. 4.11**). The fact that the EIC shows two isomers of similar intensities for the carbonyl product, suggesting that both the CH<sub>2</sub> and CH<sub>3</sub> groups are vulnerable to hydrogen abstraction, is surprising because the SAR for gas phase reactions predict that the terminal

CH<sub>3</sub> group will be less reactive than the CH<sub>2</sub> group. Desnitro CLD, CLD urea, and the desnitro-carbonyl show one major isomer as expected.

For CLD, it seems apparent that photolysis contributed a relatively larger amount to the formation of the products observed in HRMS than were observed for the other two NNs: as shown in **Fig. 4.6c**, the *m/z* 219 desnitro carbonyl group is now the dominant product peak compared to the carbonyl and alcohol products for IMD (*m/z* 270 and 272) and DNF (*m/z* 217 and 219). This is consistent with both the relative kinetics based on having fewer reactive C-H groups predicted by the SAR and the smaller reaction probability observed in these studies.

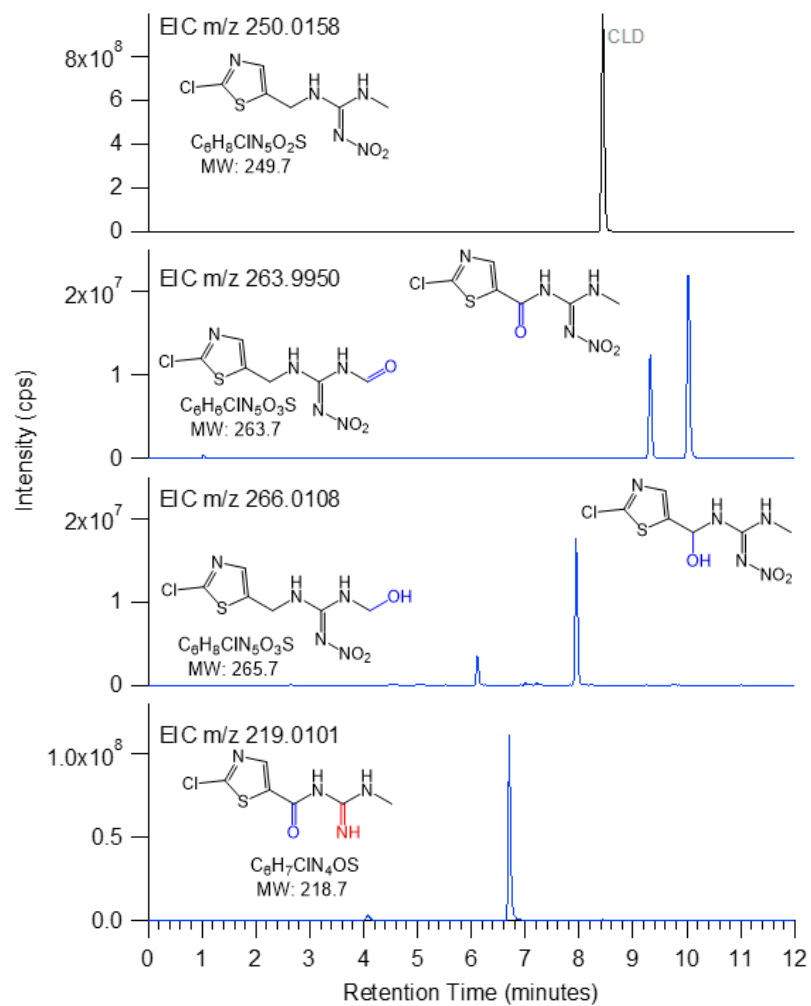


Figure 4.11: Extracted ion chromatograms (EIC) for species with  $m/z$  250, 264, 266 and 219 in CLD + OH reaction.

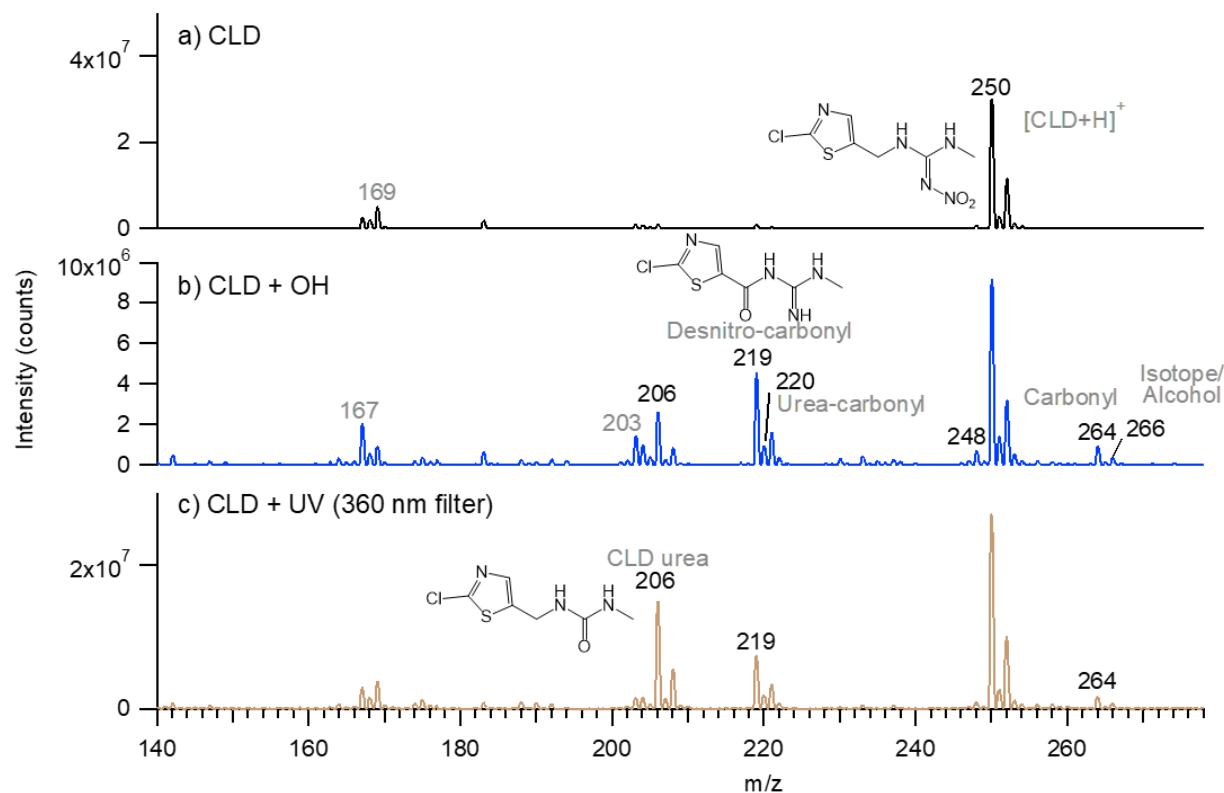


Figure 4.12: Typical DART-MS spectra of CLD samples. The top pane (a) shows CLD on ZnSe before reaction. The second pane (b) shows representative CLD spectra after 16 hours treatment with OH. The bottom pane (c) shows CLD after 19 hours of photolysis with a 360 nm optical filter. Background room air has been subtracted.

**Fig. 4.12** shows the DART spectra for CLD. The major chlorine isotope peaks from  $[CLD+H]^+$  are observed at  $m/z$  250/252. DART-MS spectra also suggest that photolysis products undergo reaction with OH simultaneously with the parent CLD, as demonstrated by the signal at  $m/z$  219/221 for the desnitro-carbonyl group and  $m/z$  220/222 for the urea-carbonyl product. While some formation of these products was also seen in photolysis-only conditions, in the OH reaction there appears to be a relatively larger contribution of the oxidized desnitro-carbonyl ( $m/z$  219) and the urea-carbonyl ( $m/z$  220) than the unoxidized urea product ( $m/z$  206) in the photolysis control. The CLD carbonyl and alcohol are also observed at  $m/z$  264 and 266 after OH reaction, but it is noted that some signal for this



species is also observed in the photolysis-only conditions as well, possibly due to known potential OH chemistry in the DART-MS source itself.<sup>129</sup> Thus, DART-MS points to a similar conclusion as the HRMS that photolysis products and those formed subsequently from their secondary reactions were more significant for CLD than for IMD and DNF.

#### 4.4.4. Summary of common products

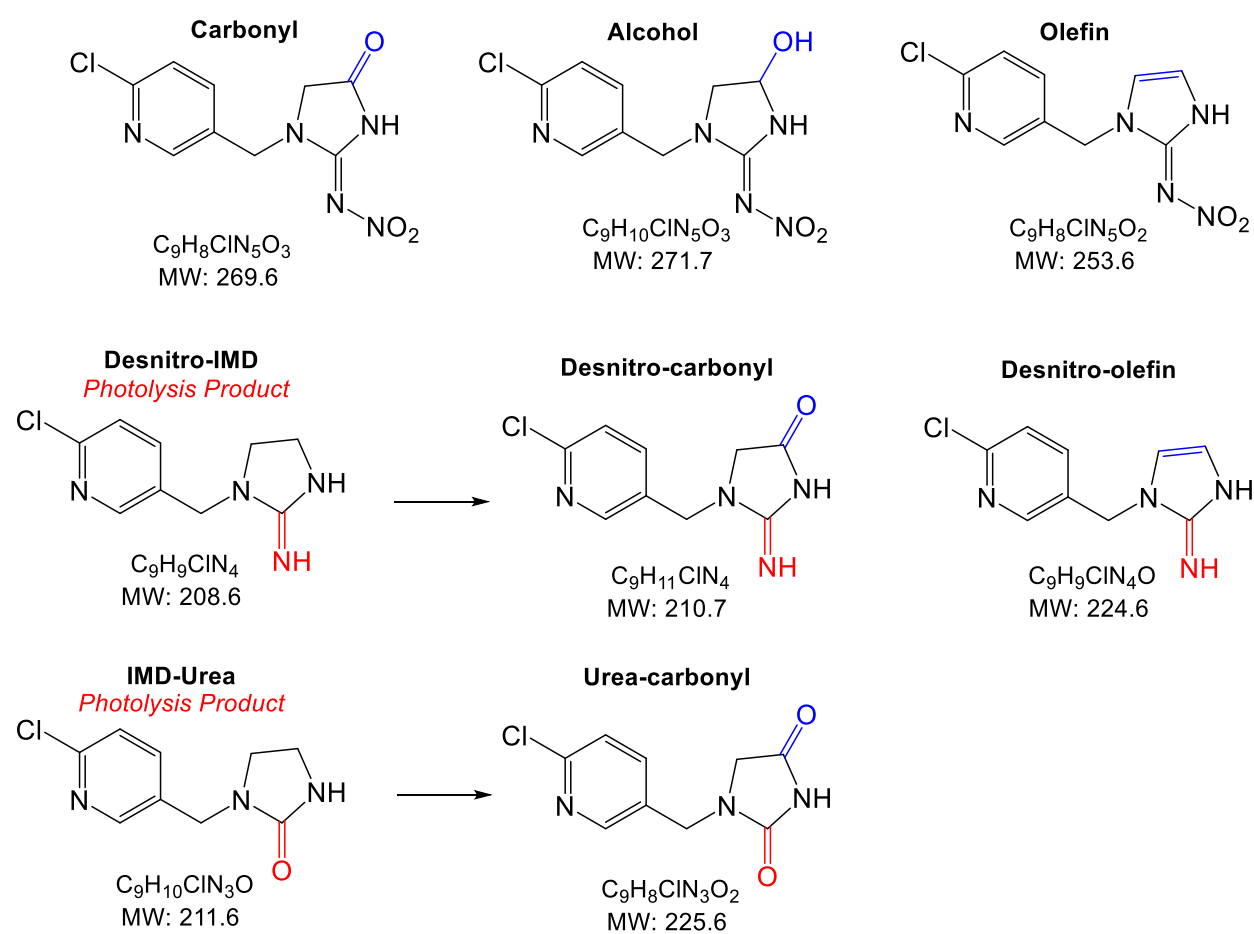


Figure 4.13: Summary of common OH reaction products observed using IMD as an example, with only one isomer shown for simplicity.

A summary of the common types of products is shown in **Fig. 4.13**, using IMD as an example. Comparison across the three structurally unique NN shows a consistent major product formation pathway. All NNs form carbonyl and alcohol products, and IMD and DNF also showed olefin products. Based on the chromatographic separation in HRMS samples, the olefin product is likely a true OH reaction product formed via dehydration of the alcohol. However, the olefin appears to have a relatively higher signal than the alcohol in the DART-MS technique, which is possibly due to the high temperature reagent gas further dehydrating the alcohol product. Additionally, secondary reactions of the desnitro and urea photolysis products leading to desnitro- and urea-oxidation products were also observed.

There is a great deal of data on these reactions in aqueous conditions that can be compared to this work for insights into differences between expected products in water versus in solids. The most commonly observed aqueous product for IMD was 6-chloronicotinic acid,<sup>60,63-65,126,128</sup> which was also observed in this work. The carbonyl product was observed in several other studies.<sup>59,60,126</sup> While additional products with multiple carbonyl or alcohol groups have been observed in the aqueous reactions,<sup>63,64,128</sup> these products were present but not prominent in this work of solid NNs (~2.5% of the signal of the single carbonyl species, **Fig. 4.14-16**). Alcohol products have also been observed in the aqueous studies.<sup>60,62,63,126,128</sup>

The urea derivative is also frequently observed in aqueous reactions,<sup>59,63,64,67,126,128</sup> and the desnitro product was observed in one other study.<sup>128</sup> However in all of these cases, there are other potential reactions occurring as well (such as photolysis, ozonolysis, and catalytic reactions) that may be forming these products. It thus seems likely that OH does not

directly attack the C=N-NO<sub>2</sub> group directly to form the urea and desnitro products, even in aqueous reactions.

Many smaller products (MW 100-157), particularly *m/z* 144,<sup>63,65-67</sup> formed from fragmentation of IMD are commonly observed in the aqueous reactions (as the goal of many of these studies in complete mineralization in a wastewater treatment-like environment), while the majority of the products observed in the solid studies presented here did not show significant fragmentation. The cage effect in the solid is likely contributing to this difference, lowering the opportunity for complete separation of the initially formed species as well as dampening out excess energy that leads to fragmentation.

To the best of our knowledge, this is the first observation of the olefin product from OH reactions, which apparently has not been reported as a product of aqueous IMD-OH reactions, although the desnitro-olefin product has been observed.<sup>59,63,128</sup> Although not previously reported in IMD-OH reactions, IMD-olefin has been widely observed as a plant metabolite and is more toxic to insects than IMD itself.<sup>130-132</sup> If the olefin is formed by dehydration of the alcohol products as proposed here, it is likely that dehydration is less likely to occur in the aqueous environment, and thus this product may only be formed in solids.

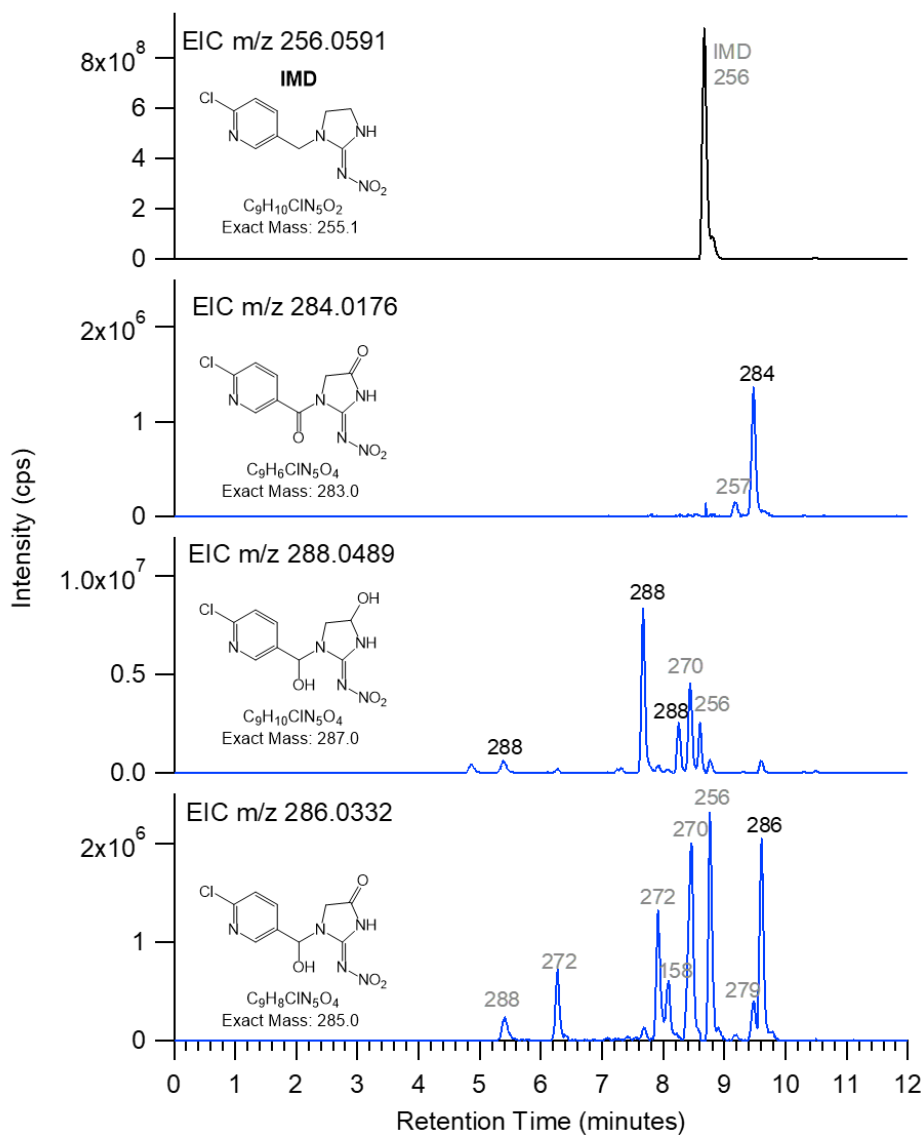


Figure 4.14: Extracted ion chromatograms (EIC) for species of interest in IMD + OH reaction. Peaks are labeled by their dominant ion, and are in grey if the ion of interest is not the dominant ion (i.e. it is occurring as a fragment of a larger signal).

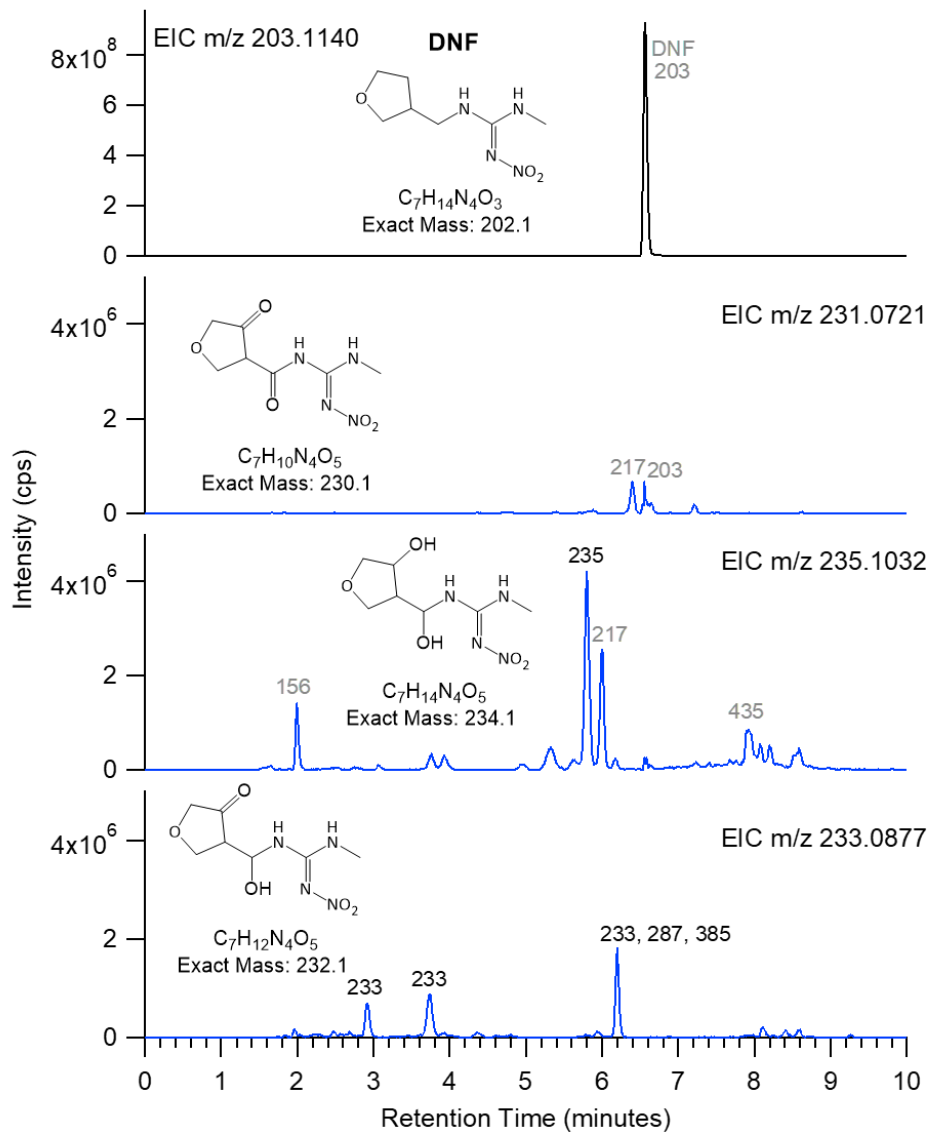


Figure 4.15: : Extracted ion chromatograms (EIC) for doubly-oxidized species in DNF + OH reaction. Peaks are labeled by their dominant ion, and are in grey if the ion of interest is not the dominant ion (i.e. the ion is a fragment of a larger signal and is not counted as an isomer identification).

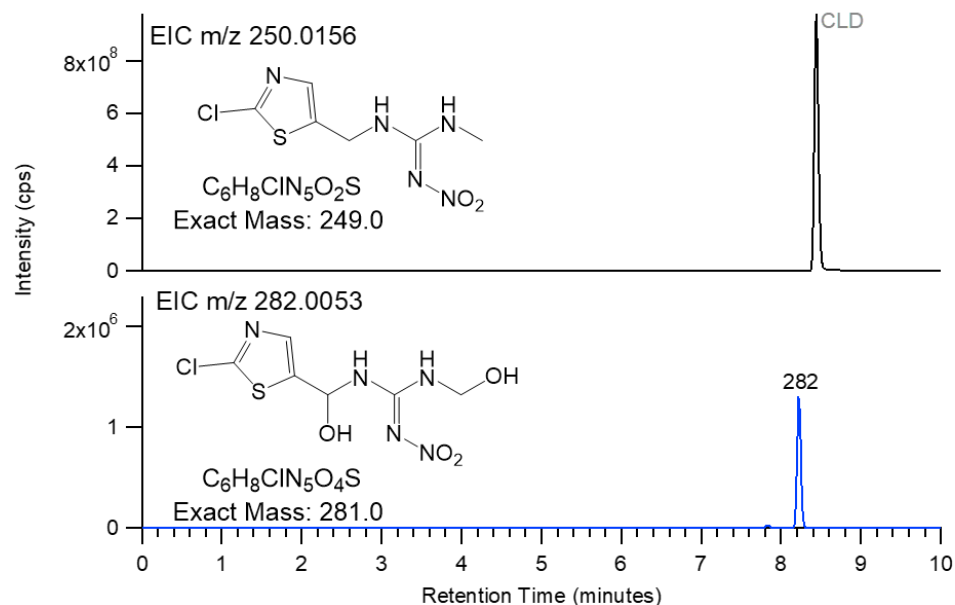


Figure 4.16: Extracted ion chromatograms (EIC) for doubly-oxidized species in CLD + OH reaction. Signals for a double carbonyl product ( $m/z$  278) and carbonyl + alcohol product ( $m/z$  279) were not observed. Peaks are labeled by their dominant ion.

## 4.5 Environmental implications

### 4.5.1. Atmospheric Lifetimes

Expected NN lifetimes with respect to the OH radical were calculated using the kinetic data obtained from FTIR results. The lifetimes were calculated using **Eqn. 4.4**:

$$\text{Lifetime } (\tau) = \frac{\# \text{ molecules on surface/cm}^2}{\text{reactions/cm}^2 \cdot s} = \frac{2 \times 10^{14} \text{ molecules/cm}^2}{\gamma \cdot [OH] \cdot \sqrt{\frac{RT}{2\pi M}}} \quad (4.4)$$

using an atmospherically-relevant OH concentration of  $10^6$  radicals  $\text{cm}^{-3}$  and the number of NN molecules  $\text{cm}^{-2}$  was estimated to be  $\sim 2 \times 10^{14}$  from structures in the Cambridge Crystallographic Data Centre library using Mercury (details in SI).<sup>133</sup> The calculated lifetimes are 102, 106, and 225 h for IMD, DNF and CLD respectively, or 5-9 days. For comparison, photolysis lifetimes determined in previous studies ranged from 11-16 hours.<sup>70,71</sup> Reaction with OH is thus expected to occur predominantly with the desnitro and urea photolysis

products during the day. However, reaction with the parent NN is expected to contribute at night, in parallel with possible nitrate radical chemistry, when photolysis is not occurring but there are dark OH sources.<sup>134</sup>

#### 4.5.2. Mechanism

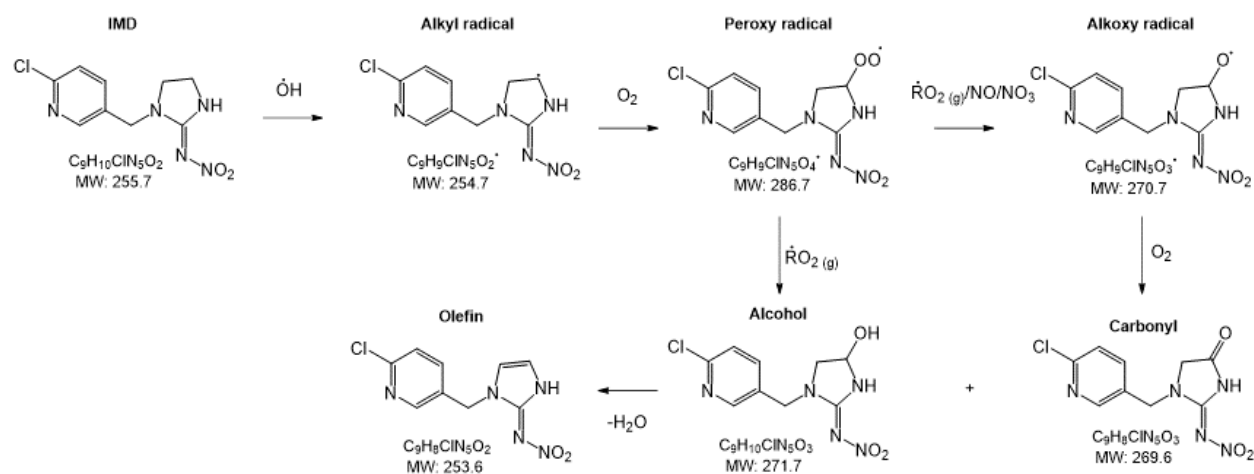


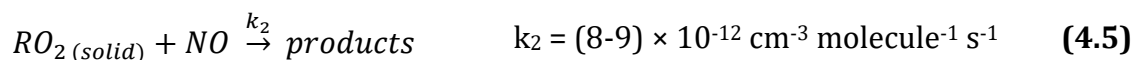
Figure 4.17: Proposed mechanism of IMD reaction with OH.

These experiments show that OH interacts with the nitroguanidines primary via hydrogen-abstraction of an aliphatic C-H<sub>x</sub> group, as shown in **Fig. 4.17**. This produces an alkyl radical which in the presence of O<sub>2</sub> forms a peroxy radical.<sup>135</sup> Due to the high concentration of RO<sub>2(g)</sub> radicals and NO in the photolyzed IPN/O<sub>2</sub> gas phase mixture, pathways are possible for the NN peroxy radical to react with RO<sub>2</sub> or NO from the gas phase to form alkoxy radicals, alcohols, and carbonyls. The alcohols are able to then form dehydrated olefin products as well in IMD and DNF. As discussed earlier, the oxidized desnitro and urea carbonyl products observed in these studies are likely due to secondary

reactions of the OH with the desnitro and urea products in reactions analogous to those in **Figure 4.17**.

This mechanism suggests that reaction of the NN peroxy radical with HO<sub>2</sub> will form hydroperoxides which cannot be detected in ESI-MS from their [M+H]<sup>+</sup> signals due to loss of water or H<sub>2</sub>O<sub>2</sub>.<sup>136</sup> The resulting ions at [M+H-H<sub>2</sub>O]<sup>+</sup> and [M+H-H<sub>2</sub>O<sub>2</sub>]<sup>+</sup> would result in similar *m/z* signals as the alcohol product and olefin product, respectively, making it difficult to obtain direct evidence of hydroperoxide product formation.

To assess the relevance of these products under environmental conditions, it is important to consider the concentration of RO<sub>2</sub> and NO radicals in the atmosphere. The NN peroxy radical intermediate (RO<sub>2 (solid)</sub>) may interact with either gas phase reactant via **reactions 4.4** or **4.5**.



In California's agriculturally-dominant San Joaquin Valley, NO concentration varies seasonally with an average of  $\sim 8.2 \times 10^8$  molecules cm<sup>-3</sup> in the summer and  $\sim 1.5 \times 10^{11}$  in the winter.<sup>137</sup> Typical RO<sub>2(g)</sub> concentrations measured at various locations around the world peak at  $\sim 5 \times 10^8$  molecules cm<sup>-3</sup> at midday.<sup>138-141</sup> Using typical rate constants for reactions 4.4 and 4.5,<sup>68</sup> first order rates are  $k_1 [RO_{2(g)}] = 5.0 \times 10^{-4} \text{ s}^{-1}$  and  $k_2 [NO] = (6.6 \times 10^{-3})$  to  $1.35 \text{ s}^{-1}$ . These estimates show that the NO reaction with RO<sub>2</sub> to form carbonyl products, of both the parent NN and the desnitro and urea photolysis products, is likely to be favored in environmentally realistic conditions.



## 4.6 Conclusions

NNs are one of the world's most commonly used pesticides and are found throughout the environment as solids on surfaces such as seeds, soil, vegetation, and blowing dust particles. Reactions of solid thin films of three NNs (IMD, DNF, and CLD) with OH radicals were studied to obtain both kinetics and product data. Reaction probabilities for the gas-solid reactions were measured using ATR-FTIR, giving estimated atmospheric lifetimes with respect to reaction with OH of 102 – 225 hours. Major products identified using UPLC-HESI-HRMS and ambient DART-MS include carbonyl-, alcohol-, and olefin containing products formed via initial hydrogen abstraction from the C-H groups. These photochemically non-reactive desnitro and urea products will continue to degrade in the environment via reaction with OH to form additional carbonyl-containing desnitro and urea products.

## CHAPTER 5: WILDFIRE INFLUENCE ON OZONE LEVELS: INSIGHTS INTO CALIFORNIA OZONE SENSITIVITY USING GROUND AND SATELLITE MEASUREMENTS

### 5.1 Introduction

Ozone pollution has been the subject of air quality control strategies for decades. While naturally occurring  $O_3$  in the stratosphere forms a protective layer from UV radiation, exposure to ground-level  $O_3$  can trigger health problems such as decreased lung function and increased pulmonary inflammation, especially in vulnerable populations such as children, the elderly, and those with pre-existing health conditions.<sup>142-144</sup> Ground-level  $O_3$  forms through peroxide radical chain reactions, which are initiated by photochemical reactions between oxides of nitrogen ( $NO_x$ ) and volatile organic compounds (VOCs).<sup>3,145</sup> The production of  $O_3$  is non-linear with respect to these  $NO_x$  and VOC precursor concentrations, as shown by the ozone isopleths (“EKMA diagrams”) in **Fig. 5.1**, and is often categorized as a  $NO_x$ -limited or VOC-limited regime. In the  $NO_x$ -limited regime, decreases in  $NO_x$  will decrease  $O_3$  concentrations, while in the VOC-limited regime, decreases in  $NO_x$  may increase  $O_3$  concentrations.

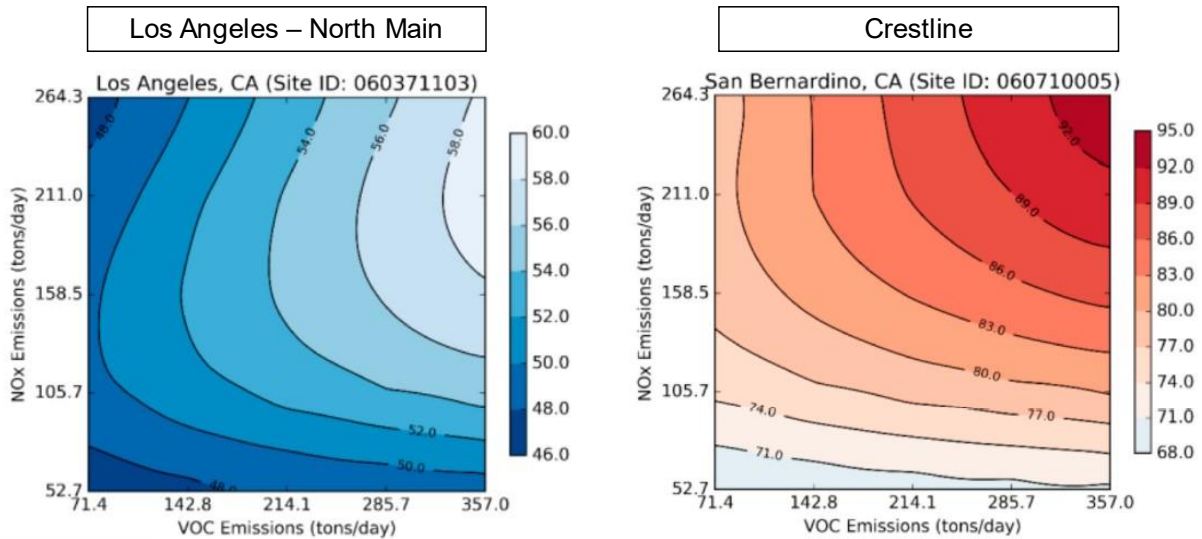


Figure 5.1 Ozone isopleths for urban (left) and rural (right) sites in the South Coast Air Basin, where the x-axis shows anthropogenic VOC emissions, and the y-axis shows anthropogenic NO<sub>x</sub> emissions at ranges of 20-100% of the projected 2030 anthropogenic emissions. The color scheme represents the ozone design values in ppb, where 70 ppb is the NAAQS attainment value. Adapted from Collet et al.<sup>146</sup>

These two regimes are the commonly used names differentiating two major photochemical pathways for O<sub>3</sub> formation from peroxy radical and NO<sub>x</sub> reactions, which are detailed in Milford et al.<sup>145</sup> In summary, reducing O<sub>3</sub> concentrations in the VOC-limited (NO<sub>x</sub>-rich) system occurs by interfering with the NO + peroxy radical reaction to favor the NO + O<sub>3</sub> reaction pathway (shown in **Fig. 5.2**) as well as the reaction of NO<sub>2</sub> and OH to form HNO<sub>3</sub>, which sequesters NO<sub>x</sub>. Reductions in NO<sub>x</sub> thus increase O<sub>3</sub> formation in this case (as shown in **Fig. 5.1**, left). In the NO<sub>x</sub>-limited (VOC rich) regime on the other hand (which is generally found in more rural areas), the VOCs are sufficiently high to produce an excess of peroxy radicals. In this case, it is the NO concentration that limits the O<sub>3</sub> generating peroxy radical-NO reaction, and reductions of NO<sub>x</sub> reduce O<sub>3</sub> formation (as shown in **Fig. 5.1**, right).

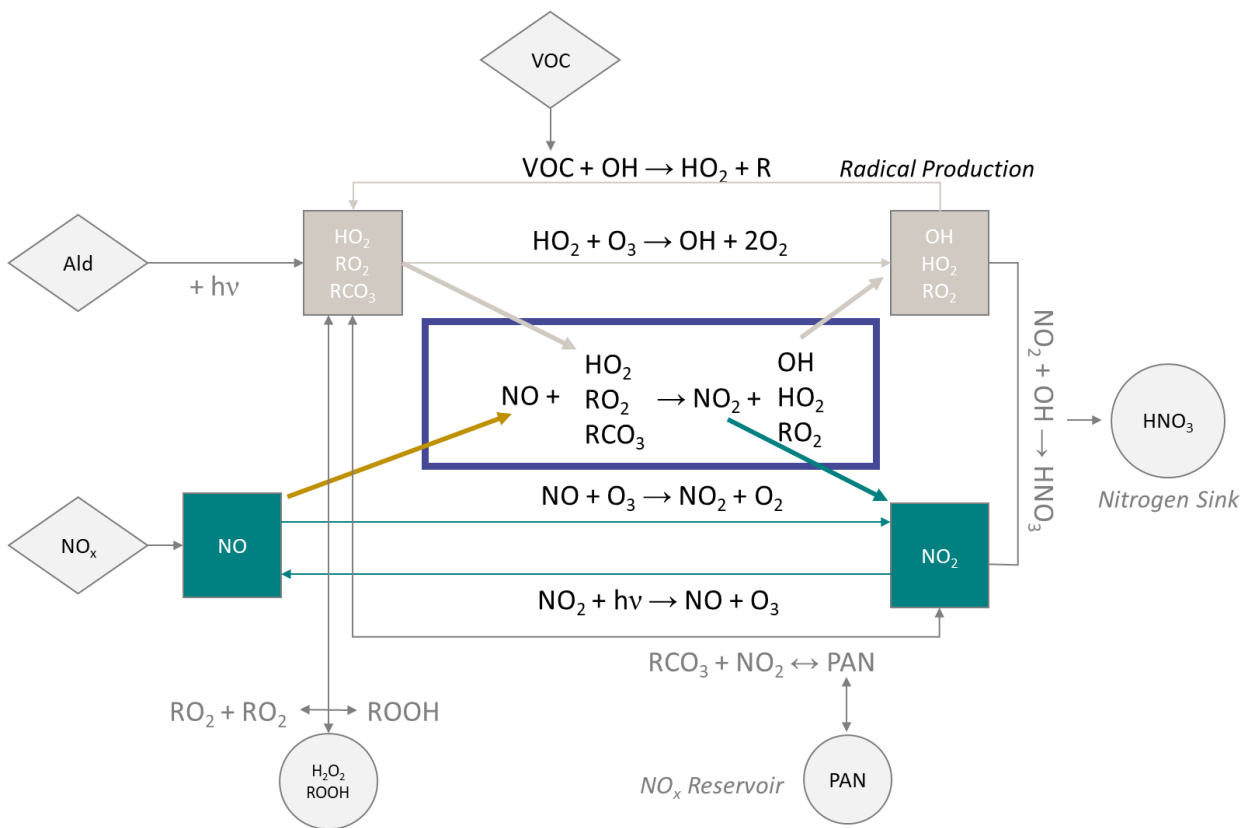


Figure 5.2 Schematic representation of the  $\text{NO}_x$  and radical reaction cycles involved in the production and consumption of ozone, adapted from Milford et al.<sup>145</sup>

Over the past five decades, California has adopted a multitude of concurrent  $\text{NO}_x$  and VOC emission control strategies to reduce ground-level  $\text{O}_3$ , with a particular focus on reducing emissions from the transportation sector.<sup>147</sup> As a result of these controls, the 8-hour  $\text{O}_3$  design value (which is defined as the 4<sup>th</sup> highest daily maximum 8-hour average (MDA8) concentration over a 3-year period) is now significantly lower in regions like the South Coast Air Basin (SoCAB), as shown in **Fig. 5.3**, despite increases in GDP, on-road passenger cars, and population.<sup>148,149</sup>

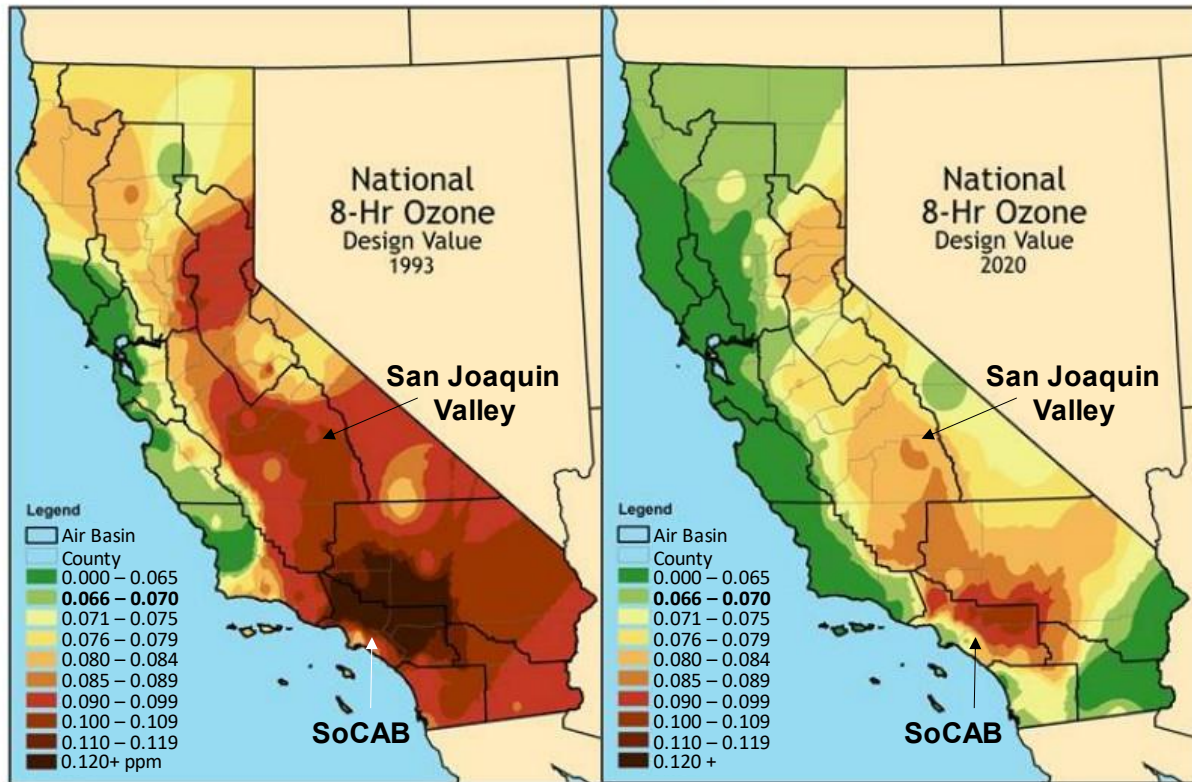


Figure 5.3 8-hour O<sub>3</sub> design value in California from 1993 to 2020, adapted from the CARB 2022 Draft SIP,<sup>149</sup> where areas in green (< 70 ppb) meet NAAQS.

Yet despite these reductions, many California air basins continue to exceed the 70 ppb 8-hour O<sub>3</sub> National Ambient Air Quality Standard (NAAQS), particularly during the warm summer months in the SoCAB and San Joaquin Valley (SJV) (Fig. 5.3).<sup>149,150</sup> California has an obligation to develop a State Implementation Plan (SIP) that would achieve compliance with NAAQS for O<sub>3</sub> in these non-attainment regions. Ozone chemical formation regimes (e.g. whether O<sub>3</sub> production is NO<sub>x</sub>- or VOC-limited) are sensitive to temperature fluctuations that affect photochemical reaction rates and can thus vary spatially and temporally.<sup>145,146,151</sup> These shifts can also occur during extreme events such as uncontrolled wildfires when large amounts of air pollutants including coarse particulate matter (PM<sub>10</sub>-

2.5), fine particulate matter (PM<sub>2.5</sub>), carbon monoxide (CO), carbon dioxide (CO<sub>2</sub>), VOCs, and NO<sub>x</sub> are released into the atmosphere.<sup>152</sup> The current emission reduction and air pollution mitigation strategies laid out in the California SIP are expected to guide the state toward O<sub>3</sub> NAAQS attainment by 2037 but do not account for the impact of increasing frequency and intensity of California's wildfires that also affect ground-level O<sub>3</sub> production. With growing importance of climate change (e.g., frequent and intense wildfire events, higher peak temperatures),<sup>153</sup> evaluating the current atmospheric O<sub>3</sub> sensitivity to NO<sub>x</sub> and VOCs during the wildfire season is imperative to ensure future O<sub>3</sub> reduction strategies are effective.

The impact of wildfires on O<sub>3</sub> levels is difficult to predict, as the emissions from these plumes can either increase or decrease ambient O<sub>3</sub> production. For example, PM emissions can obscure light to reduce O<sub>3</sub>-generating photochemical reactions, react heterogeneously with O<sub>3</sub>, or nudge atmospheric chemical composition towards those less favorable for O<sub>3</sub> production.<sup>154</sup> Ozone precursor emissions within a wildfire plume, on the other hand, can contribute to O<sub>3</sub> formation, and studies in Colorado, Idaho, and other Western states have observed increases in O<sub>3</sub> ranging from 1 to 20 ppb.<sup>155-158</sup> Additionally, although satellite instruments like Moderate Resolution Imaging Spectroradiometer (MODIS) on-board Terra and Aqua Earth observing satellites are being used to detect and study active fires, direct and residual fire influence on ground-level air quality and atmospheric chemical regimes are difficult to determine quantitatively.<sup>154</sup> This poses additional challenges in understanding the root causes of 8-hour O<sub>3</sub> NAAQS exceedances during the warm summer months. Robust identification of wildfire-influenced days while simultaneously observing

changes in O<sub>3</sub> chemical regimes and MDA8 O<sub>3</sub> levels will help determine whether additional emission control measures are needed to offset the influence of future wildfires.

## **5.2 Research Goals**

This study investigated the impact of wildfires on O<sub>3</sub> levels and formation regimes using ground and satellite observations in California. We applied a threshold exceedance determination (TED) method, which binned days of extreme air pollution events by level of statistical anomalies in ground-level air quality monitoring data. This included two statistical methods on 2018, 2019, and 2020 ground-level PM<sub>10</sub>, PM<sub>2.5</sub>, and CO measurements collected at 17 air monitoring sites across California to differentiate extreme air pollution event days (which are likely associated with wildfires, prescribed fires, or agricultural burning). Monthly aggregated data were then statistically evaluated to determine whether these extreme air pollution event days were associated with greater probability of 8-hour O<sub>3</sub> NAAQS exceedances.

Additionally, tropospheric column integrated formaldehyde (HCHO) and nitrogen dioxide (NO<sub>2</sub>) data from TROPospheric Monitoring Instrument (TROPOMI) on-board the Sentinel-5 Precursor (S5P) satellite were used as surrogates to study the simultaneous O<sub>3</sub>-NO<sub>x</sub>-VOC sensitivities relative to the ground-level air monitoring data. These results provide new insight into the 8-hour O<sub>3</sub> NAAQS exceedances during California fires and therefore precursor emission policy goals across the state.

## **5.3 Methods**

### **5.3.1. Ground-Level Air Quality Monitoring Data**

Ground-level air quality data from 17 California air quality monitoring sites from 2018 – 2020 were obtained from the U.S. Environmental Protection Agency (EPA) Air Quality

System (AQS).<sup>159</sup> The AQS provides access to ambient air quality data collected at outdoor ground-level monitors from state, local and tribal monitoring agencies across the United States. The data obtained included ground-level daily mean PM<sub>10</sub> concentration, daily mean PM<sub>2.5</sub> concentration, daily maximum 8-hour average (MDA8) CO concentration, and MDA8 O<sub>3</sub> concentration. Ground-level air quality data for the most recent time period (November and December 2020) was not yet available in the EPA AQS, and was therefore gathered from the California Air Resources Board (CARB) Air Quality Data Query Tool,<sup>137</sup> using the Air Quality and Meteorological Information System (AQMIS). AQMIS provides real-time, preliminary data and is subject to change.

This study focused on the SJV and SoCAB due to their continued O<sub>3</sub> exceedances, but also included sites in the Sacramento Valley Air Basin to enable comparison of observations with a recent ground-level O<sub>3</sub> sensitivity study that used daily measurements of ambient air samples in Sacramento.<sup>160</sup> Only air quality monitoring sites within these three air basins that monitored for all pollutants of interest (PM<sub>10</sub>, PM<sub>2.5</sub>, CO, and O<sub>3</sub>) were used in this study. This selection process resulted in 17 monitoring sites across the three air basins, and their locations are displayed in **Fig. 5.4**. Of the sites, four were in the SJV, 11 in the SoCAB, and two in the Sacramento Valley. In most cases, data were reported daily with occasional intermittent gaps in data (details on data collection frequency by site are included in **Table 5.1**).



Table 5.1: Ground-monitor site locations

Air Basin	County	Site Name <sup>a</sup>	Latitude	Longitude
Sacramento Valley	Butte	Chico-East Avenue	39.76168	-121.84
Sacramento Valley	Sacramento	Sacramento-Del Paso Manor	38.61378	-121.368
San Joaquin Valley	Fresno	Clovis-Villa	36.81945	-119.716
San Joaquin Valley	Fresno	Fresno - Garland	36.78538	-119.773
San Joaquin Valley	Stanislaus	Modesto-14th Street	37.64217	-120.994
San Joaquin Valley	San Joaquin	Stockton-Hazelton	37.95074	-121.269
South Coast	Orange	Anaheim	33.83062	-117.938
South Coast	Los Angeles	Glendora	34.14435	-117.85
South Coast	Riverside	Lake Elsinore	33.67649	-117.331
South Coast	Los Angeles	Los Angeles-North Main Street	34.06659	-118.227
South Coast	Riverside	Mira Loma (Van Buren)	33.99636	-117.492
South Coast	Riverside	Palm Springs	33.85275	-116.541
South Coast	Riverside	Rubidoux	33.99958	-117.416
South Coast	San Bernardino	San Bernardino	34.10668	-117.274
South Coast	Los Angeles	Santa Clarita	34.38344	-118.528
South Coast	San Bernardino	Upland	34.10374	-117.629
South Coast	San Bernardino	Victorville-Park Avenue	34.51096	-117.326

<sup>a</sup> Sites in red have intermittent PM<sub>10</sub> data. These sites were evaluated by the TED method using PM<sub>2.5</sub> and CO thresholds, and PM<sub>10</sub> data was then qualitatively used to confirm fire influence. No difference in the trends were observed when sites with intermittent PM<sub>10</sub> data were removed.

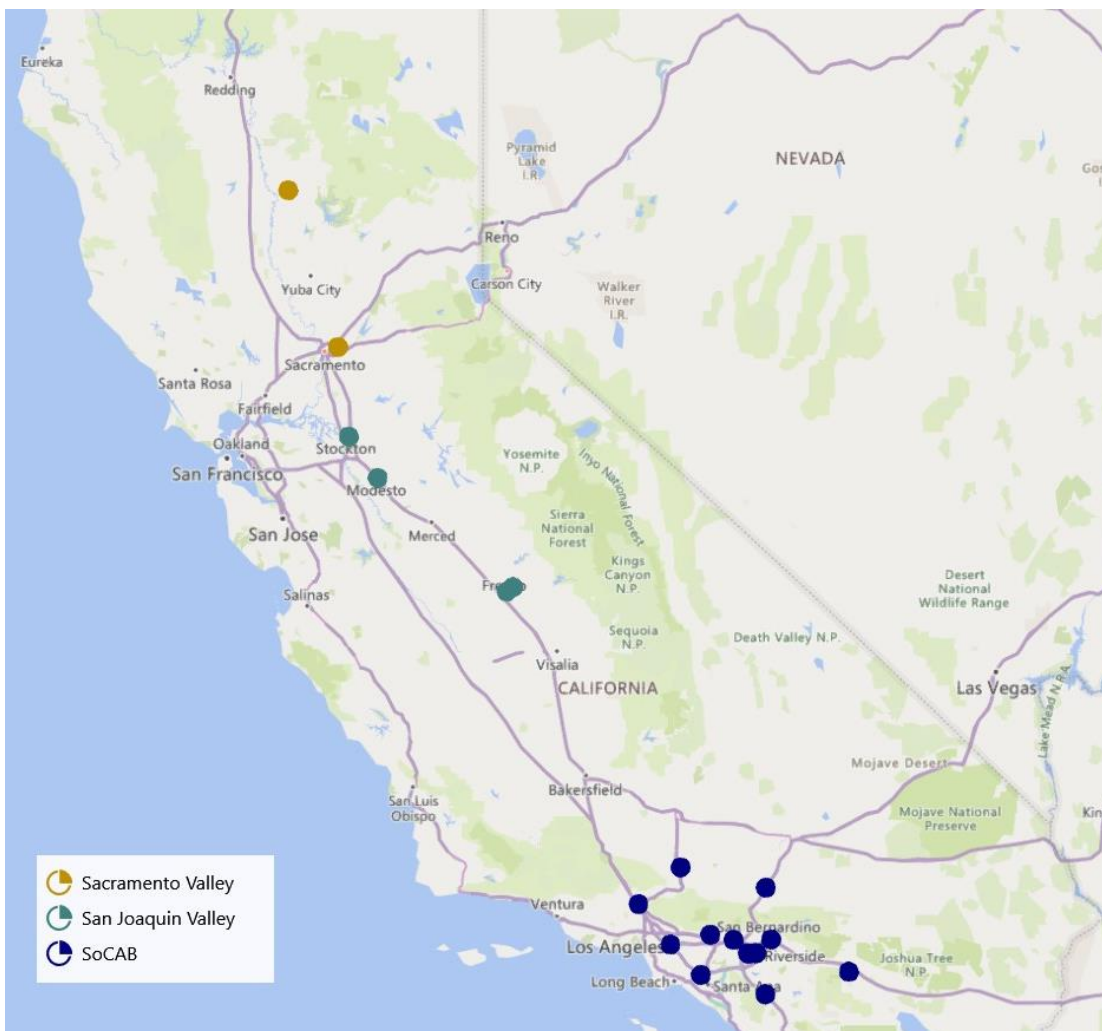


Figure 5.4: Map of ground monitor locations.

### 5.3.2. TROPOMI Satellite Data for O<sub>3</sub>-NO<sub>x</sub>-VOC sensitivity

Daily tropospheric column integrated TROPOMI NO<sub>2</sub> and HCHO levels (Unit: mol/m<sup>2</sup>) as surrogates for ground-level NO<sub>x</sub> and VOC concentrations, respectively, were extracted from NASA Earthdata<sup>161</sup> for May 2018 to December 2020.<sup>162</sup> We retained TROPOMI NO<sub>2</sub> and HCHO data with quality assurance (QA) values  $\geq 0.5$  for further analyses.<sup>163</sup> R (version 4.0.4) was then used to calculate the monthly average TROPOMI NO<sub>2</sub> and HCHO tropospheric vertical column densities for 0.1° (11 km × 11 km) grid cells centered at each of the ground

air monitoring sites. Using this radius enabled the detection of 1-7 measurements per site per day, with a mean of 3.1 HCHO and 3.2 NO<sub>2</sub> measurements per site per day that were then averaged across the entire month. The coefficient of variation (standard deviation divided by mean value) of the sites within the grid cell was 0.56 for NO<sub>2</sub> and 0.80 for HCHO. TROPOMI occasionally records negative data values when levels are exceptionally low due to low sensitivity at those levels. These negative values are still meaningful because they represent very low HCHO or NO<sub>2</sub> levels and removing them will cause overestimation bias. Thus for this study negative values were replaced with the non-negative 2018 – 2020 minimum value in the month of interest.

### **5.3.3. Threshold Exceedance Determination (TED)**

Fires emit large amounts of both particles and gas-phase emissions. The plumes contain a compositionally complex mixture of particles including ash, PM<sub>10</sub>, and PM<sub>2.5</sub>, and gaseous species such as CO, CO<sub>2</sub>, and the ozone precursors NO<sub>x</sub> and VOCs.<sup>154,164</sup> Evidence of wildfire influence in air samples can thus appear in ambient measurements of PM<sub>10</sub>, PM<sub>2.5</sub>, and CO, which are measured throughout California's air quality monitoring sites. In this work, the ground-level air quality monitoring data was used to bin days of extreme air pollution events by level of statistical anomalies in these tracer levels using a threshold exceedance determination (TED) method. Threshold exceedance criteria were developed for select pollutants (PM<sub>10</sub>, PM<sub>2.5</sub>, and CO) which were chosen based on their association with wildfire emissions and observed sensitivity to reported fires occurring in the same county as the monitors (**Fig. 5.5**).

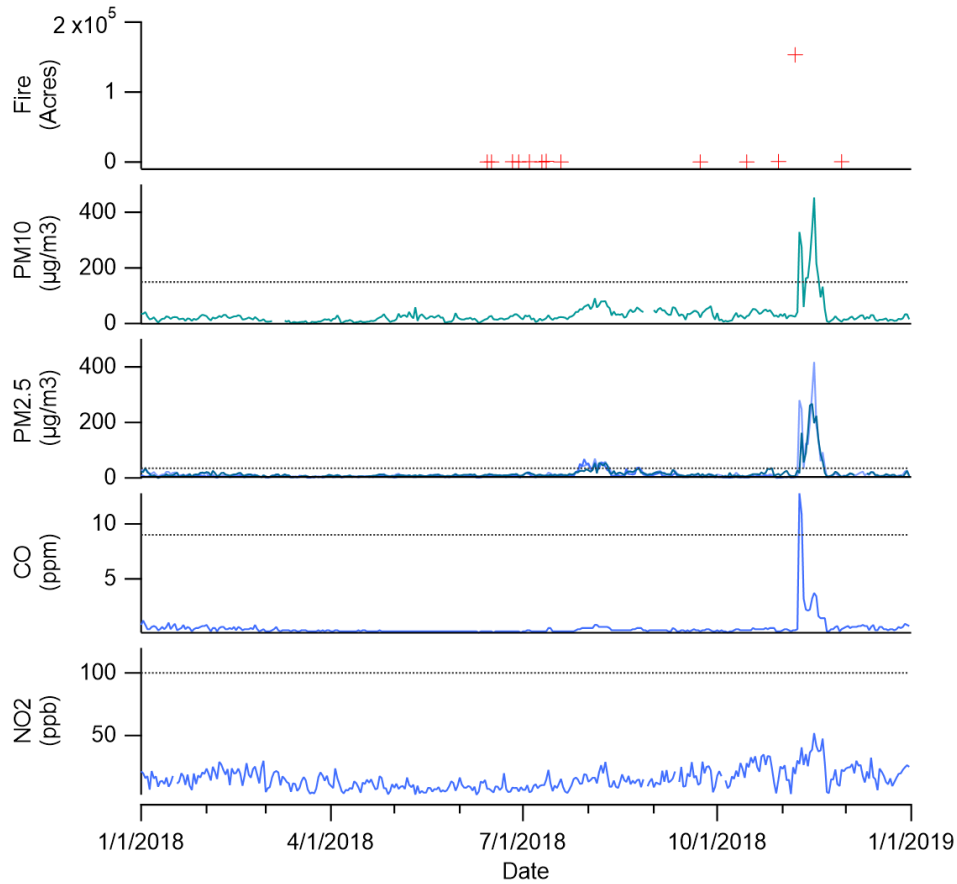


Figure 5.5 Ground-level air quality data in Butte County compared to reported wildfires<sup>165</sup> in Butte County.

The threshold criteria were developed to bin extreme air pollution days and are summarized in **Table 5.2**. Initial threshold values (“base case”) were derived from values that binned roughly 10% of days as extreme air pollution event days and visually matched observed peaks in the indicator species. The threshold values were further refined to evaluate the sensitivity of these criteria. Sensitivity tests showed that the ability to bin days between control days and extreme air pollution event days was not overly sensitive to small changes in the criteria thresholds.

The first criterion was a numerical threshold, a condition in which the daily average air pollutant levels must be greater than  $2 \times 15$ -day minimum, with the 15-day period centered on the

day of interest. The second criterion was a statistical threshold, where the first threshold must be met and the rising slope over a 7-day period (centered on the day of interest) must be greater than  $3 \mu\text{g}/\text{m}^3$  per day (for  $\text{PM}_{10}$  and  $\text{PM}_{2.5}$ ) or 20 ppb per day (for CO). Falling slopes must also satisfy the same criteria.

Table 5.2: Threshold exceedance value (TED) method summary for wildfire influence summary

	Numerical Threshold	Statistical Threshold
<b>Tier 1</b> (Control)	None	None
<b>Tier 2</b> (Extreme air pollution event)	$> 2 \times$ minimum 15-day windows	Slope ( $\text{PM}_{2.5}$ and $\text{PM}_{10}$ ) $> 3 \mu\text{g}/\text{m}^3/\text{day}$ Slope (CO) $> 20$ ppb/day 7-day windows
<b>Tier 3</b> (NAAQS exceedance days)	$\text{PM}_{10} > 150 \mu\text{g}/\text{m}^3$ $\text{PM}_{2.5} > 35 \mu\text{g}/\text{m}^3$ CO $> 9$ ppm	N/A

Days were then binned as tier 1, 2, or 3, where tier 1 are control days (no atypical pollution events). Tier 2 days are considered extreme air pollution event days (likely associated with extreme air pollution events such as wildfires, prescribed fires, or agricultural burning) that met both criteria for all three air pollutants of interest. If a gap of two or less days between tier 2 days existed, a filter was added to reclassify the days in between as also tier 2 days. Tier 3 days are air pollution exceedance days with at least one of the criteria pollutants exceeding the NAAQS threshold, but the TED method was not met for all three species. The tier 3 days are of interest because there is a NAAQS exceedance occurring, and removing them from the tier 1 group helps better differentiate trends related solely to high pollution levels, but since they are unlikely associated with wildfires they are not the focus of the present study.

## 5.4 Identification of fire-influenced days

Fig. 5.5 shows an example visual output of the TED method applied to the 2020 air quality data reported at the Modesto-14<sup>th</sup> Street site, which is an air quality monitoring site located in the SJV.

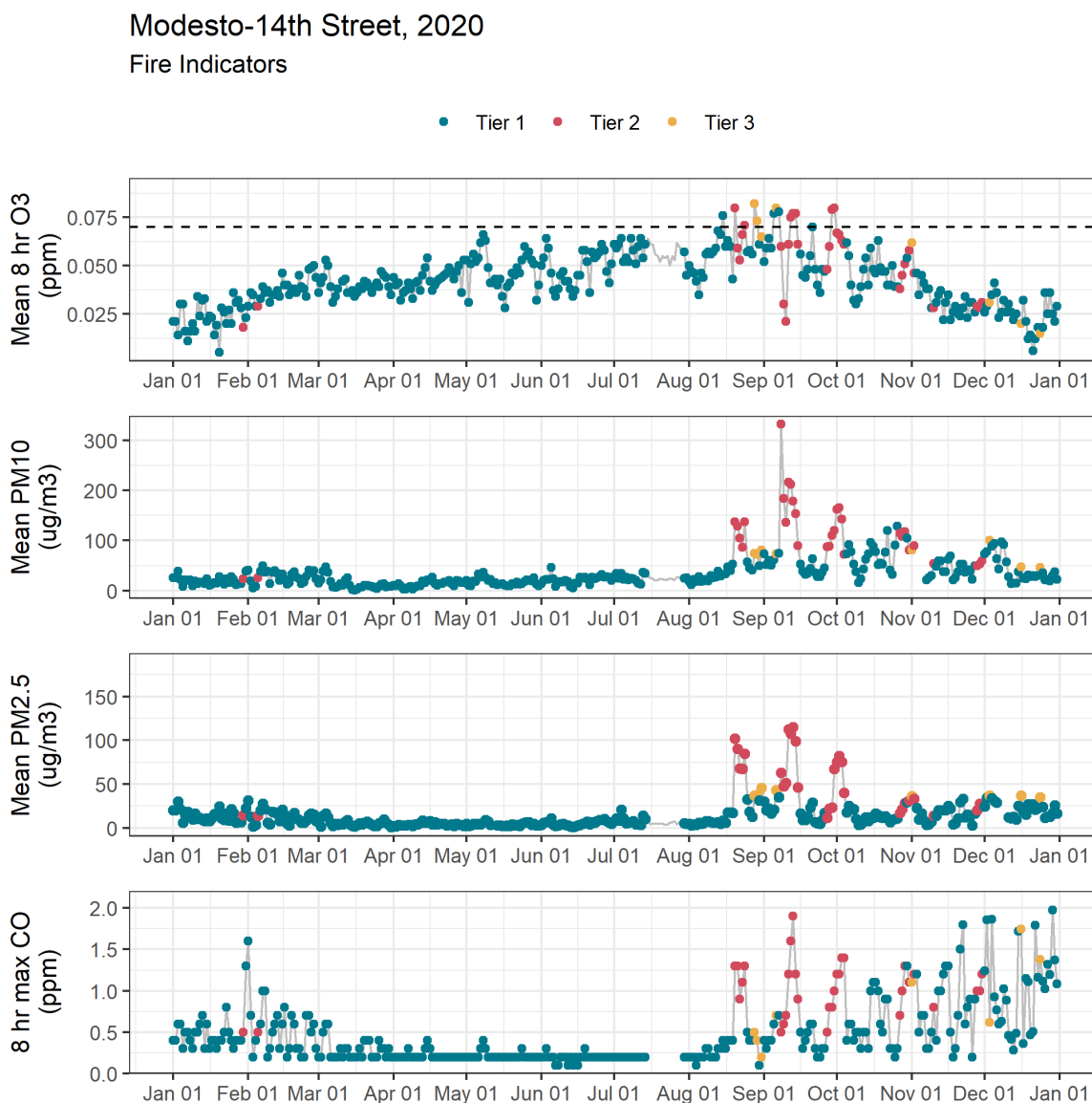


Figure 5.6: Example of ground monitor data retrieved for each site. Colors show differentiation of days between tiers, where Tier 1 (teal) are control days, Tier 2 (red) are extreme air pollution event days, and Tier 3 (yellow) are NAAQS exceedance days that did not meet criteria for Tier 2. The tiers are determined by the TED method described in the methods section, based on values of  $PM_{10}$ ,  $PM_{2.5}$ , and CO.  $O_3$  data is also shown in the top pane, but was not used in the binning process. The dashed line in the  $O_3$  pane is the 8-hour  $O_3$  NAAQS of 70 ppb.

The distribution of identified days is summarized in **Fig. 5.6**. The TED method identified 267 total tier 2 (extreme air pollution event days) in the SJV air basin across four monitors, or an average of 67 days identified per monitor from 2018 – 2020. In the SoCAB, an average of 21 days per monitor from 2018 – 2020 were identified (226 total tier 2 indicated across 11 monitors), and in Sacramento Valley an average of 51 days per monitor from 2018 – 2020 were identified (102 total tier 2 days across two monitors). Thus, amongst the three air basins SJV saw the highest average number of fire-influenced days and SoCAB saw the lowest.

## Tier 2 (extreme air pollution event) Indications

Air Basin:  Sacramento Valley  SJV  SoCAB

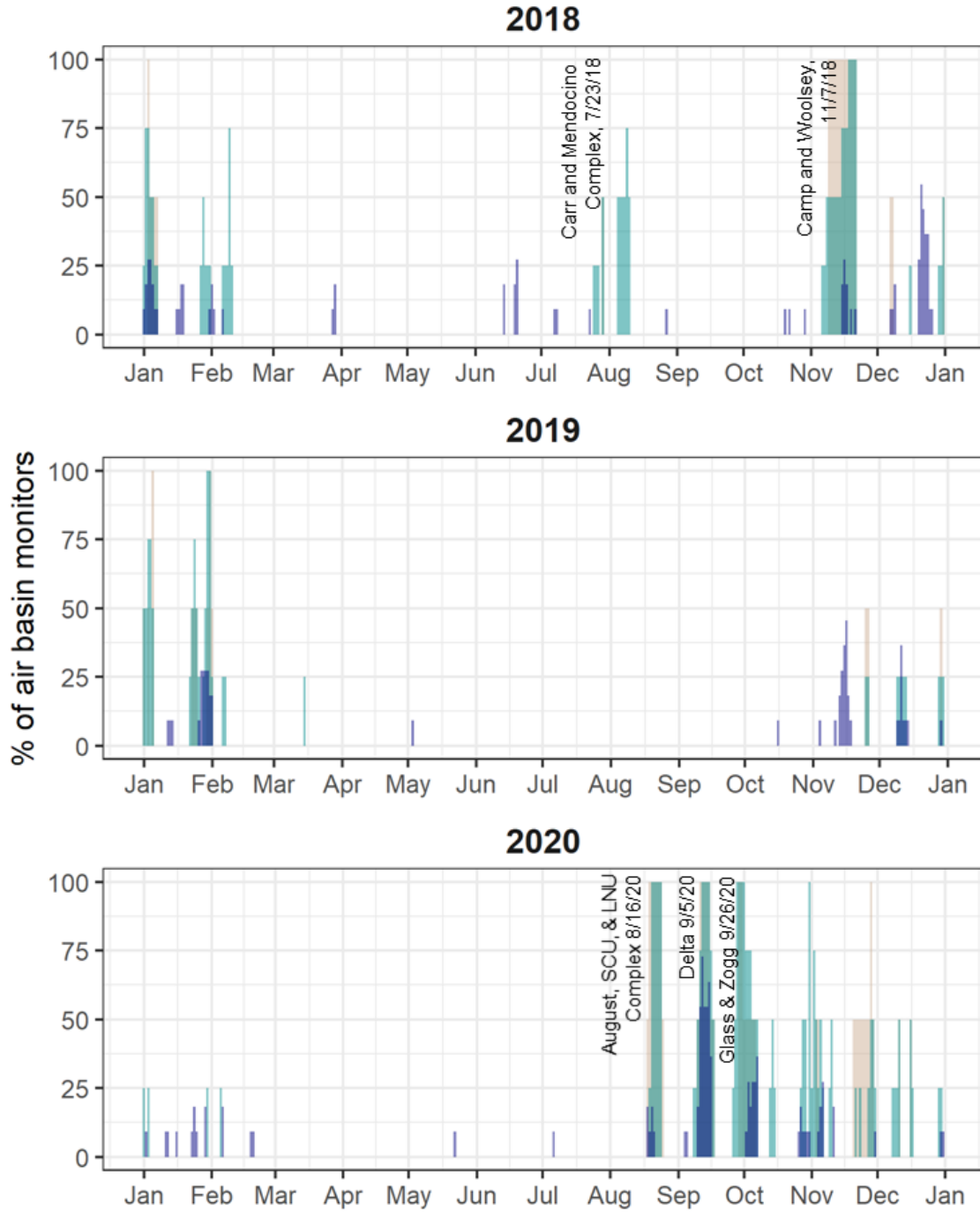


Figure 5.7: Histogram of identifications of tier 2 days, normalized to the normal of monitors in each air basin. Reported CAL FIRE<sup>165</sup> begin dates correlating with large identification peaks are also marked



CAL FIRE Incident Database<sup>165</sup> and CARB's Prescribed Fire Information Reporting System (PFIRS) were used to corroborate the outputs of the TED method based on the reported start days and acres burned for fires that occurred in California. However, not all identified tier 2 days are expected to be purely from wildfires, and not all wildfires near a site are expected to be detected by the method. The effects of poor vertical mixing of the fire plumes, residual wildfire smoke from smoldering conditions, residential burning, and other unreported intentional and non-intentional burning are expected to impact the regional air quality and are difficult to pinpoint due to lack of data. For example, some days flagged by the TED method in January and February (outside of the typical wildfire season) aligned with prescribed burning reported in the area<sup>166</sup> (**Fig 5.8**), which peaks in January – February, as well as aligning with detections of burned area from the MODIS Terra/Aqua burned area product.<sup>167</sup>

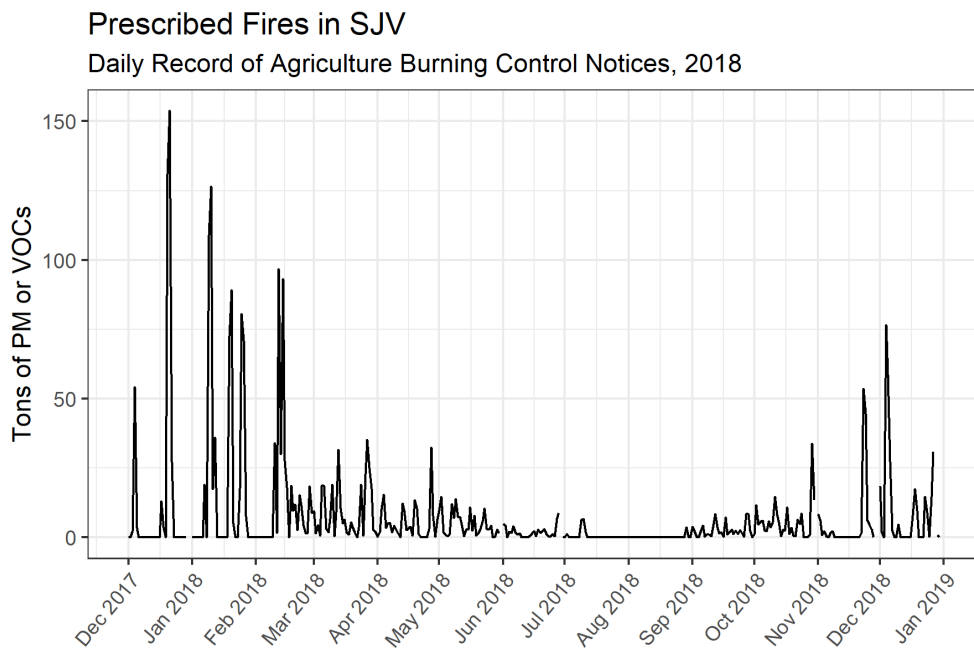


Figure 5.8 Tons of PM or VOCs reported in agricultural burn notices in 2018 in San Joaquin Valley.<sup>166</sup>

Satellite remote sensing techniques such as MODIS, however, often struggle to detect smaller fires and have been reported to miss a larger portion of prescribed fires compared to wildfires (which are often intentionally set to burn at lower intensities).<sup>154</sup> In these instances, the TED method described herein may identify anomalously polluted air samples near the surface not observed in other data sources.

Days flagged by TED method are currently being further evaluated by pairing the reported data with NOAA Hazard Mapping System (HMS).<sup>168</sup> The HMS provides daily estimates based on visible wavelength of low, medium, or high smoke concentrations transported over air quality monitoring sites. The satellite-based HMS system is subject to both positive and negative biases that may result in different identifications from the ground-based TED method. For example, the HMS may overestimate some wildfire-affected days detected as the satellite retrieves the entire integrated air column, and smoke plumes may be moving above the ground-level air mass. Additionally, the HMS can also undercount the number of days compared to the TED method due to interference from clouds.

### **5.5 Seasonal Shifts in TROPOMI HCHO/NO<sub>2</sub> ratios**

With days binned between tier 1 (control days), tier 2 (extreme air pollution exceedance days), and tier 3 (NAAQS exceedance only days), insights into O<sub>3</sub>-VOC-NO<sub>x</sub> sensitivity trends via TROPOMI HCHO/NO<sub>2</sub> ratios were investigated. **Figure 5.9** shows the TROPOMI HCHO/NO<sub>2</sub> ratio statistics averaged for all air quality monitoring sites in each air basin aggregated by month from 2018-2020 as box and whisker plots, where median values are bars across the box. Statistical significance of tier 2 and tier 3 day averages compared to tier 1 days are calculated using Wilcoxon tests, and groups with no \* are not statistically different.

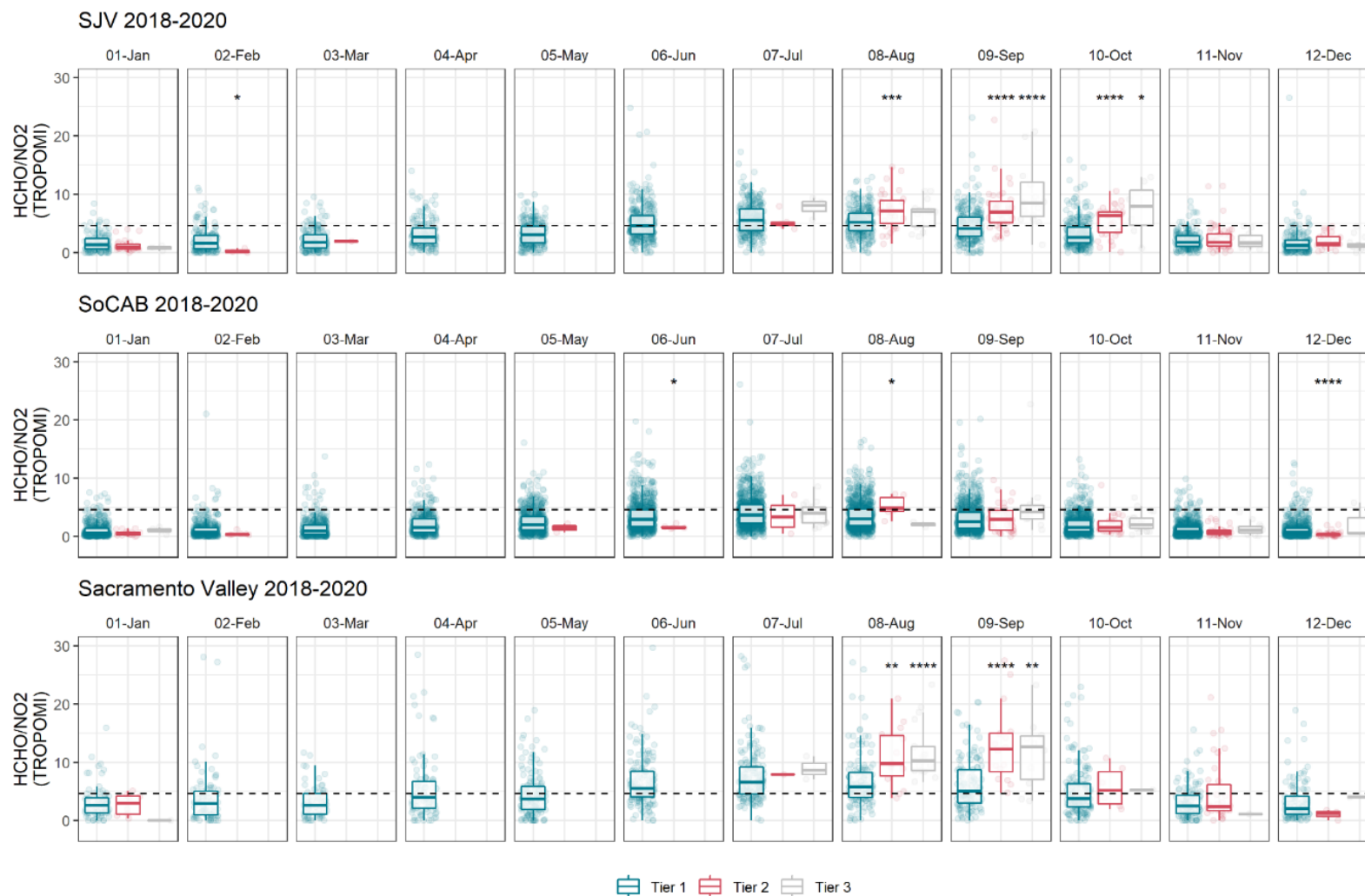


Figure 5.9: Visualization of TROPOMI HCHO/NO<sub>2</sub> values in each air basin aggregated by month from 2018-2020. Median values are bars across box, the top and bottom of boxes indicate the 75<sup>th</sup> and 25<sup>th</sup> percentiles, and whiskers show 90<sup>th</sup> and 10<sup>th</sup> percentiles. Outlier points have been hidden from the box-and-whiskers display, and instead individual data points are shown behind box plots. Statistical significance of tier 2 and tier 3 days compared to tier 1 days are calculated using Wilcoxon tests, where \* represents statistical significance (\* is  $p < 0.05$ , \*\* is  $p < 0.01$ , \*\*\* is  $p < 0.001$ , and \*\*\*\* is  $p < 0.0001$ ) and groups with no \* are not statistically different.

The TROPOMI HCHO/NO<sub>2</sub> ratio is plotted on the vertical axis of this figure. A lower ratio indicates a more VOC-limited regime (NO<sub>x</sub>-rich), while higher ratios indicate a more NO<sub>x</sub>-limited regime (VOC-rich). An approximate transition point (4.6) between the two regimes is indicated by the dashed line. The true transition point in actuality is broader than a single point,<sup>169,170</sup> can vary across the urban-to-rural gradient,<sup>145,146,169</sup> and likely varies somewhat across the three air basins. We thus cannot conclude with certainty that values near this transition point in the respective NO<sub>x</sub> or VOC-limited regimes. The transition point chosen for this visual aid is based on values reported in Jin et al.<sup>169</sup> and Wu et al.<sup>160</sup> The study by Jin et al.<sup>169</sup> based their transition point values on modeling using OMI satellite observations and ground-level O<sub>3</sub> measurements across seven U.S. cities. Los Angeles reported the highest transition point (4.5 ± 1.8) compared to the mean transition point across these seven cities which was 3.6 ± 0.2 (2σ).<sup>169</sup> More recently, field studies by Wu et al.<sup>160</sup> reported a similar transition point in Sacramento of 4.6 (95% confidence interval: 4.39 – 5.90) by pairing field chamber studies of ambient air samples that measured the effect of NO<sub>x</sub> and VOC perturbation on O<sub>3</sub> production with TROPOMI observations.

Setting aside the tier 2 and 3 days momentarily, a clear, seasonal trend in the TROPOMI HCHO/NO<sub>2</sub> ratio was observed in the tier 1 days (control group, blue in **Fig. 5.9**). This trend shows the ratio was highest in the summer and lowest in the winter and was observed across all three air basins. The Sacramento Valley presented the highest ratios (most NO<sub>x</sub>-limited), while SoCAB had both the lowest values (most VOC-limited) and the narrowest range of values throughout the year. In the SJV and Sacramento Valley, a transition across the VOC-limited side of the transition point (TROPOMI HCHO/NO<sub>2</sub> < 4.6) in the winter towards the

NO<sub>x</sub>-limited side (TROPOMI HCHO/NO<sub>2</sub> > 4.6) in the summer is observed, while the median SoCAB value remains on the VOC-limited side throughout the year.

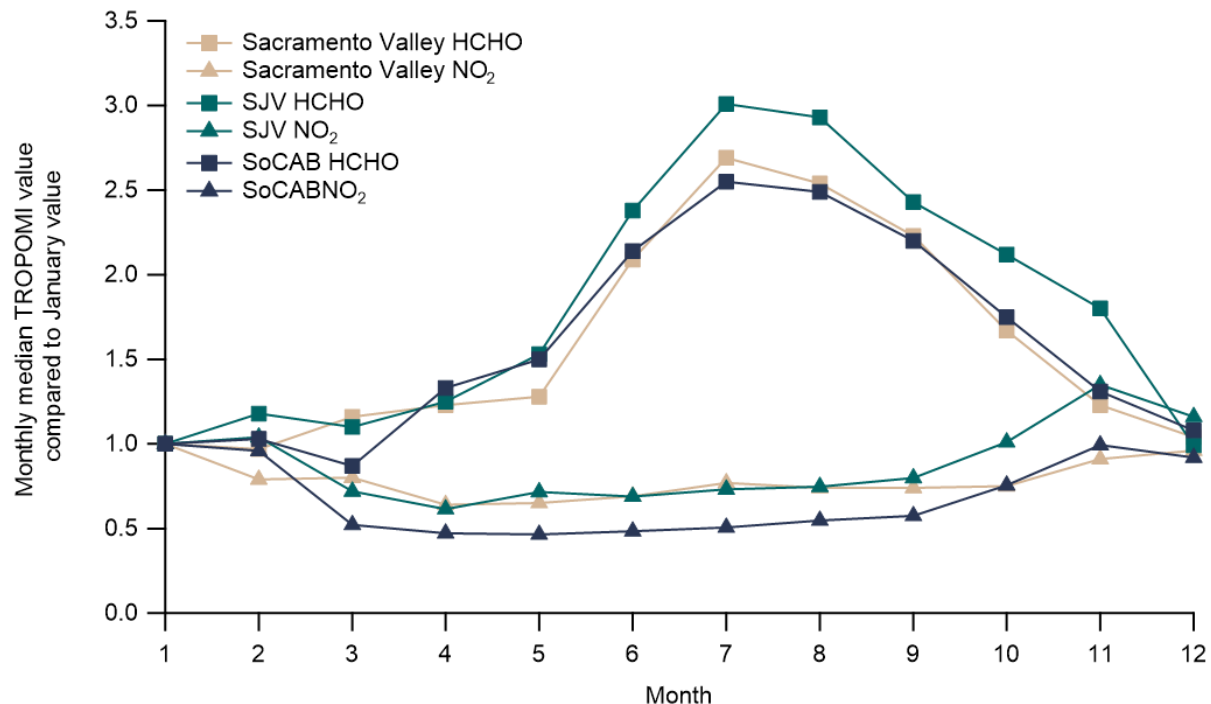


Figure 5.10: Median monthly TROPOMI HCHO and NO<sub>2</sub> values compared to their January values, highlighting an increase in HCHO values in the summer months.

Analysis of the magnitude of TROPOMI HCHO and NO<sub>2</sub> fluxes showed that the increased ratios in the summers were mainly driven by increasing HCHO concentrations (**Fig. 5.10**). NO<sub>2</sub> concentrations decrease in summer as expected from photochemistry but remained relatively more constant throughout the year than HCHO. HCHO has numerous primary sources, including direct emissions of HCHO from vehicle emissions, solvent-use, and off-gassing from building materials. Secondary sources of HCHO though are generally more dominant than direct emissions,<sup>68,171-174</sup> and occur via photochemical oxidation from numerous VOCs.<sup>68,171</sup> With secondary photochemical formation of HCHO, the dominant HCHO precursor can vary spatially and temporally and include both biogenic and

anthropogenic VOCs. For example, the main HCHO source has been reported to be oxidation of biogenic VOCs in the Southeastern U.S. and Texas,<sup>172,173</sup> but higher contributions from urban vehicle emissions have been reported in Hong Kong.<sup>174</sup> Thus, although the cause of the increase in California is not immediately clear without a dedicated source apportionment effort, we predict the seasonal shift in HCHO/NO<sub>2</sub> values in the air basins in the summer to be due to an increase in photooxidation of biogenic VOCs. This is in agreement with both the known dependence of biogenic emissions on temperature,<sup>175</sup> an increase in photolytic activity during the summer (i.e., longer, sunnier days), and the geospatial trend of HCHO increases in vegetation-rich areas observed by Wu et al.<sup>160</sup> The result is that while the air basins may be firmly in the VOC-limited regimes in the winter, the summer influx in HCHO results in an increased TROPOMI HCHO/NO<sub>2</sub> ratio, pushing the ratio near the predicted transition range, where O<sub>3</sub> production is most efficient.

#### **5.5.1. HCHO/NO<sub>2</sub> ratios on tier 2 days**

An increase in TROPOMI HCHO/NO<sub>2</sub> ratio values was observed not only in summer months compared to winter months, but also in tier 2 days (red in **Fig. 5.9**) compared to tier 1 days. During the wildfire season months (e.g., July, August, and September), TROPOMI HCHO/NO<sub>2</sub> ratios on tier 2 days pushed the summer months further into the NO<sub>x</sub>-limited side of the transition point. The largest increase was observed in Sacramento Valley, followed by strong increases in SJV, and weak increases in SoCAB that were less statistically significant than the other two air basins. The magnitude of the increase in tier 2 days compared to tier 1 days appears to decrease as a function of the distance of the air basin from the largest burns from 2018-2020, which were largely in Northern California, and include:

- the August Complex fire (August 2020, over 1 million acres burned in North Coast and Sacramento Valley air basins)
- the Mendocino Complex fire (July 2018, reported 410,203 acres burned in North Coast and Sacramento Valley air basins)
- the LNU lightning Complex fire (August 2020, reported 396,624 acres burned in the San Francisco Bay Area and Sacramento Valley air basins).<sup>165</sup>

It is interesting to note that these tier 2 increases were also observed into October, when the seasonal cycle of the tier 1 days was already pushing back into VOC-limited regime. As wildfire occurrence and severity increase and the typical wildfire season is prolonged, this may result in these air basins remaining near the transition point for a longer period. It is noted that these increases were in general also observed in tier 3 days in SJV and Sacramento Valley, and the cause for this remains an intriguing question for future exploration.

To investigate the cause of the increase in the HCHO/NO<sub>2</sub> ratios on tier 2 days, wildfire emissions inventories were explored. Wildfire emissions are known to contain large amounts of CO, CO<sub>2</sub>, particulate matter, and both O<sub>3</sub> precursors VOCs and NO<sub>x</sub>.<sup>164</sup> The amount and relative contribution of these emissions are highly sensitive to fire duration, burning conditions, and fuel type.<sup>154,176,177</sup> The 2017 EPA National Emissions Inventory (NEI) reports that in the SJV, wildfire emissions contained 8 – 54 times more VOCs by weight than NO<sub>x</sub>, with a median ratio of 20.3 VOCs/NO<sub>x</sub> (w/w).<sup>164</sup> Thus it is reasonable to attribute the significantly higher TROPOMI HCHO/NO<sub>2</sub> ratios observed on tier 2 days in SJV and the Sacramento Valley to the large influx of VOCs from the wildfire plume,<sup>154,164</sup> which pushed the air basin further away from VOCs being the limiting factor in O<sub>3</sub> production.

In the SoCAB, which was often located furthest from major fires, the increase in VOCs from the plume may have been offset by a simultaneous increase in wildfire  $\text{NO}_x$  emissions, resulting in a less pronounced increase in the  $\text{HCHO}/\text{NO}_2$  ratio. While  $\text{NO}_x$  is also an important wildfire emission, it is rapidly sequestered as PAN, which acts as a temporary reservoir.<sup>154</sup> Subsequent thermal decomposition of PAN can thus regenerate  $\text{NO}_x$  further downwind, and thus became more important in an air basin that is furthest from the fires.

### 5.6 Effects on $\text{O}_3$ levels

**Fig. 5.11** shows MDA8  $\text{O}_3$  values on the different tiered days. As expected,  $\text{O}_3$  values peak in the summer months. Statistically significant differences were identified between tier 1 and tier 2 days during three months of wildfire season: August, September, and October. During these months,  $\text{O}_3$  increased on tier 2 days by  $14 \pm 5$  ppb on average in the SJV (error is the standard deviation amongst the medians of the three months),  $16 \pm 6$  in SoCAB, and  $16 \pm 4$  in Sacramento Valley compared to tier 1 days.





Figure 5.11: Visualization of MDA8 O<sub>3</sub> levels in each air basin aggregated by month from 2018-2020. Median values are bars across box, the top and bottom of boxes indicate the 75<sup>th</sup> and 25<sup>th</sup> percentiles, and whiskers show 90<sup>th</sup> and 10<sup>th</sup> percentiles. Outlier points have been hidden from the box-and-whiskers display, and instead individual data points are shown behind box plots. Statistical significance of tier 2 and tier 3 days compared to tier 1 days are calculated using Wilcoxon tests, where \* represents statistical significance (\* is  $p < 0.05$ , \*\* is  $p < 0.01$ , \*\*\* is  $p < 0.001$ , and \*\*\*\* is  $p < 0.0001$ ) and groups with no \* are not statistically different.

The highest increase in  $O_3$  was observed in October for both SJV (17 ppb, or a 40% increase from tier 1 values) and Sacramento Valley (20 ppb, 50% increase) and in August in SoCAB (23 ppb, 34% increase). It is interesting that in all three of these cases, the maximum  $O_3$  increase was observed when the TROPOMI HCHO/ $NO_2$  ratios straddled the transition point, with tier 1 days on the VOC-limited side and tier 2 days on the  $NO_x$ -limited side in **Figure 5.9**. It is likely that this large increase in  $O_3$  on these extreme air pollution event days is occurring because the VOC/ $NO_x$  ratio is near the most efficient  $O_3$  producing point (i.e. the ridgeline of an isopleth) yet is still sensitive to VOC increases from the influx of VOCs in wildfire plumes. While in SJV and Sacramento Valley this point occurs in October when seasonally  $O_3$  levels are not as high, in the SoCAB this point occurs at the most inopportune time: in August when  $O_3$  levels are already near their seasonally highest point, which exacerbates the challenge of NAAQS  $O_3$  attainment in the SoCAB. If future  $NO_x$  and VOC emissions reductions decreased in SoCAB, the overall arc of tier 1 values might descend closer to where the arcs for SJV and Sacramento Valley cross the transition point. This could potentially move the month where the most efficient  $O_3$  producing point is away from August towards October when meteorology is less favorable for  $O_3$  formation, and thus increase the probability of NAAQS attainment in SoCAB during wildfires in these highly sensitive months.

While the largest increases in  $O_3$  were detected during wildfire season, a somewhat different trend is observed in tier 2 days in January and February, where  $O_3$  production appeared lower on tier 2 days compared to tier 1 days. **Fig. 5.12** shows the difference between the tier 2 day values and tier 1 day values for median HCHO/ $NO_2$  ratios and MDA8  $O_3$  concentrations by month, and shows a general trend that data points for wildfire season (reds) and data points for January and February (blues) are in opposite corners. The tier 2

days in January and February are not associated with known fires in the CAL FIRE database,<sup>165</sup> and may be associated with prescribed burning which peaks in January and February as described earlier (**Fig. 5.8**), but may also be due to other types of unreported burning (such as residential).

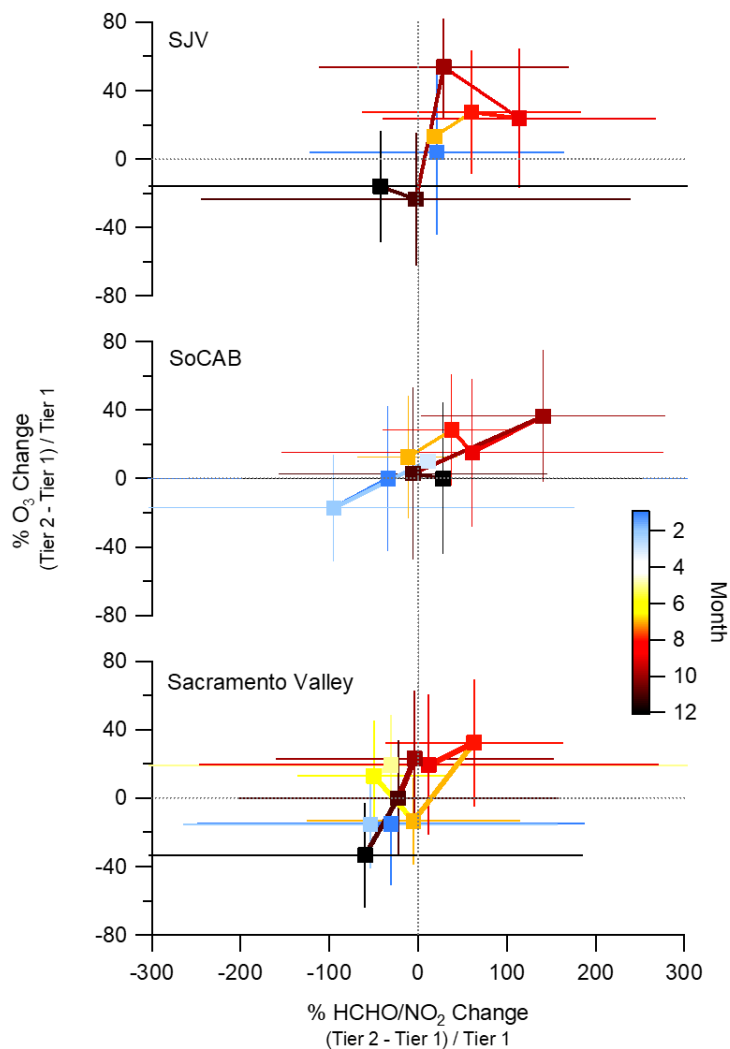


Figure 5.12: Visualization of observed HCHO/NO<sub>2</sub> ratio and O<sub>3</sub> differences on tier 2 and tier 1 days, colored by month. Wildfire season corresponds to red colors.

This suggests that extreme air pollution events associated with burning outside of wildfire season can have effects on O<sub>3</sub> chemistry that are unique from wildfires and may

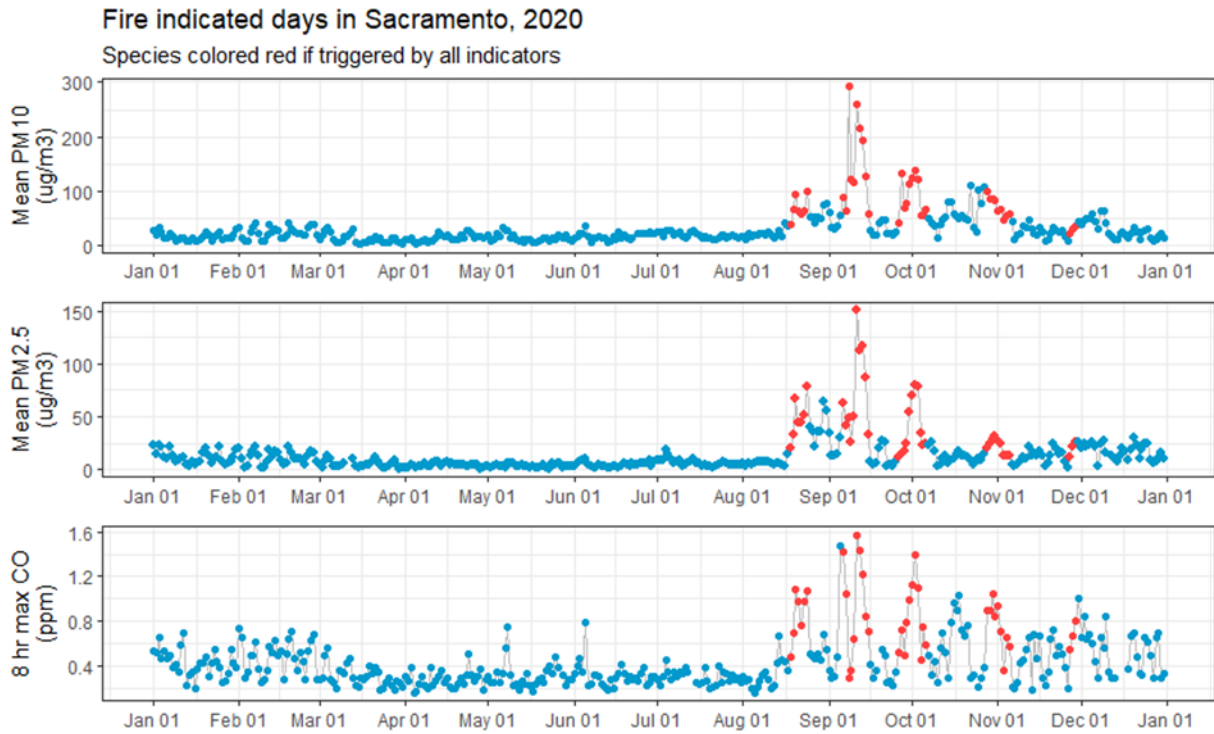
suggest that changes in prescribed burning under winter meteorological conditions offers a pathway to lower O<sub>3</sub> increases associated with the natural fire cycle. This is surprising, as the TROPOMI ratio shows a more VOC-limited environment in the winter, and one may have predicted O<sub>3</sub> formation to be more sensitive to a large flux of VOCs from a fire plume at this time. As this was not the case, it suggests that the TROPOMI ratio is not always a good indicator of O<sub>3</sub> production in the winter. This different chemistry may be due to a combination of differences in fire emission composition from the less intensely burning prescribed fires compared to wildfires, as well as meteorology during prescribed burning season. For example, lower photochemical activity in winter results in less efficient O<sub>3</sub> formation. Other winter meteorological conditions such as low temperatures, low turbulence, high moisture, and inversion conditions can also have an effect, particularly resulting in a lower planetary boundary layer during the cool, wet period and exacerbating accumulation of organic aerosol.<sup>178-180</sup> As O<sub>3</sub> is known to heterogeneously react on particle surfaces, this accumulation of one pollutant (organic aerosol), may be driving down the presence of another (O<sub>3</sub>), and highlights the need for integrated multi-pollutant control strategies.

To be clear, prescribed burning has many health concerns, as the emissions are a mixture of highly reactive VOCs which are likely to drive O<sub>3</sub> production downwind of the burning fire, in addition to large amounts of particulate matter and hazardous air pollutants. A prescribed burning strategy requires careful development to ensure that corresponding PM<sub>2.5</sub> and PM<sub>10</sub> exceedances and health threats are not exacerbated, especially since the SJV is one of the largest PM<sub>2.5</sub> non-attainment areas in the US.<sup>181</sup> Additional understanding of ambient

primary and secondary organic aerosol-O<sub>3</sub> interaction behavior during wintertime and consideration for reducing direct PM exposure in downwind communities is required.

### **5.7 Application of TED technique to field chamber studies in Sacramento**

The TED technique (to identify extreme air pollution events likely associated with wildfires) was also used to identify wildfire days in support of a field study measuring ozone response to NO<sub>x</sub> and VOC concentrations in Sacramento, CA in 2020.<sup>160</sup> In this study, in three identical chambers of ambient air samples were monitored: one chamber was a control of ambient air ozone formation, a second added NO<sub>x</sub> to the ambient air, and the third added surrogate VOCs to the ambient air. The ozone formation sensitivity was then compared for the NO<sub>x</sub> and VOC additions relative to the control chamber. In this case, data from two ground-monitors near the field site were combined: PM<sub>10</sub> and PM<sub>2.5</sub> data came from the Sacramento T-Street site and CO data came from the Sacramento – Bercut site (as neither site monitored for all three simultaneously), and results are shown in **Fig. 5.13**.



*Figure 5.13 Identification of extreme air pollution event days in Sacramento using the TED method.*

The results of the extreme air pollution event day identification were used to separate days where the ozone sensitivity in the ambient air samples in the chambers was likely influenced by wildfire smoke. Results are shown in **Fig. 5.13**.

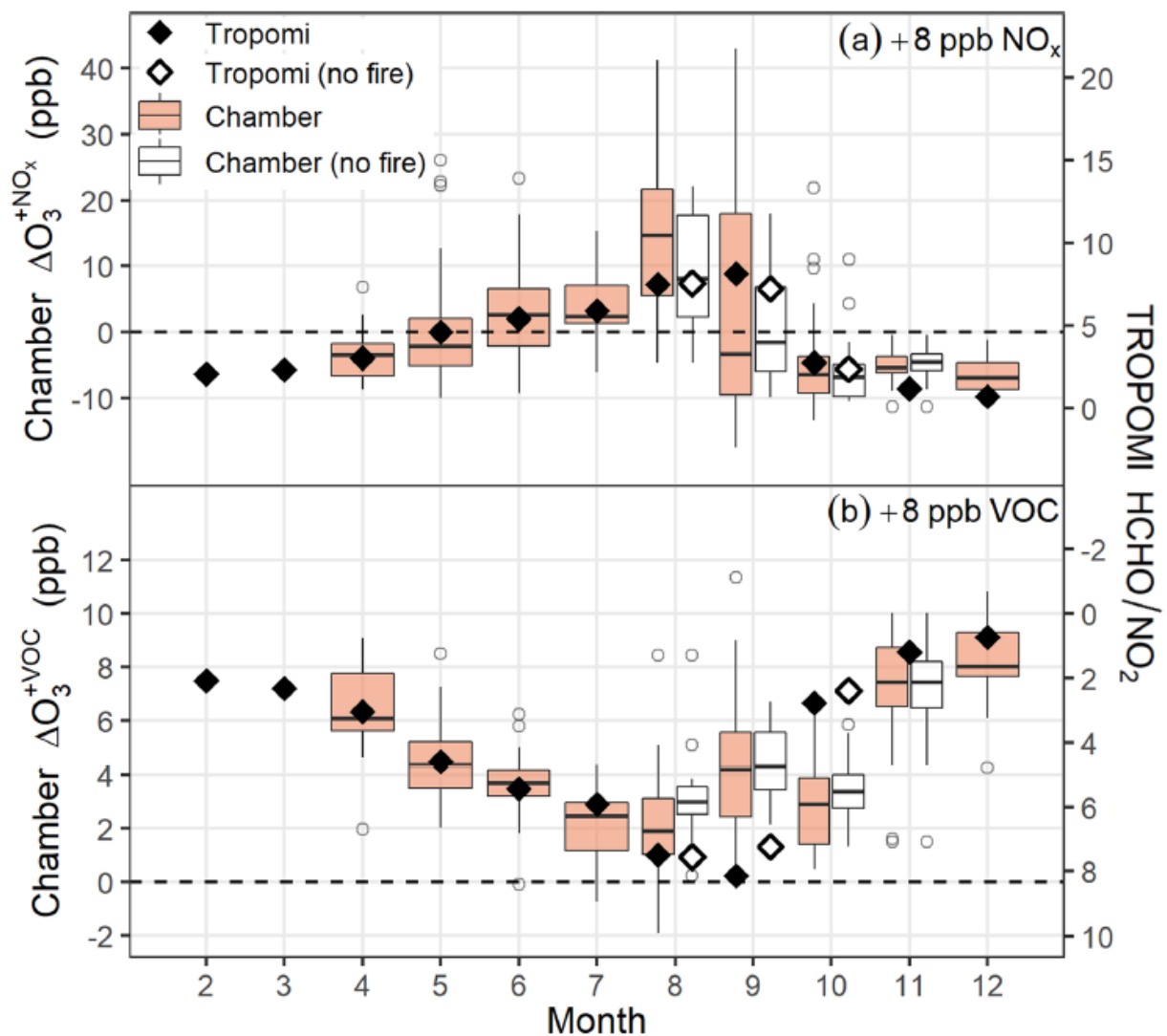


Figure 5.14 Monthly variation of  $\Delta O_3$  (box) observed in chamber studies due to  $NO_x$  addition ( $\Delta O_3^{+NO_x}$ , a) and VOC addition ( $\Delta O_3^{+VOC}$ , b) including wildfire days (shaded box) and without wildfire days (open box). TROPOMI HCHO/NO<sub>2</sub> values (diamond) are also shown. Adapted from Wu et al. 2022.<sup>160</sup>

The experimental chamber data (left axis, boxes) also observed the seasonal trend of a transition from a VOC-limited regime in the winter (increases in  $NO_x$  reduce  $O_3$  formation, increases in VOCs favor  $O_3$  formation) to a  $NO_x$ -limited regime in the summer (increases in  $NO_x$  enhance  $O_3$  formation). The corresponding TROPOMI HCHO/NO<sub>2</sub> observations (right axis, diamonds) for the area also follow a seasonal trend that increases in the summer,

meaning a transition to the NO<sub>x</sub>-limited regime. This is in agreement with TROPOMI HCHO/NO<sub>2</sub> trends reported in chapter 5.5 where an increase in the NO<sub>x</sub> sensitivity (higher TROPOMI HCHO/NO<sub>2</sub> ratio) is observed in the summer.

Additionally, separation of the TED-identified days greatly impacted the observed NO<sub>x</sub> sensitivity values in August. Sensitivity values including the wildfire days (shaded boxes) resulted in a higher observed NO<sub>x</sub> sensitivity ( $\Delta O_3^{+NO_x}$ ) and lower VOC sensitivity ( $\Delta O_3^{+VOC}$ ), meaning the wildfire days increased NO<sub>x</sub> sensitivity in August (to compare **Fig. 5.14** to **Fig. 5.9** and **Fig. 5.11**, open boxes are tier 1 days only, and shaded boxes are both tier 1 and tier 2 days.) The observed increase of HCHO/NO<sub>2</sub> ratio (i.e. more NO<sub>x</sub>-limited) observed in both the TROPOMI seasonal trend and in tier 2 data reported in chapter 5.5 are thus supported by direct chamber O<sub>3</sub> sensitivity measurements.

## 5.8 Conclusions

In California, fire is an intrinsic part of the landscape. As in other places in the world, wildfire management has become increasingly complex due to climate change, legacy fire abatement strategies, and housing growth into wildland-urban interfaces. Here we developed a statistical fire detection method using ground-level air quality monitors to identify extreme air pollution event (tier 2) days likely associated with fires across three California air basins (SJV, SoCAB, and Sacramento Valley). Concurrent TROPOMI satellite measurements of HCHO/NO<sub>2</sub> ratios (as surrogates for VOCs and NO<sub>x</sub>) provided simultaneous insight into O<sub>3</sub>-NO<sub>x</sub>-VOC sensitivity. An increase in the TROPOMI HCHO/NO<sub>2</sub> ratio was observed to have a seasonal cycle, with the lowest value on the VOC-limited side of the transition point in the winter, increasing towards the transition or more NO<sub>x</sub>-limited regime in the summer. Comparison of the extreme air pollution event (tier 2) days to control (tier



1) days showed that tier 2 days during wildfire season further increase the TROPOMI HCHO/NO<sub>2</sub> ratio towards or into the NO<sub>x</sub>-limited regime. Tier 2 days were also associated with increased O<sub>3</sub> levels, with the largest increase observed when tier 1 and tier 2 days were on opposite sides of the transition point. Outside of wildfire season, tier 2 days had a weaker or negative relationship on O<sub>3</sub>.

## REFERENCES

- (1) Caltech Fifty Years of Clearing the Skies. <https://www.caltech.edu/about/news/fifty-years-clearing-skies-39248> (accessed 3 May 2022).
- (2) Haagen-Smit, A. J., Chemistry and Physiology of Los Angeles Smog. *Industrial & Engineering Chemistry* **1952**, *44* (6), 1342-1346.
- (3) Haagen-smit, A. J.; Bradley, C. E.; Fox, M. M., Ozone Formation in Photochemical Oxidation of Organic Substances. *Ind. Eng. Chem.* **1953**, *45* (9), 2086-2089.
- (4) Haagen-Smit, A. J.; Fox, M. M., Photochemical Ozone Formation with Hydrocarbons and Automobile Exhaust. *Air Repair* **1954**, *4* (3), 105-136.
- (5) Molina, M. J.; Rowland, F. S., Stratospheric sink for chlorofluoromethanes: chlorine atom-catalysed destruction of ozone. *Nature* **1974**, *249* (5460), 810-812.
- (6) California State Water Resources Control Board Emerging Contaminants. [https://www.waterboards.ca.gov/drinking\\_water/certlic/drinkingwater/EmergingContaminants.html](https://www.waterboards.ca.gov/drinking_water/certlic/drinkingwater/EmergingContaminants.html) (accessed 3 May 2022).
- (7) California Department of Toxic Substances Control Chemicals of Emerging Concern. <https://dtsc.ca.gov/emerging-chemicals-of-concern/> (accessed 3 May 2022).
- (8) US Environmental Protection Agency (EPA) Contaminants of Emerging Concern including Pharmaceuticals and Personal Care Products. <https://www.epa.gov/wqc/contaminants-emerging-concern-including-pharmaceuticals-and-personal-care-products> (accessed 3 May 2022).
- (9) Brown, M. A.; Petreas, M. X.; Okamoto, H. S.; Mischke, T. M.; Stephens, R. D., Monitoring of Malathion and Its Impurities and Environmental Transformation Products on Surfaces and in Air Following an Aerial Application. *Environ Sci Technol* **1993**, *27* (2), 388-397.
- (10) Tomizawa, M.; Casida, J. E., Neonicotinoid insecticide toxicology: Mechanisms of selective action. *Annu. Rev. Pharmacool. Toxicol.* **2005**, *45*, 247-268.
- (11) Casida, J. E., Neonicotinoid metabolism: compounds, substituents, pathways, enzymes, organisms, and relevance. *J Agr Food Chem* **2011**, *59* (7), 2923-2931.
- (12) Debnath, B.; Gayen, S.; Basu, A.; Ghosh, B.; Srikanth, K.; Jha, T., Quantitative structure-activity relationship study using refractotopological state atom index on some neonicotinoid insecticides. *Biorg. Med. Chem.* **2004**, *12* (23), 6137-6145.
- (13) Zwart, R.; Oortgiesen, M.; Vijverberg, H. P. M., Nitromethylene heterocycles - selective agonists of nicotinic receptors in locust neurons compared to mouse N1e-115 and Bc3h1 cells. *Pestic. Biochem. Physiol.* **1994**, *48* (3), 202-213.
- (14) Goulson, D., Review: An overview of the environmental risks posed by neonicotinoid insecticides. *J Appl Ecol* **2013**, *50* (4), 977-987.
- (15) Buchholz, A.; Nauen, R., Translocation and translaminar bioavailability of two neonicotinoid insecticides after foliar application to cabbage and cotton. *Pest Manag Sci* **2002**, *58* (1), 10-16.
- (16) Elbert, A.; Haas, M.; Springer, B.; Thielert, W.; Nauen, R., Applied aspects of neonicotinoid uses in crop protection. *Pest Manag Sci* **2008**, *64* (11), 1099-1105.
- (17) Halmer, P., Commercial seed treatment technology. In *Seed technology and its biological basis*, Black, M. B., J.D., Ed. Sheffield, U.K., 2000; pp 257-286.

- (18) Hladik, M. L.; Main, A. R.; Goulson, D., Environmental risks and challenges associated with neonicotinoid insecticides. *Environ Sci Technol* **2018**, *52* (6), 3329-3335.
- (19) Stehle, S.; Schulz, R., Agricultural insecticides threaten surface waters at the global scale. *PNAS* **2015**, *112* (18), 5750-5755.
- (20) Morrissey, C. A.; Mineau, P.; Devries, J. H.; Sanchez-Bayo, F.; Liess, M.; Cavallaro, M. C.; Liber, K., Neonicotinoid contamination of global surface waters and associated risk to aquatic invertebrates: A review. *Environ Int* **2015**, *74*, 291-303.
- (21) Bonmatin, J. M.; Giorio, C.; Girolami, V.; Goulson, D.; Kreutzweiser, D. P.; Krupke, C.; Liess, M.; Long, E.; Marzaro, M.; Mitchell, E. A. D.; Noome, D. A.; Simon-Delso, N.; Tapparo, A., Environmental fate and exposure; neonicotinoids and fipronil. *Environ Sci Pollut R* **2015**, *22* (1), 35-67.
- (22) Goulson, D.; Nicholls, E.; Botias, C.; Rotheray, E. L., Bee declines driven by combined stress from parasites, pesticides, and lack of flowers. *Science* **2015**, *347* (6229), 1255957-1 - 1255957-9.
- (23) Wood, T. J.; Goulson, D., The environmental risks of neonicotinoid pesticides: a review of the evidence post 2013. *Environ Sci Pollut R* **2017**, *24* (21), 17285-17325.
- (24) Fischer, J.; Muller, T.; Spatz, A. K.; Greggers, U.; Grunewald, B.; Menzel, R., Neonicotinoids interfere with specific components of navigation in honeybees. *Plos One* **2014**, *9* (3), 1-10.
- (25) Girolami, V.; Mazzon, L.; Squartini, A.; Mori, N.; Marzaro, M.; Di Bernardo, A.; Greatti, M.; Giorio, C.; Tapparo, A., Translocation of neonicotinoid insecticides from coated seeds to seedling guttation drops: a novel way of intoxication for bees. *J Econ Entomol* **2009**, *102* (5), 1808-1815.
- (26) Pisa, L. W.; Amaral-Rogers, V.; Belzunces, L. P.; Bonmatin, J. M.; Downs, C. A.; Goulson, D.; Kreutzweiser, D. P.; Krupke, C.; Liess, M.; McField, M.; Morrissey, C. A.; Noome, D. A.; Settele, J.; Simon-Delso, N.; Stark, J. D.; Van der Sluijs, J. P.; Van Dyck, H.; Wiemers, M., Effects of neonicotinoids and fipronil on non-target invertebrates. *Environ Sci Pollut R* **2015**, *22* (1), 68-102.
- (27) Crall, J. D.; Switzer, C. M.; Oppenheimer, R. L.; Versypt, A. N. F.; Dey, B.; Brown, A.; Eyster, M.; Guerin, C.; Pierce, N. E.; Combes, S. A.; de Bivort, B. L., Neonicotinoid exposure disrupts bumblebee nest behavior, social networks, and thermoregulation. *Science* **2018**, *362* (6415), 683-686.
- (28) Rundlof, M.; Andersson, G. K. S.; Bommarco, R.; Fries, I.; Hederstrom, V.; Herbertsson, L.; Jonsson, O.; Klatt, B. K.; Pedersen, T. R.; Yourstone, J.; Smith, H. G., Seed coating with a neonicotinoid insecticide negatively affects wild bees. *Nature* **2015**, *521* (7550), 77-80.
- (29) Tsvetkov, N.; Samson-Robert, O.; Sood, K.; Patel, H. S.; Malena, D. A.; Gajiwala, P. H.; Maciukiewicz, P.; Fournier, V.; Zayed, A., Chronic exposure to neonicotinoids reduces honey bee health near corn crops. *Science* **2017**, *356* (6345), 1395-1397.
- (30) Blacquiere, T.; Smagghe, G.; Van Gestel, C. A. M.; Mommaerts, V., Neonicotinoids in bees: a review on concentrations, side-effects and risk assessment (vol 21, pg 973, 2012). *Ecotoxicology* **2012**, *21* (5), 1581-1581.
- (31) Whitehorn, P. R.; O'Connor, S.; Wackers, F. L.; Goulson, D., Neonicotinoid pesticide reduces bumble bee colony growth and queen production. *Science* **2012**, *336* (6079), 351-352.

- (32) Kadlikova, K.; Vaclavikova, M.; Halesova, T.; Kamler, M.; Markovic, M.; Erban, T., The investigation of honey bee pesticide poisoning incidents in Czechia. *Chemosphere* **2021**, *263*, (128056).
- (33) European Commission. 2018. Commission Implementing Regulation (EU) 2018/783 of 29 May 2018, Implementing Regulation (EU) No 540/2011 as regards the conditions of approval of the active substance imidacloprid, clothianidin, and thiamethoxam. <https://eur-lex.europa.eu/legal-content/EN/TXT/PDF/?uri=CELEX:32018R0785> (accessed November 27, 2018).
- (34) California Department of Pesticide Regulation Neonicotinoids. <https://www.cdpr.ca.gov/docs/registration/reevaluation/chemicals/neonicotinoids.htm> (accessed 27 April 2022).
- (35) Greatti, M.; Sabatini, A. G.; Barbatinni, R.; Rossi, S.; Stravasi, A., Risk of environmental contamination by the active ingredient imidacloprid used for corn seed dressing. *Bulletin of Insectology* **2003**, *56* (1), 69-72.
- (36) Craddock, H. A.; Huang, D.; Turner, P. C.; Quirós-Alcalá, L.; Payne-Sturges, D. C., Trends in neonicotinoid pesticide residues in food and water in the United States, 1999–2015. *Environ. Health* **2019**, *18* (1), 1-16.
- (37) Lu, C.; Chang, C.-H.; Palmer, C.; Zhao, M.; Zhang, Q., Neonicotinoid residues in fruits and vegetables: an integrated dietary exposure assessment approach. *Environ Sci Technol* **2018**, *52* (5), 3175-3184.
- (38) Liu, S.; Zheng, Z.; Wei, F.; Ren, Y.; Gui, W.; Wu, H.; Zhu, G., Simultaneous determination of seven neonicotinoid pesticide residues in food by ultraperformance liquid chromatography tandem mass spectrometry. *J Agr Food Chem* **2010**, *58* (6), 3271-3278.
- (39) Mitchell, E. A. D.; Mulhauser, B.; Mulo, M.; Mutabazi, A.; Glauser, G.; Aebi, A., A worldwide survey of neonicotinoids in honey. *Science* **2017**, *358* (6359), 109-111.
- (40) Mullin, C. A.; Frazier, M.; Frazier, J. L.; Ashcraft, S.; Simonds, R.; vanEngelsdorp, D.; Pettis, J. S., High levels of miticides and agrochemicals in North American apiaries: implications for honey bee health. *Plos One* **2010**, *5* (3), 1-19.
- (41) Botias, C.; David, A.; Horwood, J.; Abdul-Sada, A.; Nicholls, E.; Hill, E.; Goulson, D., Neonicotinoid residues in wildflowers, a potential route of chronic exposure for bees. *Environ Sci Technol* **2015**, *49* (21), 12731-12740.
- (42) Chao, S. L.; Casida, J. E., Interaction of imidacloprid metabolites and analogs with the nicotinic acetylcholine receptor of mouse brain in relation to toxicity. *Pestic. Biochem. Physiol.* **1997**, *58* (1), 77-88.
- (43) Woodcock, B. A.; Bullock, J. M.; Shore, R. F.; Heard, M. S.; Pereira, M. G.; Redhead, J.; Ridding, L.; Dean, H.; Sleep, D.; Henrys, P.; Peyton, J.; Hulmes, S.; Hulmes, L.; Sarospataki, M.; Saure, C.; Edwards, M.; Genersch, E.; Knabe, S.; Pywell, R. F., Country-specific effects of neonicotinoid pesticides on honey bees and wild bees. *Science* **2017**, *356* (6345), 1393-1395.
- (44) George, C.; Ammann, M.; D'Anna, B.; Donaldson, D. J.; Nizkorodov, S. A., Heterogeneous photochemistry in the atmosphere. *Chem. Rev.* **2015**, *115* (10), 4218-4258.
- (45) Lester, Y.; Sabach, S.; Zivan, O.; Dubowski, Y., Key environmental processes affecting the fate of the insecticide chlorpyrifos applied to leaves. *Chemosphere* **2017**, *171*, 74-80.
- (46) Kira, O.; Linker, R.; Dubowski, Y., Estimating drift of airborne pesticides during orchard spraying using active Open Path FTIR. *Atmos. Environ.* **2016**, *142*, 264-270.

- (47) Estillore, A. D.; Trueblood, J. V.; Grassian, V. H., Atmospheric chemistry of bioaerosols: heterogeneous and multiphase reactions with atmospheric oxidants and other trace gases. *Chem Sci* **2016**, *7* (11), 6604-6616.
- (48) Sur, R.; Stork, A., Uptake, translocation and metabolism of imidacloprid in plants. *Bulletin of Insectology* **2003**, *56* (1), 35-40.
- (49) Wintermantel, D.; Odoux, J. F.; Decourtye, A.; Henry, M.; Allier, F.; Bretagnolle, V., Neonicotinoid-induced mortality risk for bees foraging on oilseed rape nectar persists despite EU moratorium. *Sci. Total Environ.* **2020**, *704*, 135400.
- (50) Humann-Guillemot, S.; Clement, S.; Desprat, J.; Binkowski, L. J.; Glauser, G.; Helfenstein, F., A large-scale survey of house sparrows feathers reveals ubiquitous presence of neonicotinoids in farmlands. *Sci. Total Environ.* **2019**, *660*, 1091-1097.
- (51) Distefano, G. G.; Zangrando, R.; Basso, M.; Panzarin, L.; Gambaro, A.; Volpi Ghirardini, A.; Picone, M., The ubiquity of neonicotinoid contamination: Residues in seabirds with different trophic habits. *Environ. Res.* **2022**, *206*, 112637.
- (52) Zhang, Q.; Li, Z.; Chang, C. H.; Lou, J. L.; Zhao, M. R.; Lu, C., Potential human exposures to neonicotinoid insecticides: A review. *Environ. Pollut.* **2018**, *236*, 71-81.
- (53) Han, W.; Tian, Y.; Shen, X., Human exposure to neonicotinoid insecticides and the evaluation of their potential toxicity: An overview. *Chemosphere* **2018**, *192*, 59-65.
- (54) Bonmatin, J. M.; Mitchell, E. A. D.; Glauser, G.; Lumawig-Heitzman, E.; Claveria, F.; van Lexmond, M. B.; Taira, K.; Sanchez-Bayo, F., Residues of neonicotinoids in soil, water and people's hair: A case study from three agricultural regions of the Philippines. *Sci. Total Environ.* **2021**, *757*.
- (55) Zhang, D.; Lu, S., Human exposure to neonicotinoids and the associated health risks: A review. *Environ Int* **2022**, *163*, 107201.
- (56) Pietrzak, D.; Kania, J.; Kmiecik, E.; Malina, G.; Wator, K., Fate of selected neonicotinoid insecticides in soil-water systems: Current state of the art and knowledge gaps. *Chemosphere* **2020**, *255*.
- (57) Klarich, K. L.; Pflug, N. C.; DeWald, E. M.; Hladik, M. L.; Kolpin, D. W.; Cwiertny, D. M.; LeFevre, G. H., Occurrence of Neonicotinoid Insecticides in Finished Drinking Water and Fate during Drinking Water Treatment. *Environ Sci Tech Let* **2017**, *4* (5), 168-173.
- (58) Mahai, G.; Wan, Y. J.; Xia, W.; Wang, A. Z.; Shi, L. S.; Qian, X.; He, Z. Y.; Xu, S. Q., A nationwide study of occurrence and exposure assessment of neonicotinoid insecticides and their metabolites in drinking water of China. *Water Res.* **2021**, *189*.
- (59) Baghirzade, B. S.; Yetis, U.; Dilek, F. B., Imidacloprid elimination by O<sub>3</sub> and O<sub>3</sub>/UV: kinetics study, matrix effect, and mechanism insight. *Environ Sci Pollut R* **2021**, *28* (19), 24535-24551.
- (60) Bourgin, M.; Violleau, F.; Debrauwer, L.; Albet, J., Ozonation of imidacloprid in aqueous solutions: Reaction monitoring and identification of degradation products. *J. Hazard. Mater.* **2011**, *190* (1-3), 60-68.
- (61) Chen, S.; Deng, J.; Deng, Y.; Gao, N., Influencing factors and kinetic studies of imidacloprid degradation by ozonation. *Environ. Technol.* **2019**, *40* (16), 2127-2134.
- (62) Liu, X.; Wu, X. L.; Long, Z.; Zhang, C.; Ma, Y. Q.; Hao, X. H.; Zhang, H. Y.; Pan, C. P., Photodegradation of Imidacloprid in Aqueous Solution by the Metal-Free Catalyst Graphitic Carbon Nitride using an Energy-Saving Lamp. *J Agr Food Chem* **2015**, *63* (19), 4754-4760.
- (63) Kan, Q. H.; Lu, K.; Dong, S. P.; Shen, D. L.; Huang, Q. G.; Tong, Y.; Wu, W.; Gao, S. X.; Mao, L., Transformation and removal of imidacloprid mediated by silver ferrite nanoparticle

facilitated peroxymonosulfate activation in water: Reaction rates, products, and pathways. *Environ. Pollut.* **2020**, 267.

(64) Malato, S.; Caceres, J.; Aguera, A.; Mezcuca, M.; Hernando, D.; Vial, J.; Fernandez-Alba, A. R., Degradation of imidacloprid in water by photo-Fenton and TiO<sub>2</sub> photocatalysis at a solar pilot plant: A comparative study. *Environ Sci Technol* **2001**, 35 (21), 4359-4366.

(65) Lacson, C. F. Z.; de Luna, M. D. G.; Dong, C. D.; Garcia-Segura, S.; Lu, M. C., Fluidized-bed Fenton treatment of imidacloprid: Optimization and degradation pathway. *Sustain Environ Res* **2018**, 28 (6), 309-314.

(66) Turabik, M.; Oturan, N.; Gözmen, B.; Oturan, M. A., Efficient removal of insecticide "imidacloprid" from water by electrochemical advanced oxidation processes. *Environ Sci Pollut R* **2014**, 21 (14), 8387-8397.

(67) Kitsiou, V.; Filippidis, N.; Mantzavinos, D.; Poulios, I., Heterogeneous and homogeneous photocatalytic degradation of the insecticide imidacloprid in aqueous solutions. *Applied Catalysis B: Environmental* **2009**, 86 (1), 27-35.

(68) Finlayson-Pitts, B. J.; Pitts, J. N., *Chemistry of the Upper and Lower Atmosphere: Theory, Experiments, and Application*. Academic Press: San Diego, 2000.

(69) Harrick, N. J., *Internal Reflection Spectroscopy*. 3rd ed.; Harrick Scientific Corporation: Ossining, New York, 1979.

(70) Aregahegn, K. Z.; Shemesh, D.; Gerber, R. B.; Finlayson-Pitts, B. J., Photochemistry of thin solid films of the neonicotinoid imidacloprid on surfaces. *Environ Sci Technol* **2017**, 51 (5), 2660-2668.

(71) Wang, W.; Aregahegn, K. Z.; Andersen, S. T.; Ni, A. Z.; Rohrbacher, A. F.; Nielsen, O. J.; Finlayson-Pitts, B. J., Quantum yields and N<sub>2</sub>O formation from photolysis of solid films of neonicotinoids. *J Agr Food Chem* **2019**, 67 (6), 1638-1646.

(72) Aregahegn, K. Z.; Shemesh, D.; Gerber, R. B.; Finlayson-Pitts, B. J., Photochemistry of Thin Solid Films of the Neonicotinoid Imidacloprid on Surfaces. *Environ. Sci. Technol.* **2017**, 51 (5), 2660-2668.

(73) Redlich, D.; Shahin, N.; Ekici, P.; Friess, A.; Parlar, H., Kinetic study of the photoinduced degradation of imidacloprid in aquatic media. *Clean* **2007**, 35 (5), 452-458.

(74) Lu, Z.; Challis, J. K.; Wong, C. S., Quantum yields for direct photolysis of neonicotinoid insecticides in water: implications for exposure to nontarget aquatic organisms. *Environ. Sci. Technol. Lett.* **2015**, 2 (7), 188-192.

(75) von Gunten, K. Photodegradation and sorption to Na-SAz clay, soil, and pollen of the neonicotinoids acetamiprid, clothianidin, imidacloprid and thiacloprid. **2012**. <https://www.yumpu.com/en/document/view/7393414/photodegradation-and-sorption-to-na-sazclay-soil-eth-zurich> (last accessed September 15, 2016).

(76) Aregahegn, K. Z.; Ezell, M. J.; Finlayson-Pitts, B. J., Photochemistry of solid films of the neonicotinoid nitenpyram. *Environ Sci Technol* **2018**, 52 (5), 2760-2767.

(77) Valent. 2015. Safari 20SG Insecticide Safety Data Sheet, SDS No 0426. <http://www.cdms.net/ldat/mpAC2001.pdf> (accessed 17 April 2022).

(78) FDA Professional Drug Information Database available via <https://www.drugs.com/pro/capstar.html>. Accessed 17 April 2020.

(79) CRC Handbook of Chemistry and Physics. Rumble, J. R., Ed. CRC Press/Taylor & Francis: Boca Raton, Fl., 2020.

(80) Le Questel, J. Y.; Graton, J.; Ceron-Carrasco, J. P.; Jacquemin, D.; Planchat, A.; Thany, S. H., New insights on the molecular features and electrophysiological properties of

dinotefuran, imidacloprid and acetamiprid neonicotinoid insecticides. *Biorg. Med. Chem.* **2011**, *19* (24), 7623-7634.

(81) Noestheden, M.; Roberts, S.; Hao, C. Y., Nitenpyram degradation in finished drinking water. *Rapid Commun. Mass Spectrom.* **2016**, *30* (13), 1653-1661.

(82) Socrates, G., *Infrared and Raman Characteristic Group Frequencies: Tables and Charts*. 3rd ed.; John Wiley & Sons Ltd.: West Sussex, England, 2001.

(83) Rohrbacher, A.; Ezell, M. J.; Perraud, V.; Finlayson-Pitts, B. J., Probing Matrix Effects on the Heterogeneous Photochemistry of Neonicotinoid Pesticides, Dinotefuran and Nitenpyram. *Acs Earth Space Chem* **2021**, *5* (5), 1196-1209.

(84) Raina-Fulton, R.; Behdarvandan, A., Liquid chromatography-mass spectrometry for the determination of neonicotinoid insecticides and their metabolites in biological, environmental and food commodity matrices. *Trends in Chromatography* **2016**, *10*, 51-79.

(85) Kamel, A., Refined methodology for the determination of neonicotinoid pesticides and their metabolites in honey bees and bee products by liquid chromatography-tandem mass spectrometry (LC-MS/MS). *J Agr Food Chem* **2010**, *58* (10), 5926-5931.

(86) Yang, Z. H.; Zhang, K. K.; Chen, L. Z.; Liu, B.; Zhang, Q. T.; Zhang, H. Z.; Sun, C. Y.; Hu, D. Y., Determination of dinotefuran and its metabolites in orange pulp, orange peel, and whole orange using liquid chromatography-tandem mass spectrometry. *J. AOAC Int.* **2017**, *100* (5), 1551-1558.

(87) Kamel, A.; Qian, Y. R.; Kolbe, E.; Stafford, C., Development and validation of a multiresidue method for the determination of neonicotinoid and macrocyclic lactone pesticide residues in milk, fruits, and vegetables by ultra-performance liquid chromatography/MS/MS. *J. AOAC Int.* **2010**, *93* (2), 389-399.

(88) Xie, W.; Han, C.; Qian, Y.; Ding, H. Y.; Chen, X. M.; Xi, J. Y., Determination of neonicotinoid pesticides residues in agricultural samples by solid-phase extraction combined with liquid chromatography-tandem mass spectrometry. *J. Chromatogr. A* **2011**, *1218* (28), 4426-4433.

(89) EPA, U. S. Dinotefuran Pesticide Fact Sheet. [https://www3.epa.gov/pesticides/chem\\_search/reg\\_actions/registration/fs\\_PC-044312\\_01-Sep-04.pdf](https://www3.epa.gov/pesticides/chem_search/reg_actions/registration/fs_PC-044312_01-Sep-04.pdf).

(90) Laane, J. O., J.R., Characterization of nitrogen oxides by vibrational spectroscopy. In *Progress in Inorganic Chemistry*, 1980; pp 465-513.

(91) Coblenz Society Inc., Evaluated Infrared Reference Spectra. In *NIST Chemistry WebBook, NIST Standard Reference Database Number 69*, Linstrom, P. J.; Mallard, W. G., Eds.

(92) Dows, D. A., Infrared spectrum of solid nitrous oxide. *J. Chem. Phys.* **1957**, *26* (4), 745-747.

(93) Yamada, H.; Person, W. B., Absolute infrared intensities of fundamental absorption bands in solid CO<sub>2</sub> + N<sub>2</sub>O. *J. Chem. Phys.* **1964**, *41* (8), 2478-2487.

(94) Hisatsune, I. C., Infrared spectrum of matrix isolated nitrous oxide. *J. Chem. Phys.* **1972**, *57* (7), 2631-2636.

(95) Hadjiivanov, K.; Saussey, J.; Freysz, J. L.; Lavalley, J. C., FT-IR study of NO + O<sub>2</sub> co-adsorption on H-ZSM-5: re-assignment of the 2133 cm<sup>-1</sup> band to NO<sup>+</sup> species. *Catal. Lett.* **1998**, *52* (1), 103-108.

(96) Pommier, B.; Gelin, P., Infrared and volumetric study of NO adsorption on Pd-H-ZSM-5. *PCCP* **2001**, *3* (6), 1138-1143.

- (97) Hadjiivanov, K.; Knözinger, H., Species formed after NO adsorption and NO + O<sub>2</sub> co-adsorption on TiO<sub>2</sub>: an FTIR spectroscopic study. *PCCP* **2000**, *2* (12), 2803-2806.
- (98) Lobree, L. J.; Hwang, I. C.; Reimer, J. A.; Bell, A. T., An in situ infrared study of NO reduction by C<sub>3</sub>H<sub>8</sub> over Fe-ZSM-5. *Catal. Lett.* **1999**, *63* (3), 233-240.
- (99) Konduru, M. V.; Chuang, S. S. C., Dynamics of NO and N<sub>2</sub>O decomposition over Cu-ZSM-5 under transient reducing and oxidizing conditions. *J. Catal.* **2000**, *196* (2), 271-286.
- (100) Joyner, R.; Stockenhuber, M., Preparation, characterization, and performance of Fe-ZSM-5 catalysts. *J. Phys. Chem. B* **1999**, *103* (29), 5963-5976.
- (101) Hadjiivanov, K. I., IR study of CO and NO<sub>x</sub> sorption on Ag-ZSM-5. *Microporous Mesoporous Mater.* **1998**, *24* (1), 41-49.
- (102) Gerlach, T.; Schutze, F. W.; Baerns, M., An FTIR study on the mechanism of the reaction between nitrogen dioxide and propene over acidic mordenites. *J. Catal.* **1999**, *185* (1), 131-137.
- (103) Chen, H. Y.; Voskoboinikov, T.; Sachtler, W. M. H., Reduction of NO<sub>x</sub> over Fe/ZSM-5 catalysts: mechanistic causes of activity differences between alkanes. *Catal. Today* **1999**, *54* (4), 483-494.
- (104) Gelin, P.; Goguet, A.; Descorme, C.; Lecuyer, C.; Primet, M., Catalytic properties of palladium exchanged ZSM-5 catalysts in the reduction of nitrogen monoxide by methane in the presence of oxygen: Nature of the active sites. *Stud Surf Sci Catal* **1998**, *116*, 275-284.
- (105) Finlayson-Pitts, B. J.; Johnson, S. N., The reaction of NO<sub>2</sub> with NaBr - possible source of BrNO in polluted marine atmospheres. *Atmos. Environ.* **1988**, *22* (6), 1107-1112.
- (106) Calvert, J. G.; Pitts, J. N., *Photochemistry*. John Wiley & Sons, Inc.: 1966.
- (107) Klan, P.; Wirz, J., *Photochemistry of Organic Compounds: From Concepts to Practice*. John Wiley & Sons, Ltd.: 2009.
- (108) Bhattacharya, A.; Guo, Y. Q.; Bernstein, E. R., Experimental and theoretical exploration of the initial steps in the decomposition of a model nitramine energetic material: dimethylnitramine. *J. Phys. Chem. A* **2009**, *113* (5), 811-823.
- (109) Groffman, P. M.; Butterbach-Bahl, K.; Fulweiler, R. W.; Gold, A. J.; Morse, J. L.; Stander, E. K.; Tague, C.; Tonitto, C.; Vidon, P., Challenges to incorporating spatially and temporally explicit phenomena (hotspots and hot moments) in denitrification models. *Biogeochemistry* **2009**, *93* (1), 49-77.
- (110) Groffman, P. M.; Altabet, M. A.; Böhlke, J. K.; Butterbach-Bahl, K.; David, M. B.; Firestone, M. K.; Giblin, A. E.; Kana, T. M.; Nielsen, L. P.; Voytek, M. A., Methods for measuring denitrification: diverse approaches to a difficult problem. *Ecological Applications* **2006**, *16* (6), 2091-2122.
- (111) Wolf, B.; Zheng, X.; Brüggemann, N.; Chen, W.; Dannenmann, M.; Han, X.; Sutton, M. A.; Wu, H.; Yao, Z.; Butterbach-Bahl, K., Grazing-induced reduction of natural nitrous oxide release from continental steppe. *Nature* **2010**, *464* (7290), 881-884.
- (112) Fowler, D.; Pilegaard, K.; Sutton, M. A.; Ambus, P.; Raivonen, M.; Duyzer, J.; Simpson, D.; Fagerli, H.; Fuzzi, S.; Schjoerring, J. K.; Granier, C.; Neftel, A.; Isaksen, I. S. A.; Laj, P.; Maione, M.; Monks, P. S.; Burkhardt, J.; Daemmgen, U.; Neiryneck, J.; Personne, E.; Wichink-Kruit, R.; Butterbach-Bahl, K.; Flechard, C.; Tuovinen, J. P.; Coyle, M.; Gerosa, G.; Loubet, B.; Altimir, N.; Gruenhage, L.; Ammann, C.; Cieslik, S.; Paoletti, E.; Mikkelsen, T. N.; Ro-Poulsen, H.; Cellier, P.; Cape, J. N.; Horvath, L.; Loreto, F.; Niinemets, U.; Palmer, P. I.; Rinne, J.; Misztal, P.; Nemitz, E.; Nilsson, D.; Pryor, S.; Gallagher, M. W.; Vesala, T.; Skiba, U.; Brüggemann, N.; Zechmeister-Boltenstern, S.; Williams, J.; O'Dowd, C.; Facchini, M. C.; de



- Leeuw, G.; Flossman, A.; Chaumerliac, N.; Erisman, J. W., Atmospheric composition change: Ecosystems-Atmosphere interactions. *Atmos. Environ.* **2009**, *43* (33), 5193-5267.
- (113) Leighton, P. A.; Lucy, F. A., The photoisomerization of the o-nitrobenzaldehydes I. photochemical results. *J. Chem. Phys.* **1934**, *2* (11), 756-759.
- (114) Pitts, J. N.; Wan, J. K. S.; Schuck, E., Photochemical studies in an alkali halide matrix. I. An o-nitrobenzaldehyde actinometer and its application to a kinetic study of the photoreduction of benzophenone by benzhydrol in a pressed potassium bromide disk. *J. Am. Chem. Soc.* **1964**, *86* (18), 3606-3610.
- (115) Vichutinskaya, E. V.; Postnikov, L. M.; Kushnerev, M. Y., Use of ortho-nitrobenzaldehyde as an internal actinometer in investigation of photooxidative degradation of thin unoriented polycapromide films. *Vysokomol Soedin a+* **1975**, *17* (3), 621-625.
- (116) Allen, J. M.; Allen, S. K.; Baertschi, S. W., 2-Nitrobenzaldehyde: a convenient UV-A and UV-B chemical actinometer for drug photostability testing. *J. Pharm. Biomed. Anal.* **2000**, *24* (2), 167-178.
- (117) Liu, R. S. H.; Hammond, G. S., Reflection on medium effects on photochemical reactivity. *Acc. Chem. Res.* **2005**, *38* (5), 396-403.
- (118) Ezell, M. J.; Wang, W. H.; Shemesh, D.; Ni, A.; Gerber, R. B.; Finlayson-Pitts, B. J., Experimental and theoretical studies of the environmental sensitivity of the absorption spectra and photochemistry of nitenpyram and analogs. *Acs Earth Space Chem* **2019**, *3* (9), 2063-2075.
- (119) Raff, J. D.; Finlayson-Pitts, B. J., Hydroxyl radical quantum yields from isopropyl nitrite photolysis in air. *Environ Sci Technol* **2010**, *44* (21), 8150-8155.
- (120) Moussa, S. G.; Finlayson-Pitts, B. J., Reaction of gas phase OH with unsaturated self-assembled monolayers and relevance to atmospheric organic oxidations. *PCCP* **2010**, *12* (32), 9419-9428.
- (121) J. B. Burkholder, S. P. S., J. Abbatt, J. R. Barker, C. Cappa, J. D. Crouse, T. S. Dibble, R. E. Huie, C. E. Kolb, M. J. Kurylo, V. L. O., C. J. Percival, D. M. Wilmouth, and P. H. Wine. 2019. Chemical Kinetics and Photochemical Data for Use in Atmospheric Studies, Evaluation No. 19. <http://jpldataeval.jpl.nasa.gov>.
- (122) Pluskal, T. C., S.; Villar-Briones, A.; Orešič, M., MZmine 2: Modular framework for processing, visualizing, and analyzing mass spectrometry-based molecular profile data. *BMC Bioinformatics* **2010**, *11* (395).
- (123) Vander Wall, A. C.; Lakey, P. S. J.; Molina, E. R.; Perraud, V.; Wingen, L. M.; Xu, J.; Soulsby, D.; Gerber, R. B.; Shiraiwa, M.; Finlayson-Pitts, B. J., Understanding interactions of organic nitrates with the surface and bulk of organic films: implications for particle growth in the atmosphere. *Environ Sci-Proc Imp* **2018**, *20* (11), 1593-1610.
- (124) Atkinson, R., A Structure-Activity Relationship for the Estimation of Rate Constants for the Gas-Phase Reactions of Oh Radicals with Organic-Compounds. *Int. J. Chem. Kinet.* **1987**, *19* (9), 799-828.
- (125) Atkinson, R., Kinetics and Mechanisms of the Gas-Phase Reactions of the Hydroxyl Radical with Organic-Compounds under Atmospheric Conditions. *Chem. Rev.* **1986**, *86* (1), 69-201.
- (126) Rozsa, G.; Nafradi, M.; Alapi, T.; Schrantz, K.; Szabo, L.; Wojnarovits, L.; Takacs, E.; Tungler, A., Photocatalytic, photolytic and radiolytic elimination of imidacloprid from aqueous solution: Reaction mechanism, efficiency and economic considerations. *Appl Catal B-Environ* **2019**, *250*, 429-439.

(127) Anderson, A. F.-P., B.J., Heterogeneous OH radical reactions with thin films of neonicotinoid pesticides:

kinetics, products, mechanisms, and environmental implications. **In preparation.**

(128) Wang, W. C.; Huang, D. Y.; Wang, D. X.; Tan, M. X.; Geng, M. Y.; Zhu, C. Y.; Chen, N.; Zhou, D. M., Extensive production of hydroxyl radicals during oxygenation of anoxic paddy soils: Implications to imidacloprid degradation. *Chemosphere* **2022**, 286.

(129) *Direct Analysis in Real Time Mass Spectrometry: Principles and Practices of DART-MS*. Wiley-VCH: 2018; p 376.

(130) Nauen, R.; Tietjen, K.; Wagner, K.; Elbert, A., Efficacy of plant metabolites of imidacloprid against *Myzus persicae* and *Aphis gossypii* (Homoptera: Aphididae). *Pesticide Science* **1998**, 52 (1), 53-57.

(131) Benton, E. P.; Grant, J. F.; Webster, R. J.; Nichols, R. J.; Cowles, R. S.; Lagalante, A. F.; Coats, C. I., Assessment of Imidacloprid and Its Metabolites in Foliage of Eastern Hemlock Multiple Years Following Treatment for Hemlock Woolly Adelgid, *Adelges tsugae* (Hemiptera: Adelgidae), in Forested Conditions. *J Econ Entomol* **2015**, 108 (6), 2672-2682.

(132) Seifrtova, M.; Halesova, T.; Sulcova, K.; Riddellova, K.; Erban, T., Distributions of imidacloprid, imidacloprid-olefin and imidacloprid-urea in green plant tissues and roots of rapeseed (*Brassica napus*) from artificially contaminated potting soil. *Pest Manag Sci* **2017**, 73 (5), 1010-1016.

(133) C. F. Macrae, I. S., S. J. Cottrell, P. T. A. Galek, P. McCabe, E. Pidcock, M. Platings, G. P. Shields, J. S. Stevens, M. Towler and P. A. Wood, Mercury 4.0: from visualization to analysis, design and prediction. *J. Appl. Cryst.* 53, 226-235.

(134) Khan, M. A. H.; Ashfold, M. J.; Nickless, G.; Martin, D.; Watson, L. A.; Hamer, P. D.; Wayne, R. P.; Canosa-Mas, C. E.; Shallcross, D. E., Night-time NO<sub>3</sub> and OH radical concentrations in the United Kingdom inferred from hydrocarbon measurements. *Atmos Sci Lett* **2008**, 9 (3), 140-146.

(135) Kroll, J. H.; Seinfeld, J. H., Chemistry of secondary organic aerosol: Formation and evolution of low-volatility organics in the atmosphere. *Atmos. Environ.* **2008**, 42 (16), 3593-3624.

(136) Witkowski, B.; Gierczak, T., Analysis of  $\alpha$ -acyloxyhydroperoxy aldehydes with electrospray ionization–tandem mass spectrometry (ESI-MSn). *J. Mass Spectrom.* **2013**, 48 (1), 79-88.

(137) California Air Resources Board (CARB) Air Quality Data Query Tool available via <https://www.arb.ca.gov/aqmis2/aqdselect.php>. Accessed April 19, 2021.

(138) Mihelcic, D.; Holland, F.; Hofzumahaus, A.; Hoppe, L.; Konrad, S.; Müsgen, P.; Pätz, H.-W.; Schäfer, H.-J.; Schmitz, T.; Volz-Thomas, A.; Bächmann, K.; Schlomski, S.; Platt, U.; Geyer, A.; Alicke, B.; Moortgat, G. K., Peroxy radicals during BERLIOZ at Pabstthum: Measurements, radical budgets and ozone production. *Journal of Geophysical Research: Atmospheres* **2003**, 108 (D4).

(139) Stevens, P. S.; Mather, J. H.; Brune, W. H.; Eisele, F.; Tanner, D.; Jefferson, A.; Cantrell, C.; Shetter, R.; Sewall, S.; Fried, A.; Henry, B.; Williams, E.; Baumann, K.; Goldan, P.; Kuster, W., HO<sub>2</sub>/OH and RO<sub>2</sub>/HO<sub>2</sub> ratios during the Tropospheric OH Photochemistry Experiment: Measurement and theory. *Journal of Geophysical Research: Atmospheres* **1997**, 102 (D5), 6379-6391.

- (140) Carslaw, N.; Creasey, D. J.; Heard, D. E.; Lewis, A. C.; McQuaid, J. B.; Pilling, M. J.; Monks, P. S.; Bandy, B. J.; Penkett, S. A., Modeling OH, HO<sub>2</sub>, and RO<sub>2</sub> radicals in the marine boundary layer: 1. Model construction and comparison with field measurements. *Journal of Geophysical Research: Atmospheres* **1999**, *104* (D23), 30241-30255.
- (141) Mihelcic, D.; Müsgen, P.; Ehhalt, D. H., An improved method of measuring tropospheric NO<sub>2</sub> and RO<sub>2</sub> by matrix isolation and electron spin resonance. *Journal of Atmospheric Chemistry* **1985**, *3* (3), 341-361.
- (142) Lippmann, M., Health Effects of Ozone: a Critical Review. *J Air Waste Manage* **1989**, *39* (5), 672-695.
- (143) Chen, T. M.; Gokhale, J.; Shofer, S.; Kuschner, W. G., Outdoor air pollution: Ozone health effects. *Am J Med Sci* **2007**, *333* (4), 244-248.
- (144) Sousa, S. I. V.; Alvim-Ferraz, M. C. M.; Martins, F. G., Health effects of ozone focusing on childhood asthma: What is now known - a review from an epidemiological point of view. *Chemosphere* **2013**, *90* (7), 2051-2058.
- (145) Milford, J. B.; Russell, A. G.; Mcrae, G. J., A New Approach to Photochemical Pollution-Control - Implications of Spatial Patterns in Pollutant Responses to Reductions in Nitrogen-Oxides and Reactive Organic Gas Emissions. *Environ Sci Technol* **1989**, *23* (10), 1290-1301.
- (146) Collet, S.; Kidokoro, T.; Karamchandani, P.; Shah, T., Future-Year Ozone Isopleths for South Coast, San Joaquin Valley, and Maryland. *Atmosphere-Basel* **2018**, *9* (9).
- (147) Sperling, D.; Eggert, A., California's climate and energy policy for transportation. *Energy Strategy Reviews* **2014**, *5*, 88-94.
- (148) SCAQMD. 2017. Final 2016 Air Quality Management Plan. <http://www.aqmd.gov/docs/default-source/clean-air-plans/air-quality-management-plans/2016-air-quality-management-plan/final-2016-aqmp/final2016aqmp.pdf>.
- (149) California Air Resources Board (CARB). 2022. Draft 2022 State Strategy for the State Implementation Plan. [https://ww2.arb.ca.gov/sites/default/files/2022-01/Draft\\_2022\\_State\\_SIP\\_Strategy.pdf](https://ww2.arb.ca.gov/sites/default/files/2022-01/Draft_2022_State_SIP_Strategy.pdf) (accessed 20 May 2022).
- (150) South Coast Air Quality Management District (SCAQMD). 2017. Final 2016 Air Quality Management Plan. <https://www.aqmd.gov/docs/default-source/clean-air-plans/air-quality-management-plans/2016-air-quality-management-plan/final-2016-aqmp/final2016aqmp.pdf?sfvrsn=15> (accessed 2 May 2022).
- (151) Pusede, S. E.; Cohen, R. C., On the observed response of ozone to NO<sub>x</sub> and VOC reactivity reductions in San Joaquin Valley California 1995-present. *Atmos Chem Phys* **2012**, *12* (18), 8323-8339.
- (152) Singh, H. B.; Cai, C.; Kaduwela, A.; Weinheimer, A.; Wisthaler, A., Interactions of fire emissions and urban pollution over California: Ozone formation and air quality simulations. *Atmos. Environ.* **2012**, *56*, 45-51.
- (153) Abatzoglou, J. T.; Williams, A. P., Impact of anthropogenic climate change on wildfire across western US forests. *Proceedings of the National Academy of Sciences* **2016**, *113* (42), 11770-11775.
- (154) Jaffe, D. A.; O'Neill, S. M.; Larkin, N. K.; Holder, A. L.; Peterson, D. L.; Halofsky, J. E.; Rappold, A. G., Wildfire and prescribed burning impacts on air quality in the United States. *J Air Waste Manage* **2020**, *70* (6), 583-615.

- (155) Lindaas, J.; Farmer, D. K.; Pollack, I. B.; Abeleira, A.; Flocke, F.; Roscioli, R.; Herndon, S.; Fischer, E. V., Changes in ozone and precursors during two aged wildfire smoke events in the Colorado Front Range in summer 2015. *Atmos Chem Phys* **2017**, *17* (17), 10691-10707.
- (156) McClure, C. D.; Jaffe, D. A., Investigation of high ozone events due to wildfire smoke in an urban area. *Atmos. Environ.* **2018**, *194*, 146-157.
- (157) Gong, X.; Kaulfus, A.; Nair, U.; Jaffe, D. A., Quantifying O<sub>3</sub> Impacts in Urban Areas Due to Wildfires Using a Generalized Additive Model. *Environ Sci Technol* **2017**, *51* (22), 13216-13223.
- (158) Gao, H.; Jaffe, D. A., Comparison of ultraviolet absorbance and NO-chemiluminescence for ozone measurement in wildfire plumes at the Mount Bachelor Observatory. *Atmos. Environ.* **2017**, *166*, 224-233.
- (159) US Environmental Protection Agency (EPA) Air Quality System (AQS) available via <https://www.epa.gov/outdoor-air-quality-data/download-daily-data>. Accessed April 19, 2021.
- (160) Wu, S.; Lee, H. J.; Anderson, A.; Liu, S.; Kuwayama, T.; Seinfeld, J. H.; Kleeman, M. J., Direct measurements of ozone response to emissions perturbations in California. *Atmos. Chem. Phys.* **2022**, *22* (7), 4929-4949.
- (161) Copernicus Sentinel-5P (processed by ESA) TROPOMI Level 2 Formaldehyde and Nitrogen Dioxide Total Column products. Version 02. available via Accessed March 9, 2021.
- (162) van Geffen, J.; Boersma, K. F.; Eskes, H.; Sneep, M.; ter Linden, M.; Zara, M.; Veefkind, J. P., S5P TROPOMI NO<sub>2</sub> slant column retrieval: method, stability, uncertainties and comparisons with OMI. *Atmos. Meas. Tech.* **2020**, *13* (3), 1315-1335.
- (163) Royal Netherlands Meteorological Institute. 2021. TROPOMI ATBD of the total and tropospheric NO<sub>2</sub> data products. <https://sentinel.esa.int/documents/247904/2476257/Sentinel-5P-TROPOMI-ATBD-NO2-data-products>.
- (164) US Environmental Protection Agency (EPA) 2017 National Emissions Inventory (NEI) Data available via <https://www.epa.gov/air-emissions-inventories/national-emissions-inventory-nei>. Accessed April 14, 2021.
- (165) California Department of Forestry and Fire Protection (CAL FIRE) Incident Database available via <https://www.fire.ca.gov/incidents/>. Accessed May 26, 2021.
- (166) California Air Resources Board (CARB) Daily Record of Agricultural Burning Control Notices available via <https://ww2.arb.ca.gov/ag-rx-burn-monthly-decisions>. Accessed March 1, 2021.
- (167) Giglio, L., Justice, C., Boschetti, L., Roy, D. MCD64A1 MODIS/Terra+Aqua Burned Area Monthly L3 Global 500m SIN Grid V006 available via <https://firms.modaps.eosdis.nasa.gov/usfs/map/>. Accessed July 16, 2021.
- (168) Brey, S. J.; Ruminiski, M.; Atwood, S. A.; Fischer, E. V., Connecting smoke plumes to sources using Hazard Mapping System (HMS) smoke and fire location data over North America. *Atmos Chem Phys* **2018**, *18* (3), 1745-1761.
- (169) Jin, X. M.; Fiore, A.; Boersma, K. F.; De Smedt, I.; Valin, L., Inferring Changes in Summertime Surface Ozone-NO<sub>x</sub>-VOC Chemistry over US Urban Areas from Two Decades of Satellite and Ground-Based Observations. *Environ Sci Technol* **2020**, *54* (11), 6518-6529.
- (170) Schroeder, J. R.; Crawford, J. H.; Fried, A.; Walega, J.; Weinheimer, A.; Wisthaler, A.; Müller, M.; Mikoviny, T.; Chen, G.; Shook, M.; Blake, D. R.; Tonnesen, G. S., New insights into

the column CH<sub>2</sub>O/NO<sub>2</sub> ratio as an indicator of near-surface ozone sensitivity. *Journal of Geophysical Research: Atmospheres* **2017**, *122* (16), 8885-8907.

(171) Ling, Z. H.; Zhao, J.; Fan, S. J.; Wang, X. M., Sources of formaldehyde and their contributions to photochemical O<sub>3</sub> formation at an urban site in the Pearl River Delta, southern China. *Chemosphere* **2017**, *168*, 1293-1301.

(172) Zhu, L.; Jacob, D. J.; Keutsch, F. N.; Mickley, L. J.; Scheffe, R.; Strum, M.; Abad, G. G.; Chance, K.; Yang, K.; Rappengluck, B.; Millet, D. B.; Baasandorj, M.; Jaegle, L.; Shah, V., Formaldehyde (HCHO) As a Hazardous Air Pollutant: Mapping Surface Air Concentrations from Satellite and Inferring Cancer Risks in the United States. *Environ Sci Technol* **2017**, *51* (10), 5650-5657.

(173) Martin, R. V.; Parrish, D. D.; Ryerson, T. B.; Nicks, D. K.; Chance, K.; Kurosu, T. P.; Jacob, D. J.; Sturges, E. D.; Fried, A.; Wert, B. P., Evaluation of GOME satellite measurements of tropospheric NO<sub>2</sub> and HCHO using regional data from aircraft campaigns in the southeastern United States. *J Geophys Res-Atmos* **2004**, *109* (D24).

(174) Lui, K. H.; Ho, S. S. H.; Louie, P. K. K.; Chan, C. S.; Lee, S. C.; Hu, D.; Chan, P. W.; Lee, J. C. W.; Ho, K. F., Seasonal behavior of carbonyls and source characterization of formaldehyde (HCHO) in ambient air. *Atmos. Environ.* **2017**, *152*, 51-60.

(175) Kesselmeier, J.; Staudt, M., Biogenic Volatile Organic Compounds (VOC): An Overview on Emission, Physiology and Ecology. *Journal of Atmospheric Chemistry* **1999**, *33* (1), 23-88.

(176) Larkin, N. K.; Strand, T. M.; Drury, S. A.; Raffuse, S. M.; Solomon, R. C.; O'Neill, S. M.; Wheeler, N.; Huang, S.; Roring, M.; Hafner, H. R. *Phase 1 of the Smoke and Emissions Model Intercomparison Project (SEMIP): Creation of SEMIP and evaluation of current models. Final Report to the Joint Fire Science Program Project #08-1-6-10.*; U.S. Joint Fire Science Program (JFSP) Research Project Reports, 2012; pp 1-44.

(177) Prichard, S. J.; Kennedy, M. C.; Andreu, A. G.; Eagle, P. C.; French, N. H.; Billmire, M., Next-Generation Biomass Mapping for Regional Emissions and Carbon Inventories: Incorporating Uncertainty in Wildland Fuel Characterization. *J Geophys Res-Biogeophys* **2019**, *124* (12), 3699-3716.

(178) Chen, J. J.; Ying, Q.; Kleeman, M. J., Source apportionment of wintertime secondary organic aerosol during the California regional PM<sub>10</sub>/PM<sub>2.5</sub> air quality study. *Atmos. Environ.* **2010**, *44* (10), 1331-1340.

(179) Baklanov, A. A.; Grisogono, B.; Bornstein, R.; Mahrt, L.; Zilitinkevich, S. S.; Taylor, P.; Larsen, S. E.; Rotach, M. W.; Fernando, H. J. S., The Nature, Theory, and Modeling of Atmospheric Planetary Boundary Layers. *B Am Meteorol Soc* **2011**, *92* (2), 123-128.

(180) Chan, K. M.; Wood, R., The seasonal cycle of planetary boundary layer depth determined using COSMIC radio occultation data. *J Geophys Res-Atmos* **2013**, *118* (22), 12422-12434.

(181) Chow, J. C.; Watson, J. G.; Lowenthal, D. H.; Chen, L. W. A.; Tropp, R. J.; Park, K.; Magliano, K. A., PM<sub>2.5</sub> and PM<sub>10</sub> mass measurements in California's San Joaquin Valley. *Aerosol Sci. Technol.* **2006**, *40* (10), 796-810.